Supplementary Information for

Single-step sound printing of bioadhesive in deep tissue

Yujie Jiang[1†], Tianqu Fan[2,3†], Mingyue Wang[1], Luyang Zhang[4,5], Chengxi Zhong[1], Jiaqi Li[1], Zhenhuan Sun[1], Yuting Yang[1], Hai Liu[6], Haojian Lu[7], Shuo Shi[2†,*], Song Liu[1,*]

[1]School of Information Science and Technology, ShanghaiTech University, Shanghai, China

[2]Shanghai Institute for Advanced Immunochemical Studies, ShanghaiTech University, Shanghai, China

[3]School of life Science and Technology, ShanghaiTech University, Shanghai, China

[4]Department of General Surgery, Ruijin Hospital, School of Medicine, Shanghai Jiao Tong University, Shanghai, China

[5]Shanghai Minimal Invasive Surgery Center, Shanghai, China

[6]Department of Electrical and Computer Engineering, University of Southern California, Los Angeles, CA, USA

[7]Institute of Cyber-Systems and Control, College of Control Science and Engineering, Zhejiang University, Hangzhou 310027, China

[†]These authors contributed equally to this work.

*Correspondence to: Shuo Shi (shishuo@shanghaitech.edu.cn); Song Liu (liusong@shanghaitech.edu.cn)

The PDF file includes:

Other Supplementary Information for this manuscript includes the following:

Materials

Lead zirconate titanate (PZT-5A, Piezo Systems, United States), AZ® 300 MIF (Merck KGaA, Darmstadt, Germany), AZ-5214 (MicroChemicals GmbH, Germany), SU-8 3025 (Kayaku Advanced Materials, USA) were used as received. Acrylic acid (Aladdin, 79-10-7, China), acryloyl *N*-hydroxysuccinimide ester (Merck, 38862-24-7, United States), alpha-ketoglutaric acid (Merck, alpha-ketoglutaric acid, United States), chitosa (Merck, 9012-76-4, United States), NaOH (Merck, 1310-73-2, United States), isopropanol (Merck, 67-63-0, United States), sodium dodecyl sulfate (Merck, 106-88-7, United States), iohexol (Merck, 66108-95-0, United States) epoxybutane (Merck, 109975, United States) were used as received. Cell lines used in this study were AGS (ATCC, CRL-1739) and SNU-1 (ATCC, CRL-5971). Phosphate-buffered saline (PBS), fetal bovine serum (FBS), F12-K medium, RPMI 1640 medium, trypsin-EDTA, and penicillin-streptomycin were purchased from Thermo Fisher Scientific. Antibodies used in this study were anti-Ki67 (Servicebio, GB111499), anti-CD31 (Servicebio, GB123151), CY3 anti-rabbit (Servicebio, GB21303), Alexa Fluor 488 anti-mouse (Servicebio, GB25301). Live/Dead Viability/Cytotoxicity Kit (C2015S) was purchased from Beyotime Biotechnology. Firefly d-luciferin (MB1834) was supplied from MeilunBio. Oxaliplatin (HY-17371) was purchased from MedChemExpress. All experiments involving rats and mice complied with all relevant ethical regulations, approved by the ShanghaiTech University Animal Care and Use Committee (Approval number: 20230604001).

Methods

Ultrasound transducer array. The ultrasound transducer array (Extended Data Fig. 1a) in S^3P is crafted from a 1 mm thick naked piezoelectric ceramic (Lead zirconate titanate, PZT-5A) using a standard photolithography process. After rinsing the PZT surfaces with acetone and deionized water, a 2 μm thick positive photoresist is spin-coated on the backside, followed by ultraviolet lithography (Microwriter ML3, Durham Magneto Optics, UK) to photoetch a 50 × 50 array of 800 μm × 800 μm square electrodes onto the photoresist (developed with AZ® 300 MIF). The pitch size is 1 mm, featuring aperture size of 50 mm × 50 mm (Extended Data Fig. 1b). Then, 20 nm thick titanium and 100 nm thick nickel are sequentially sputtered onto the backside of the PZT. The PZT is then immersed in acetone for five mins under ultrasonic treatment to remove the redundant metal and photoresist, forming the array of 50 × 50 electrodes. Subsequently, 20 nm thick titanium, 100 nm thick nickel, and another 20 nm thick titanium are sputtered on the topside of the PZT to create the ground electrode. On both sides of the PZT, titanium is deposited to enhance the adhesion between the nickel and PZT. Finally, a 310 μm thick layer of SU-8 3025 is spin-coated on the topside for acoustic impedance matching, followed by a 5 μm thick coating of Parylene C for waterproofing.

The ultrasound transducer array functions through its 50 × 50 array of square electrodes, each independently actuated by 2.32 MHz electrical square waves, essentially creating 2500 densely packed vibration sources. These sources emit sound waves with uniform amplitude but precise phase differences, controlled by the actuation voltages delivered to each electrode. These voltages are generated by a driving board containing six field programmable gate arrays (FPGAs, XC7A200T-1FFG1156I, 200 MHz, Xilinx, United States), which receives phase information from a host computer via a controller area network (CAN bus, 500 kilobits per second). The phase information is calculated by the host computer using a deep learning-based

ultrasound beamforming algorithm to create the desired sound image (see next section). The emitted sound waves from the ultrasonic transducer array then penetrate deep into the tissue, reaching the targeted tissue surface, where they interfere constructively to form the corresponding sound image, selectively depositing heat energy by sonothermal effect to cure thermoresponsive bioadhesive (Extended Data Fig. 1c).

Super-resolution ultrasound beamforming algorithm. A deep-learning based ultrasound beamforming algorithm is developed to compute the phase information to control the phase shifts of the emitted sound waves from the ultrasound transducer array. With this algorithm, the transducer array can generate super-resolution sound images upon targeted tissue surface[1]. Specifically, we established a deep neural network using PyTorch 3.9.7, following the U-Net architecture[2] (Extended Data Fig. 6a), whose input is an expected sound image in customized resolution of $m \times n$ pixels (covering 50 mm × 50 mm surface area, where m and n are pixel counts along two axes of sound image and valued as 25 × 25, 50 × 50, 150 × 150, 250 × 250, and 300 × 300 in the experiments), and output is the phase information in fixed resolution of 50 × 50 pixels corresponding to the 50 × 50 array of square electrodes on the ultrasonic transducer array. Notably, the U-Net features a globally asymmetrical framework and locally adaptive convolutional components, facilitating alignment of fixed output resolution and the model's ability to handle sound images with different resolutions. The U-Net, initialized by Kaiming method, was trained with a self-supervised learning strategy, which was implemented using a numerical sound image reconstruction method formulated by the piston source model and linear accumulation[3]. The linear accumulation models sound images as a series of acoustic pressure amplitudes assigned to individual spatial positions, associating sound images and ultrasound transducer array through independent acoustic propagation. Thus, the acoustic amplitudes of sound images can be reconstructed by accumulation of entire transducer elements and the reconstructed sound images can exhibit the same resolution as expected sound

image. The loss function was defined by comparing the sound amplitude differences between the expected sound images and the reconstructed sound images, providing an optimization gradient for neural network training using the Adam optimizer. The used loss function is thereby defined as

$$L = \frac{1}{m \cdot n} \sum \left\{ p^{T}_{x,y,d} - p^{C}_{x,y,d} \right\} = \frac{1}{m \cdot n} \left\{ p^{T}_{x,y,d} - P \cdot \exp\left(j\varphi^{C}_{x,y,0} \right) \right\} \quad (1)$$

where $p^{T}_{x,y,d}$ and $p^{C}_{x,y,d}$ are the expected and reconstructed sound images, $\varphi^{C}_{x,y,0}$ is the phase information generated by the neural network, m and n equals 50 in this context.

To meet common bioadhesive deployment requirements in different clinical scenarios, a dataset consisting of sound images with various geometrical patterns, such as lattice, solid area images, and contour images were prepared (Extended Data Fig. 6b). The Python code and the prepared dataset are available from supplementary source data.

Characterization of sound patterning resolution of S^{3}P system. To characterize the sound pattern resolution with varying water/tissue thickness or transducer size, we measured the single focal pressure profile using a needle hydrophone (Precision Acoustics, 200 μm diameter needle tip, UK). We mounted the hydrophone to a motion stage (KWL06050, Suruga Seiki, Japan). The scanning movement of the hydrophone was controlled by the PC, which also collected the voltage signal from the hydrophone. The voltage signal was converted into ultrasound pressure based on the hydrophone's sensitivity of 52 mV/MPa at a frequency of 2.32 MHz.

To characterize the single focal pressure profile in pure water, we placed the hydrophone needle tip at the focal point and then scanned the sound field in a 2 mm × 2 mm plane parallel to the sound source array with a 100 μm scanning step size (Extended Data Fig. 2a). Next, we scanned

in a 4 mm × 4 mm plane perpendicular to the sound source array with a 200 μm step size (Extended Data Fig. 2c), obtaining the cross-sectional pressure profile of the focused ultrasound.

To characterize impacts of tissue penetration on sound patterning resolution, we scanned the single focal pressure profile with varying water/tissue thickness (Extended Data Fig. 2f, g). To measure the impact with varying tissue thickness, the transducer generated a single focal point at the plane of Z = 50 mm, and the transducer size was fixed at 50 mm. To measure the impact with varying water thickness, the transducer generated the single focal point at the plane of Z equal to water thickness. The needle hydrophone was used to scan the sound pressure step by step. Porcine liver, stomach, and brain tissues with different thicknesses from 10 mm to 50 mm were placed between the transducer plane and focal plane. For each tissue/water thickness, we scanned three times. During the field scanning, we first moved the tip of the hydrophone to the focal point. Then we scanned within a 2 mm × 2 mm area parallel to the sound source array with 100 μm step size to obtain the whole single focal pressure distribution.

To characterize the impact of transducer size on sound patterning resolution, we measured the single focal pressure profile with transducer size of 30 mm × 30 mm, 36 mm × 36 mm, 40 mm × 40 mm, 46 mm × 46 mm, and 50 mm × 50 mm, respectively (Extended Data Fig. 2j, k). To achieve the varying sizes of transducers (T), we deactivated the outer 1600, 1204, 900, 384, and 0 channels of 2500 channels in the 50 mm × 50 mm transducer for each transducer size. For each transducer size, the transducer generated a single focal point at the plane of Z = T mm. The needle hydrophone was used to scan the sound pressure step by step. For each transducer size, we scanned three times. During the field scanning, we first moved the tip of the hydrophone to the focal point, and then we scanned within a 2 mm × 2 mm area parallel to the sound source array with 100 μm step size to obtain the whole single focal pressure distribution.

To measure the lateral focal size (-6 dB attenuation), we further used the original data obtained by scanning the single focal with hydrophone and then acquired the sound pressure profile (Fig. 2d, Extended Data Fig. 2b, d, i). Spatial resolution of the scanning data was 100 μm. We used bilinear interpolation to calculate sound pressure between scanning data points. We established an image coordinate (u, v). By bilinear interpolation, we actually constructed a function P (u, v) whose value was the sound pressure of the point (u, v). After that, we found the location of the maximum pressure point, denoted as (u_0, v_0), and next we calculated the pressure of point ($u_0 + L\cos\alpha$, $v_0 + L\sin\alpha$) by function P (u, v). For each direction α, there always existed a length L that satisfies $P(u_0 + L\cos\alpha, v_0 + L\sin\alpha) / P(u_0, v_0) = 1/2$, so we built a function $L(\alpha)$ that satisfied the equation above. $L(\alpha)$ was the radius of the focal point along direction α. As a result, we calculated the average value of $L(\alpha)$ and use this value to represent radius of the focal point. For each direction α, the binary search method was used to find L. Unit of function $L(\alpha)$ was pixel length, so we further multiplied the pixel length with pixel equivalent to obtain physical focal radius.

Preparation of bioadhesive solution used in S^{3}P. The thermoresponsive bioadhesive solution consists of poly (acrylic acid) N-hydroxysuccinimide (NHS) ester (PAA-NHS) and hydroxybutyl chitosan (HBCS) (Fig. 1b). To prepare PAA-NHS, 30 w/w% acrylic acid, 1 w/w% acryloyl N-hydroxysuccinimide ester (AAc-NHS ester), and 0.5 w/w% alpha-ketoglutaric acid were dissolved in deionized water and reacted for 360 minutes. Then the solution was freeze-dried and ground into PAA-NHS powder. The PAA-NHS was stored in a desiccator at 4 °C for further use. To prepare hydroxybutyl chitosan, 15 g of chitosan was added into 100 ml of 10 w/w % NaOH solution and alkalized for 24 hours. The alkalized chitosan was then added into a 50% isopropanol-water solution and stirred for 3 hours. Subsequently, 0.2 g of sodium dodecyl sulfate and 200 mg of epoxybutane were added to the solution, which was then heated to 50 °C for 12 hours. Then the pH was adjusted to 7. The mixture was dialyzed, centrifuged,

and the supernatant was collected. Finally, the supernatant was lyophilized to obtain hydroxybutyl chitosan. To prepare the bioadhesive solution, a 7 w/w% HBCS solution was used as the precursor. 5 mg of PAA-NHS powder was mixed into 1 ml of HBCS.

Sonothermal effect characterization on tissue surfaces *in vitro*. To characterize the sonothermal effect on different tissue surfaces, we used C57BL/6 mice (6–8 weeks, GemPharmatech). The mice were sacrificed using carbon dioxide (CO_2) inhalation. Subsequently, the fresh skin, liver, and stomach were harvested. The skull was then carefully separated using a cranial drill to completely extract the brain. All experiments were carried out at room temperature (24 °C). To measure the temperature on liver, stomach, and brain surfaces, the mice skin was firstly placed on the platform of printer, and the liver, stomach, and brain, were placed on the skin. Then, we used an injector to place a layer of water between the skin and platform for impedance matching while another layer of PBS solution between the organ and the skin to simulate the physiological environment. After that, we applied 100 µl of bioadhesive solution onto the tissue surface and placed a thermal gauge (YET-620x, KAIPUSEN, China) into the bioadhesive upon the tissue (Extended Data Fig. 5a). Each experiment in Extended Data Fig. 5b involved recording the temperature for 5 minutes once the ultrasound was turned on, and was repeated three times with an actuation voltage of 9 Volts. The setup for the experiments in Extended Data Fig. 5c was identical. We adjusted the ultrasonic pressure through the actuation voltage, which controlled the input power. At 100% input power, the focused ultrasonic beam, measured via hydrophone scanning (Precision Acoustics, 200 µm needle tip, UK), reached 2.75 MPa. Given the ultrasonic pressure is linearly related to the input power, modulating the actuation voltage allowed us to set 22% input power to achieve a focal pressure of 0.6 MPa. The experiment was conducted with input power increments of 11% per step (Extended Data Fig. 5b, c).

Temperature control in S^{3}P. During bioadhesive printing process, S^{3}P maintained the temperature at target tissue surface around 42 ℃, which was about 3 ℃ higher than that of the body temperature of mice, ensuring rapid bioadhesive curing in about TI without heating damage (Supplementary Note 7). In this regard, the input sound energy was controlled accordingly for printing different patterns on different tissue surfaces (Extended Data Fig. 7). For an 8 mm × 8 mm circular area (defined by the sound image), the input energy required to maintain 42 ± 0.3 ℃, compared with full power operation (9 Volts), was 80% for the liver, 83% for the brain, and 88% for the stomach. For a smaller 4 mm × 4 mm circular area, less energy was required as the smaller region can better concentrate the ultrasonic waves. The input energy needed, compared with full power operation, was 63% for the liver, 65% for the brain, and 70% for the stomach to maintain 42 ± 0.3 ℃. For a 2 mm × 2 mm circular area, the input energy required, compared with full power operation, was 51% for the liver, 54% for the brain, and 59% for the stomach to maintain 42 ± 0.3 ℃.

Characterization of the heat accumulation. To characterize the heat accumulation under single focal pressure, we sliced fresh porcine liver, stomach, and brain tissues into 3 mm thin sections and placed them on petri dishes. The tissues were then preheated to 35 °C in an incubator. A 1 mm thick layer of bioadhesive solution was applied to cover the tissue surface, and the tissue was exposed to a single focal pressure. The relationship between sound pressures and temperature increase was determined by characterization of the sonothermal effect on different tissue surfaces. During the heating process, we used an infrared thermal camera (RT630, Raythink, China) to monitor the temperature. When the average temperature in the region reached the target temperature of 37 °C (Extended Data Figure. 8a-c), 39 °C and 42 °C and stabilized, we recorded the diameter of the region (Extended Data Figure. 8d) and measured the temperature difference between the maximum and minimum values within the region (Extended Data Figure. 8e).

To measure the characterization of heat accumulation under different sound pattern sizes, we sliced fresh porcine liver, stomach, and brain tissues into 3 mm thin sections and placed them on petri dishes. The tissues were then preheated to 35 °C in an incubator. A 1 mm thick layer of bioadhesive solution was applied to the tissue surface. We used sonothermal with 5 mm, 10 mm, and 15 mm circular pattern size to heat tissues covered with bioadhesive solution to 42 °C (Extended Data Figure. 9a). During the heating process, we used an infrared thermal camera (RT630, Raythink, China) to monitor the temperature. Once the average temperature in the region reached 42 °C and stabilized, we recorded the region's diameter and took 100 evenly distributed sample points within the region to calculate the standard deviation.

To measure the characterization of heat accumulation under different pixel densities, we sliced fresh porcine liver, stomach, and brain tissues into 3 mm thin sections and placed them on petri dishes. The tissues were then preheated to 35 °C in an incubator. A 1 mm thick layer of bioadhesive solution was applied to the tissue surface. We used sonothermal with 5 mm, 10 mm (Extended Data Figure. 9b), and 15 mm diameters sound pattern at pixel densities of 1 pixel/mm², 9 pixels/mm², and 25 pixels/mm² to heat the tissues to 42 °C. During the entire heating process, we used an infrared thermal camera to monitor the temperature. Once the average temperature in the region reached 42 °C and stabilized, we evenly sampled 100 points within the region and calculated the standard deviation (SD) (Extended Data Figure. 9c-e).

Characterization of the curing behaviors of the bioadhesive in S^{3}P. To characterize and compare the curing process of bioadhesive under hotplate heating and sonothermal heating, we first weighed several equal portions (m_0 = 1 g) of bioadhesive solution for each heating method group. These portions were then preheated to 34 °C. The bioadhesive was subsequently heated using either sonothermal or hotplate heating. Every 30 seconds, the fluid portion was removed, and the remaining mass was weighed so that the mass of the cured portion (m_t) was measured.

We calculated the curing percentage by the ratio of m_t/m_0, which quantifies the curing process (Extended Data Figure. 10a, b).

To further characterize the curing process of the bioadhesive, rheological properties were measured using a rotational rheometer (MARS 60, HAAKE, United States) (Extended Data Figure. 10c). The testing gap between the parallel plates was set to 0.3 mm. The sample was equilibrated at 10 °C for 120 seconds prior to testing. Oscillatory temperature sweeps were performed under a controlled stress of 1 Pa and a frequency of 1 Hz. The temperature was increased from 10 °C to 60 °C at a constant rate of 1 °C per minute.

Mechanical characterization of printed bioadhesive. The adhesion and mechanical properties of the printed bioadhesive on tissue surfaces in terms of adhesion energy, tensile stress, shear strength, Young's modules, and tear energy. The adhesion properties including adhesion energy, tensile stress and shear strength were measured by standard 180° peeling, standard tensile, standard lap-shear test respectively. Young's modulus and tear energy were calculated based on the stress-strain curves by tensile test. All of the tests were performed on the universal testing system (5966, Instron, United States) at a deformation rate of 5 mm/s with 24 °C room temperature.

For the adhesion properties, commercially available tissue bioadhesives (Histoacryl, Coseal, and Tisseel) were tested as control. Before the experiment, the rat colon was cut into slices with a dimension of 20 mm × 10 mm, and then cleaned with PBS buffer. To fabricate adhering tissue joints, bioadhesives were applied to a 10 mm ×10 mm area of cut tissue. For our bioadhesive, we heated the tissue by the hotplate or sonathermal to 42 °C and maintained the temperature for 5 minutes or 40 seconds with 24 °C room temperature. Commercially available bioadhesives were applied at equally large tissue areas. All of the commercially available bioadhesives were applied following the standard user guide or manual for each product

(measured after 1 min of application for Histoacryl, 3 mins for Coseal, and 3 mins for Tisseel). Before applying the bioadhesive or commercially available tissue adhesives, tissues were covered with PBS to ensure wetness. Nylon papers (200 μm in thickness) were adhered on the other side of the tissues as stiff backings using cyanoacrylate glue, in order to avoid the elastic deformation of the biological tissues. Aluminum fixtures were applied using cyanoacrylate glues to provide grips for tensile tests (Fig. 3d).

For characterizing the adhesion performance and mechanical properties under different concentrations, we prepared different formulations of bioadhesive by adding 3 mg, 4 mg, and 5 mg of PAA-NHS to 1 mL of standard bioadhesive precursor solution. Additionally, we prepared precursor solution with 4 wt% HBCS, adding 2.5 mg of PAA-NHS per mL of precursor solution. For adhesion performance tests, we cut the rat colon into slices measuring 20 mm × 10 mm and cleaned them with PBS buffer. To fabricate adhering tissue joints, bioadhesives were applied to a 10 mm × 10 mm area of the cut tissue. The tissues were then heated by sonothermal to 42 °C and maintained at that temperature for the curing duration corresponding to each formulation. Standard 180° peeling (Extended Data Fig. 11a), standard tensile (Extended Data Fig. 11b), and standard lap-shear tests (Extended Data Fig. 11c) were then performed. To characterize the mechanical properties, we uniformly injected 1 ml of the bioadhesive solution with the above formulations via subcutaneous injection into the backs of mice. The solution was then heated by sonothermal to 42 °C and maintained at that temperature for the curing duration corresponding to each concentration, the uncured bioadhesive was then aspirated. After 1 hour, the mice were sacrificed, and the cured bioadhesive was retrieved and performed tensile test at a deformation rate of 5 mm/min. Young's modulus (Extended Data Fig. 11e) and tear energy (Extended Data Fig. 11f) were calculated based on the stress-strain curves.

For characterizing the adhesion performance mechanical properties of bioadhesives cured at different temperatures under sonothermal heating, we cut the rat colon into slices with dimensions of 20 mm × 10 mm and then cleaned them with PBS buffer. To fabricate adhering tissue joints, the bioadhesive solution was applied to a 10 mm × 10 mm area of the cut tissue. The tissues were then heated to 37 °C, 39 °C, and 42 °C by sonothermal for indicated curing time. Standard 180° peeling (Extended Data Fig. 15a), standard tensile (Extended Data Fig. 15b), and standard lap-shear tests (Extended Data Fig. 15c) were then performed at a deformation rate of 5 mm/min. For characterizing of mechanical properties of bioadhesives cured at different temperatures under sonothermal heating, we uniformly injected 1 ml of bioadhesive solution subcutaneously into the backs of mice. The solution was then heated using sonothermal treatment to 37 °C, 39 °C, and 42 °C, with each temperature maintained for the corresponding curing time, the uncured bioadhesive was then aspirated. After 1 hour, the mice were sacrificed, and the bioadhesive was retrieved. Tensile tests were performed at a deformation rate of 5 mm/min, and Young's modulus (Extended Data Fig. 15d) and tear energy (Extended Data Fig. 15e) were calculated based on the stress-strain curves. Besides, to characterize the mechanical properties of bioadhesive cured by hotplate, after injecting the bioadhesive solution to the mice, we heated the dorsal of the mice with a hotplate to 42 °C for 5 minutes and tested the mechanical properties as above.

For characterizing the long-term *in vivo* adhesion performance and mechanical properties of the delivered bioadhesive, we uniformly injected 1 ml of bioadhesive solution subcutaneously into the backs of mice. The solution was then heated using sonothermal treatment to 42 °C and maintained for 40 seconds, the uncured bioadhesive was then aspirated. After curing, the mice were sacrificed at 1, 6, 12, 24, and 48 hours. The fur on the back of the mice was removed, and the skin and underlying muscle adhered to the bioadhesive were excised to 20 mm × 10 mm, and excess bioadhesive was removed, ensuring that the bioadhesive only adhered to the joints

of 10 mm. Standard 180° peeling (Extended Data Fig. 16a), standard tensile (Extended Data Fig. 16b), and standard lap-shear tests (Extended Data Fig. 16c) were then performed. For the mechanical properties, mice were sacrificed at 1, 6, 12, 24, and 48 hours, and the bioadhesive was retrieved and trimmed. Tensile tests were then performed, and Young's modulus (Extended Data Fig. 16d) and tear energy (Extended Data Fig. 16e) were calculated based on the stress-strain curves. The deformation rate was 5 mm/min.

For characterizing the adhesion performance of bioadhesives cured at different pixel densities under sonothermal heating, we cut the rat colon into slices measuring 20 mm × 10 mm and cleaned them with PBS solution. To fabricate adhering tissue joints, bioadhesives were applied to a 10 mm × 10 mm area of the cut tissue. The tissue was then heated to 42 °C for 40 seconds using sound patterns with pixel densities of 0.25, 1, 9, and 25 pixels/mm². Standard 180° peeling (Extended Data Fig. 17a), standard tensile (Extended Data Fig. 17b), and standard lap-shear tests (Extended Data Fig. 17c) were then performed. For characterizing the mechanical properties of bioadhesives cured at different pixel densities under sonothermal heating, we uniformly injected 1 ml of bioadhesive solution subcutaneously into the back of mice. The tissue was then heated to 42 °C using sound patterns with pixel densities of 0.25, 1, 9, and 25 pixels/mm², and maintained at that temperature for 40 seconds, the uncured bioadhesive was then aspirated. After 1 hour, the mice were euthanized, and the bioadhesive was retrieved and trimmed. Tensile tests were then performed, and Young's modulus (Extended Data Fig. 17d) and tear energy (Extended Data Fig. 17e) were calculated based on the stress-strain curves. The deformation rate was 5 mm/min.

For characterizing the adhesion performance and mechanical properties of bioadhesives cured at different pattern sizes under sonothermal heating. We cut the rat colon into slices with dimensions of 10 mm × 5 mm, 20 mm × 10 mm, and 30 mm × 15 mm, and then cleaned them

with PBS buffer. To fabricate adhering tissue joints, bioadhesive solution was applied to 5 mm × 5 mm, 10 mm × 10 mm, and 15 mm × 15 mm areas of the cut tissue. The tissue was then heated to 42 °C lasting 40 seconds. Standard 180° peeling (Extended Data Fig. 20a), standard tensile (Extended Data Fig. 20b), and standard lap-shear tests (Extended Data Fig. 20c) were then performed. For characterizing the mechanical properties of bioadhesives cured at different pattern sizes under sonothermal heating, we uniformly injected 1 ml of bioadhesive solution subcutaneously into the backs of mice. The tissue was then heated to 42 °C for 40 seconds. The uncured bioadhesive was then aspirated, and after 1 hour, the mice were euthanized. The tissue was dissected, and tensile tests were performed. Young's modulus (Extended Data Fig. 20d) and tear energy (Extended Data Fig. 20e) were calculated based on the stress–strain curves.

Characterization of curing behaviors and biodegradability of PAA-NHS/HBCS formulation under different concentrations. To characterize the curing behaviors and biodegradability of PAA-NHS/HBCS formulation under different concentrations, we prepared different formulations of bioadhesive by adding 3 mg, 4 mg, and 5 mg of PAA-NHS to 1 ml of standard bioadhesive precursor solution. Additionally, we prepared precursor solution with 4 wt% HBCS and added 2.5 mg of PAA-NHS per ml of precursor solution. To measure the biodegradability of 0.25 wt% bioadhesive solution (Extended Data Fig. 11d), we applied 1 ml of bioadhesive solution to the stomach of mice curd by sonothermal heating at 42 °C. The remaining bioadhesive area was recorded every hour to quantify the biodegradability.

To measure the curing temperature (Extended Data Fig. 11g), we applied sonothermal treatment to bioadhesives with different formulations, starting at 42 °C and increasing the temperature by 1 °C at each step, heating for 40 seconds. This allowed us to determine the temperature threshold at which curing could be achieved within 40 seconds of sonothermal treatment.

To measure the curing time (Extended Data Fig. 11h), we tested different bioadhesive formulations with sonothermal heating to 42 °C, recording the shortest time determined as curing time.

Cytocompatibility, biocompatibility, and biodegradability characterization of S^3P. The *in vitro* cytocompatibility (Extended Data Fig. 24a, b, c, d) tests using the bioadhesive solution were conducted by culturing cells on the cell culture plates pre-coated with bioadhesive. Specifically, to prepare the films, sterilized bioadhesive was thermally cured in the wells of a 24-well cell culture plate heated to 42 °C by S^3P for 40 seconds. The bioadhesive-coated cell culture plates were then added to PBS and left to sit in cell culture incubator for 10 mins. After removing the PBS, gastric cancer cells resuspended in cell culture media were seeded onto bioadhesive-coated cell culture plates. Two gastric cancer cell lines were used, i.e., AGS (ATCC, CRL-1739) and SNU-1 (ATCC, CRL-5971). AGS cells were cultured in F12-K medium and SNU-1 cells in RPMI 1640 medium, both with 10% fetal bovine serum and 100 U ml^{-1} penicillin-streptomycin. Cell density was 0.2 - 0.4 × 10^5 cells ml^{-1}. Gastric cancer cells cultured on cell culture plates without bioadhesive coating served as the control group for the experiments. The cell viability was determined using a LIVE/DEAD viability/cytotoxicity kit (Beyotime, C2015S) at different culture times (1–3 days). Briefly, Calcein-AM and PI were added to each well of cell culture plates, followed by incubation at 37 °C for 30 mins. A laser confocal microscope (Carl Zeiss, LSM 710) was then used to image live cells at excitation/emission wavelengths of 494 nm/517 nm and dead cells at 535 nm/617 nm. The cell viability was subsequently calculated by counting the number of live (green fluorescence) and dead (red fluorescence) cells using ImageJ (version 1.48).

For *in vivo* biocompatibility evaluation of S^3P (Extended Data Fig. 24e, f), the C57BL / 6 mice (6–8 weeks, GemPharmatech) were anesthetized with pentobarbital sodium (50 mg kg^{-1}).

Abdominal hair was then removed, and the animals were placed on a heating pad during the surgery. Thereafter, the liver or stomach was exposed via a laparotomy. For *in vivo* biocompatibility evaluation, the mouse was placed on the platform of printer. The input power of ultrasound was controlled at 80% of full power operation (9 Volts) for the liver and 88% for the stomach to maintain the temperature at the target tissue surface around 42 ± 0.3 ℃ for 40 seconds. The abdominal wall muscle and skin incision was closed using 6-0 sutures. Three days after ultrasound treatment, the animals were sacrificed. Stomach and liver tissues of interest were excised and fixed in 4% paraformaldehyde for 24 hours for histological analysis.

For *in vivo* biodegradability (Extended Data Fig. 26a) evaluation of printed bioadhesive, the C57BL / 6 mice (6–8 weeks, GemPharmatech) were anesthetized with pentobarbital sodium (50 mg kg^{-1}). The back hair was removed, and the animals were placed over a heating pad for the duration of the surgery. Then, 0.5 ml bioadhesive solution was injected into the left subcutaneous space at 24 °C room temperature. Finally, the mouse was put on the platform of printer and heated locally to 42 °C for 40 seconds by S^3P. At 0^{th}, 2^{nd}, 4^{th}, 6^{th}, 8^{th}, and 10^{th} day (n = 3) after bioadhesive delivery, the animals were anesthetized with pentobarbital sodium and opened, and the area of bioadhesive was taken images to measure the biodegradability.

For *in vivo* biodegradability (Fig. 3e) evaluation of printed bioadhesive on stomach, the C57BL / 6 mice (6–8 weeks, GemPharmatech) were anesthetized with pentobarbital sodium (50 mg kg^{-1}). The abdominal hair was removed, and the stomach was exposed by surgery. The animals were placed over a heating pad for the duration of the surgery. Then 150 µl bioadhesive was injected onto the stomach of the mouse. Then the mouse was heated locally to 42 ℃ by the printer. Finally, the mouse was closed by 6-0 suture. At 0^{th}, 1^{st}, 2^{nd}, 3^{rd}, and 4^{th} day (n = 3), the mice were anesthetized with pentobarbital sodium and opened to inspect the bioadhesive area.

***In vitro* characterization of bioadhesive solution biodegradability**. To prepare *in vitro* enzymatic biodegradation solution for the bioadhesive, we added 0.5 mg lysozyme (Sigma) in 10 ml PBS. The 70 mg of dry HBCS powder was then dissolved in 1 ml of the enzymatic medium within glass scintillation vials and incubated at 37 °C with shaking at 60 r.p.m. At each time interval, the solution was monitored using Ultraviolet–visible spectroscopy (UV-Vis) at the absorbance of 210 nm (Extended Data Fig. 26d).

Cardiac hemostasis. For hemostatic sealing of the full thickness ventricular injury, the rats (12 weeks, GemPharmatech) were anesthetized with pentobarbital sodium (50 mg kg^{-1}). Chest hair was removed. The heart was exposed via a thoracotomy and the pericardium was removed using fine forceps. A 4 mm incision was made to the left ventricular wall of the heart using an ophthalmic surgical scissor. To form hemostatic sealing, 300 μl of the adhesive was injected onto the bleeding site and then heated locally to 42 °C by S^3P (n = 4). For the untreated group, no hemostasis was performed (n = 4). The amount of blood loss until hemostasis was reached and the time to hemostasis were recorded for each group. After the rats were sacrificed, hearts were excised and fixed in 4% paraformaldehyde for 24 hours for histological analysis. Animal experiments were approved by the Animal Ethics Committee at ShanghaiTech, and performed in accordance with the institutional guidelines.

Minimally invasive gastric perforation repair. System control experiments. For *in vivo* gastric perforation repair in the mouse model, C57BL / 6 mice (6–8 weeks, GemPharmatech) were fasted for 24 hours before repairing to minimize bowel contents in the stomach. Mice were divided into four groups (n = 4 per group): (1) no treatment; (2) bioadhesive only; (3) ultrasound exposure only; (4) S^3P repair. After the mice were anesthetized with pentobarbital sodium (50 mg kg^{-1}), their abdominal hair was removed. A 2 mm incisional defect was made to the stomach by using an ophthalmic surgical scissor. The mice were placed on a heating pad

during the surgery. Then the bioadhesive only group was given 100 μl bioadhesive solution. The ultrasound exposure only group was put on the platform of printer and heated to 42 ℃ for 40 seconds. S^3P repair group was given 100 μl bioadhesive solution and heated to 42 ℃ for 40 seconds by the printer. After the treatment, the abdominal wall muscle and skin incision were closed with 6-0 sutures. 3 days after the repair, the mice were sacrificed (Extended Data Fig. 29). Stomach tissues of interest were excised and fixed in 4% paraformaldehyde for 24 hours for histological and immunofluorescence analyses. Animal experiments were approved by the Animal Ethics Committee at ShanghaiTech, and performed in accordance with the institutional guidelines.

Treatment control experiments: Before the experiments, C57BL / 6 mice (6–8 weeks, GemPharmatech) were fasted for 24 hours before repairing to minimize bowel contents in the stomach. Mice were divided into two groups (n = 5 per group): (1) suture treatment; (2) S^3P repair. For S^3P repair group, after the mice were anesthetized with pentobarbital sodium (50 mg kg^{-1}). The mice were gavaged with 100 μl of iohexol contrast agent. Then the abdominal hair was removed. A 2 mm incisional defect was made to the stomach by an ophthalmic surgical scissor. The abdominal wall muscle and skin were closed with 6-0 sutures after the incision was created. The mice were placed on a heating pad during the surgery. The mice were first scanned using micro-CT (x-cube, MOLECUBES, United States) with its right side facing up. After scanning, the mice were carefully removed and placed on the single-step sound printing platform in same posture. In the end of this process, the geometrical center of mouse was aligned with the platform coordinate system. We obtained the position of gastric perforation relative to the center of the mouse from three-dimensional micro-CT image to direct injecting bioadhesive solution process and printing process. Before the printing, we converted the perforation location to the platform's absolute coordinates using image Jacobian matrix[4]. A laparoscope was inserted into the mouse around the perforation site minimally invasively to

visualize the printing process. 100 μl bioadhesive solution with iohexol was injected into the mice. Then the mouse was heating to 42 ℃ locally for about 40 seconds by S^3P. For the surgical group, after the incision was created, the wound was sutured with three continuous stitches by 6-0 suture. After treatment, the muscle and skin were sutured. 3 days after the treatment, the mice were sacrificed. Stomach tissues of interest were excised and fixed in 4% paraformaldehyde for 24 hours for histological analyses (Extended Data Fig. 29j, k). Animal experiments were approved by the Animal Ethics Committee at ShanghaiTech, and performed in accordance with the institutional guidelines.

To measure long-term tissue interaction of the delivered bioadhesives by S^3P, C57BL / 6 mice (6–8 weeks, GemPharmatech) were fasted for 24 hours before repairing to minimize bowel contents in the stomach. Mice were divided into three groups (n = 3 per group): (1) no treatment; (2) suture; (3) S^3P repair. After the mice were anesthetized with pentobarbital sodium (50 mg kg^{-1}), their abdominal hair was removed. A 2 mm incisional defect was made to the stomach and colon by using an ophthalmic surgical scissor. The mice were placed on a heating pad during the surgery. For the suture group, the wound was continuously sutured using 8-0 surgical thread. S^3P repair group was given 100 μl bioadhesive solution and heated to 42 ℃ for 40 seconds by sonothermal. After treatment, the abdominal wall muscle and skin incision were closed with 6-0 sutures. 3 days after repair, the mice were sacrificed and measured the postoperative tissue adhesion (Extended Data Fig. 31). Animal experiments were approved by the Animal Ethics Committee at ShanghaiTech, and performed in accordance with the institutional guidelines.

Regarding the excessive bioadhesive in gastric perforation repair, we did not remove the excessive bioadhesive solution outside the animal after curing, because of its biocompatibility and biodegradability. The bioadhesive solution is composed of 0.5 wt% PAA-NHS, 7.5 wt%

HBCS, and 92 wt% water. The excess bioadhesive solution remaining uncured after printing will be diluted by the body fluid, and dispersed into the abdominal cavity. The HBCS will be absorbed and biodegraded by the tissue organ, while the PAA-NHS will also be biodegraded. We anticipate that some of the excess PAA-NHS have the chance be crossed linked to HBCS or form adhesion to tissue surface somewhere else, but will eventually be biodegraded. However, due to the interfacial water on tissue surface, the extra adhesion is neglectable. We have further confirmed the biosafety of leaving the excess bioadhesive solution inside the body by evaluating the side effects on other organs 3 days after treatment (Extended Data Fig. 30).

Extended Data Fig. 31g presents a statistical comparison of the postoperative adhesion rates under the three treatment conditions. In the no-treatment group (black bars), the adhesion rate is 100% for both the stomach and colon. In the suture group (blue bars), the adhesion rates are reduced to 70% for the stomach and 50% for the colon. Notably, in the S^3P group (red bars), the adhesion rates are significantly reduced to 20% for the stomach and 10% for the colon.

Characterization of Fourier-transform infrared (FTIR) characterizations. The chemical composition was characterized using a Fourier-transform infrared spectrometer (VERTEX 70, Bruker, Germany) in attenuated total reflectance (ATR) mode. The FTIR spectra were recorded by averaging 32 scans over a range from 600 cm^{-1} to 4500 cm^{-1}, with a resolution of 0.4 cm^{-1}.

We characterized the amidation reaction of our bioadhesive solution with FTIR analysis to provide molecular evidence to confirm the curing mechanism. Extended Data Fig. 13a shows the FTIR analysis on the bioadhesives before and after curing, validating the formation of amide bonds in the cured bioadhesive, and confirming that the curing of the bioadhesive is through the amidation between activated carboxyl groups and amino groups.

For analysis of the successful synthesis and long-term stability of PAA-NHS (Extended Data Fig. 12), we placed 5 mg of freshly synthesized PAA-NHS powder into a centrifuge tube, and

after adding 500 µl of water, we allowed it to soak for 24 hours. The water-absorbed PAA-NHS was then freeze-dried at -70°C to obtain a powdered sample. The freeze-dried PAA-NHS powder was analyzed and compared with the freshly prepared 5 mg PAA-NHS powder. We focused on the peak intensities at 1315 cm^{-1} and 1134 cm^{-1}, which correspond to the C-N-C stretching in NHS ester groups.

For analysis of the amidation reaction and under different concentrations of PAA-NHS and different PH conditions, we cured the bioadhesive on a hotplate at 42 °C for 5 minutes and compared it with the uncured bioadhesive solution, both of which were then freeze-dried at -70 °C for analysis (Extended Data Fig. 13a). Additionally, we prepared a bioadhesive solution with 0.4 wt% PAA-NHS to the bioadhesive precursor solution, cured it on a hotplate at 42 °C, and freeze-dried it at -70 °C for analysis. The spectra of this sample were compared with those of the bioadhesive containing 0.5 wt% PAA-NHS (Extended Data Fig. 13b). Furthermore, we placed the standard bioadhesive in a petri dish at pH = 6, cured it on a hotplate, and after freeze-drying, scanned it to evaluate the acid resistance of the cured bioadhesive (Extended Data Fig. 13c).

For analysis of the amidation reaction with sonothermal heating and hotplate heating, we cured the bioadhesive to 42 °C for 40 seconds using both sonothermal and hotplate heating (Extended Data Fig. 21a). To investigate the mechanism behind the faster curing of the bioadhesive with sonothermal treatment, we stirred the bioadhesive during heating at speeds of 1 mm/s, 3 mm/s, and 5 mm/s using a magnetic stirrer (Extended Data Fig. 21b). The bioadhesive samples from sonothermal heating, hotplate heating, and the three stirring speed gradients were then freeze-dried at -70°C. Infrared measurements were conducted to compare the quantity of amide bonds.

All of the FTIR data were analyzed by software of OPTUS. The stretching vibration absorption peak of carboxyl group C=O appeared at 1732 cm^{-1} indicated unreacted carboxyl groups of

PAA. The C=O absorption peak (amide I band) at 1639 cm^{-1} indicated that the carboxyl group in PAA reacted with the amino group in chitosan. The N-H bending vibration absorption peak in chitosan was at 1557 cm^{-1}. After the reaction, 1557 cm^{-1} also contains N-H bending vibration in the amide bond formed by the reaction of carboxyl group and amino group (amide II band).

Characterization of heat diffusion under single focal pressure with and without local circulation. To investigate the local circulation, we utilized Particle Imaging Velocimetry (PIV) to visualize the local circulation under single focal pressure (Extended Data Fig. 18b). The experimental setup consisted of a vision system, an illumination system, and tracer particles. The vision system featured a high-resolution microscopic camera, positioned in front of the water tank to capture a front view of the particles. The camera was capable of recording at 30 frames per second with a resolution of 2688 x 1512. The illumination system included a 532 nm laser generator, which excited the 1 μm fluorescent tracer particles. During the experiment, 6 mm of water containing tracer particles was added to the petri dish, and a single focal point was applied to the center of the water. Once the particle trajectories were captured, image preprocessing was performed to eliminate the stably trapped micro-particles. ImageJ was used to analyze the particle trajectories. Specifically, 60 images (corresponding to 2 seconds of video, as the camera captures 30 frames per second) were processed in the "image-stacks-Z Project-Max intensity" sequence.

To characterize the heat diffusion under single focal pressure with and without local circulation, we characterized the heating process with and without local circulation. Two 3-mm thick slices of the porcine stomach were placed in separate petri dishes and preheated to 39 °C. One group of stomach slices was exposed directly to air (Extended Data Fig. 18c), while the other group had a 1 mm thick layer of bioadhesive applied to the surface (Extended Data Fig. 18d). Both groups were then heated to 42 °C by single focal sonothermal. The temperature field changes

during the heating process were recorded using an infrared thermal camera, and the size of the area reaching 42 °C (Extended Data Fig. 18e) and the maximum temperature difference within that area were measured (Extended Data Fig. 18f). For the curve showing temperature inconsistency with time, due to the infrared camera's resolution of only 0.1 °C, the data were processed using nonlinear fitting and smoothing.

Characterization of the printing resolution with varying curing temperatures on different tissue types. To measure the printing resolution with varying temperatures on different tissue types (Extended Data Fig. 22), we sliced fresh porcine stomach, brain, and liver tissues into 3 mm thick sections and preheated them to 34 °C. The tissues were then placed in petri dishes, and a 1 mm layer of bioadhesive solution was applied. Using single focal heating, the tissues were heated to 37 °C, 39 °C, and 42 °C respectively maintained for 5 minutes, 3 minutes, and 40 seconds. Afterward, the uncured bioadhesive was washed off with PBS. The diameter of the cured bioadhesive was measured and recorded.

Characterization of the printing accuracy with varying pixel densities and pattern sizes on different tissue surfaces. To measure the printing accuracy with varying pixel densities and pattern sizes on different tissue surfaces (Extended Data Fig. 23), we sliced fresh porcine stomach, brain, and liver tissues into 3 mm thick sections and preheated them to 34 °C. The tissues were then placed in petri dishes, and a 1 mm layer of bioadhesive solution was applied. We used sonothermal heated tissues to 42 °C under sound patterns with diameters of 5, 10, and 15 mm for 40 seconds. Each sound pattern size corresponded to pixel densities of 1 pixel/mm², 9 pixels/mm², and 25 pixels/mm². After washing off the uncured bioadhesive with PBS, the diameter of the cured bioadhesive was measured and recorded.

***In vivo* assessment of sonothermal heating effects during S^3P treatment on IMQ-induced inflammation in mice**. C57BL / 6 mice (6–8 weeks, GemPharmatech) received a daily topical

dose of 62.5 mg IMQ cream (5%, Aldara, 3M Pharmaceuticals) on the shaved dorsal skin for 4 days. The inflamed mice were treated with S^3P on the dorsal skin and without treatment 24 h after the last IMQ treatment. The mice were then sacrificed and the skin samples were collected and analyzed using hematoxylin and eosin (H&E) staining. For epidermal thickness measurement, the mean values were calculated from five random area measurements in three different regional images of independent biological replicates using CaseViewer. Animal experiments were approved by the Animal Ethics Committee at ShanghaiTech, and performed in accordance with the institutional guidelines.

Minimally invasive printing of triangular bioadhesive on mouse kidney. For *in vivo* minimally invasive printing of triangular bioadhesive on mouse kidney, C57BL / 6 mice (6–8 weeks, GemPharmatech) was anesthetized with pentobarbital sodium (50 mg kg^{-1}). Then the mouse was injected subcutaneously in the neck with 200 µl of iohexol contrast agent. After 10 mins, the mouse was scanned by the micro-CT with normal posture. Then the mice were removed and placed on the printing platform carefully in same posture. In the end of this process, the center of mouse was perfectly aligned with the platform's center. We obtained the position of kidney relative to the center of the mouse from micro-CT image to direct injecting bioadhesive solution process and printing process. Before the printing, we converted the kidney location to the printer's absolute coordinates using a transformation matrix. 200 µl bioadhesive solution with iohexol was injected into the mice. Then the mouse was heating to 42 ℃ locally with a triangular sound image for about 40 seconds by S^3P. After printing, the mouse was scanned by micro-CT and surgically opened to show the cured triangular bioadhesive.

Xenograft assay and minimally invasive drug delivery. Athymic nude immunodeficient mice were purchased from GemPharmatech. Mice were aged 4 weeks and subcutaneously implanted with 1.5×10^6 AGS GFP-luciferase cells. 14 days after the epitomic tumor cell

injection, the mice were randomized and enrolled into four groups (untreated, intraperitoneal injection (IP), tail vein injection (IV), and S^3P groups; n = 7 per group) when animals met enrolment criteria of either visible tumor or a luminescence reading of 10^7 photons s^{-1}. After randomization, no blinding was performed. The groups were without treatment or treated with 100 μL of 1.5mg ml^{-1} oxaliplatin (HY-17371, MedChemExpress) via IP, IV, and S^3P respectively at different time points (14^{th}, 16^{th}, 18^{th}, and 20^{th} days). Tumor growth was measured by IVIS bioluminescence at the indicated times. Body weight was recorded throughout the experiment. At the end of the experiment (24 days), the mice were sacrificed. The tumors were then collected and analyzed using hematoxylin and eosin (H&E) staining. Animal experiments were approved by the Animal Ethics Committee at ShanghaiTech, and performed in accordance with the institutional guidelines.

***In vivo* imaging and quantification.** Mice bearing AGS-GFP-luciferase cells were injected intraperitoneally with 15 mg ml^{-1} firefly d-luciferin (MeilunBio, MB1834; 10 μl g^{-1} per mouse). Bioluminescence images were taken 5 mins later luciferase injection using the IVIS Lumina III imaging system (PerkinElmer). Anesthesia was administered throughout image acquisition (isoflurane 1.5% in O_2 at 21 min^{-1}). The Living Image v.4.4 software (PerkinElmer) was used to generate a standard region of interest (ROI) encompassing the largest tumor at the maximal bioluminescence signal. The identical ROI was used to determine the average radiance (photons s^{-1}) for all xenografts.

Histology and immunofluorescence. For hematoxylin and eosin (H&E) staining, fixed tissue samples were embedded in paraffin, mounted on the microscope slides, and stained with H&E. The paraffin sections were immersed sequentially in the following solutions: (1) dewaxing transparent agent (60722ES76, Yeasen) I for 20 mins; (2) dewaxing transparent agent II for 20 mins; (3) absolute ethanol I for 5 mins; (4) absolute ethanol II for 5 mins; (5) 75% alcohol for

5mins. And then rinsed with tap water. Put sections into hematoxylin solution for 3-5 mins, followed by rinsing with tap water until the stain turned blue (about 15 mins). The sections were then placed in 95% ethanol for 1 min, and eosin stain for 15 s. To dehydrate the sections, they were immersed sequentially in (1) absolute ethanol I for 2 mins; (2) absolute ethanol II for 2 mins; (3) absolute ethanol III for 2 mins; (4) normal butanol I for 2 mins; (5) normal butanol II for 2 mins; (6) xylene I for 2 mins; (7) xylene II for 2mins. Finally, the sections were mounted using a resin-based mounting medium.

For immunofluorescence, the paraffin-imbedded fixed tissues were sliced and prepared into slides. The slides were then deparaffinized in xylene and rehydrated in graded ethanol series, and underwent antigen retrieval using the steam method. Then, Put the slide in PBS (PH 7.4) and shook it on a decoloring shaker for 3 times, each time for 5 mins. After washing, non-specific antigen was blocked with 3% BSA. The slides were incubated in primary antibodies [rabbit anti-Ki67 (GB111499, Servicebio, 1:500); mouse anti-CD31 (GB123151, Servicebio, 1:1,000)] at 4 ℃ overnight. The slides were then washed three times with PBS–Tween 20 and incubated with CY3 goat anti-rabbit (GB21303, Servicebio, 1:300) or Alexa Fluor 488 goat anti-mouse secondary antibody (GB25301, Servicebio, 1:400) at room temperature for 60 mins in the dark. The slides were washed in PBS-Tween 20 three times for 5 mins per cycle. Then, the slides were incubated with fluorescent mounting medium with 4′,6-diamidino-2-phenylindole (DAPI), and the slides were washed in PBS and then counterstained with propidium iodide solution for 20 mins. An integrated tissue cytometer (TissueGnostics, Tissue FAXS Plus) was used for image acquisition. ImageJ (version 1.48) was used to quantify the fluorescence intensity of expressed antibodies. All the images were converted to the 8-bit binary images, and fluorescence intensity was calculated with normalized analysis.

Statistical analysis. GraphPad Prism (version 10.1.2) was used to assess the statistical significance of all comparison studies in this work. Data distribution was assumed to be normal for all parametric tests but not formally tested. In the statistical analysis for comparison between multiple groups, one-way analysis of variance (ANOVA) followed by Tukey's multiple comparison test was conducted with the significance threshold of $*P < 0.05$, $**P \leq 0.01$, and $***P \leq 0.001$. In the statistical analysis between grouped data, two-way ANOVA was conducted with the significance threshold of $*P < 0.05$, $**P \leq 0.01$, and $***P \leq 0.001$. In the statistical analysis between two groups, if both groups were assumed to have the same standard deviation (SD), a two-sided Student's *t*-test was performed with the significance threshold of $*P < 0.05$, $**P \leq 0.01$, and $***P \leq 0.001$, If the assumption of equal SDs was not met, a two-sided *t*-test with Welch's correction was used.

Simulation. To simulate the breaking of interfacial water on tissue surface (Extended Data Fig. 19a, b, Video S2), COMSOL Multiphysics 6.1 is employed in a three-step simulation process within a 25 × 40 mm^2 2D axisymmetric component to model acoustic and flow field, as well as particle tracking. Initially, the Pressure Acoustics, Frequency Domain Interface calculates the acoustic field, assuming a free space environment to omit sound reflections, using a normal displacement sound source to create a focal point. This sound source, with a vibration amplitude of 74.8 pm and a 50 mm diameter, generates a focal point over an area of 2.8 mm by 0.5 mm, centered 33 mm above the source on the symmetry axis. Subsequently, the flow and phase field simulations utilize this acoustic data to compute volume forces, focusing on the water layer above 33 mm, with properties set for the hydrogel and water and calculated using the Turbulent Flow, k-ε Interface, the Phase Field Interface, and their coupling feature. To ensure stability, specific discretization methods and a step function for volume forces are set. Finally, the Particle Tracing for Fluid Flow Interface releases and tracks 100 nm particles (density, 1050 kg/m^3), over a grid along the lateral axis (1-24 mm) and vertical axis (34-39 mm)

in this modeled environment. This comprehensive simulation provides insights into acoustic manipulation and particle behavior in a controlled fluidic system.

To simulate the acoustic streaming inside the water, COMSOL Multiphysics 6.1 is employed (Extended Data Fig. 18a, Video S4). To further simplify the problem, 2D component is choose to model the physical process. For geometric settings, we first draw a circle at the origin with radius 1 cm, add a 1 mm thick layer on this circle. Then, draw another circle at the origin with radius 2 mm. The propose of draw the small circle is to provide a domain where we can assign the mesh in this domain be finer, since this domain is where the vortex located. After that, use line $y = 0$ to cut the whole domain apart. The lower part of the domains will become the solid domain, and the upper part of the domain will become the liquid domain. Finally, delete the left part of the domains with boundary $x = 0$. The final geometry settings and material assignments are shown below:

For material settings, the liquid material is water, and its physical parameters are in default. The solid material is Polystyrene, its physical parameters are also in default.For physical interfaces, we first assign two arc-shaped domains be "Pressure Acoustics, Frequency Domain". "Cylindrical Wave Radiation" boundary condition is used to avoid secondary reflection, and then use "Incident Pressure Field" to apply incident pressure field. Since the domain is in circle shape, the phase of the incident sound field is uniform. Amplitude of the incident soundwave is $p_0 = 0.1$ MPa, but we truncate it with condition $|\theta\text{-}90°| < 15°$, where $\theta = \text{atan2}(y, x)$ is the azimuth angle of the point at the boundary. We also use "Symmetry" boundary condition to boundaries at line $x = 0$. The remain liquid domains are assigned with "Thermoviscous Acoustics, Frequency Domain" interface. All settings inside this interface remain default, except adding "Symmetry" boundary condition to boundary at line $x = 0$. Also, "The Laminar Flow Interface" are assigned to same domains. Similarly, we adding "Symmetry" boundary condition to boundary at line $x = 0$. To guarantee the convergence of the calculation, we assign

the hydraulic pressure at the origin be 0. Other conditions remain as default. The solid domain is assigned with “The Solid Mechanics Interface”. Similarly, all settings inside this interface remain default, except adding “Symmetry” boundary condition to boundary at line $x = 0$. After that, “The Particle Tracing for Fluid Flow Interface” is used to show the trajectories of particles in the fluid. Radius and density of the particles are in default. Use “Release from Grid” to release the particles, particles have no initial velocity. Add a domain force “Drag force”, and cite the velocity field as the field in “The Laminar Flow Interface”. Wall condition in is set to be “Disappear”.

The “Pressure Acoustics, Frequency Domain” interface and “Thermoviscous Acoustics, Frequency Domain” interface are connected by “Acoustic-Thermoviscous Acoustic Boundary” multiphysics branch. Also, the “Thermoviscous Acoustics, Frequency Domain” interface and “The Solid Mechanics Interface” is connected by “Thermoviscous Acoustic-Structure Boundary”. The “Laminar Flow” interface is coupling with “Thermoviscous Acoustics, Frequency Domain” through “Acoustic Streaming Domain Coupling” multiphysics branch.

For mesh generation, the small quadrant domain needs a very thin mesh, the maximum element size is about 20 μm. For other domain which involved in Laminar Flow interface, the maximum element is about 80 μm. Mesh of solid domain is relatively rough, the maximum element size is 500 μm.

For calculation, we first use “Frequency Domain” research step to calculate sound field distribution. Then use “Stationary” research step to calculate acoustic streaming. Finally, use “Time Dependent” research step to calculate particle tracing interface. Time step of the simulation is 10 milliseconds, and the duration is 10 seconds.

Extended Data Figures and Tables

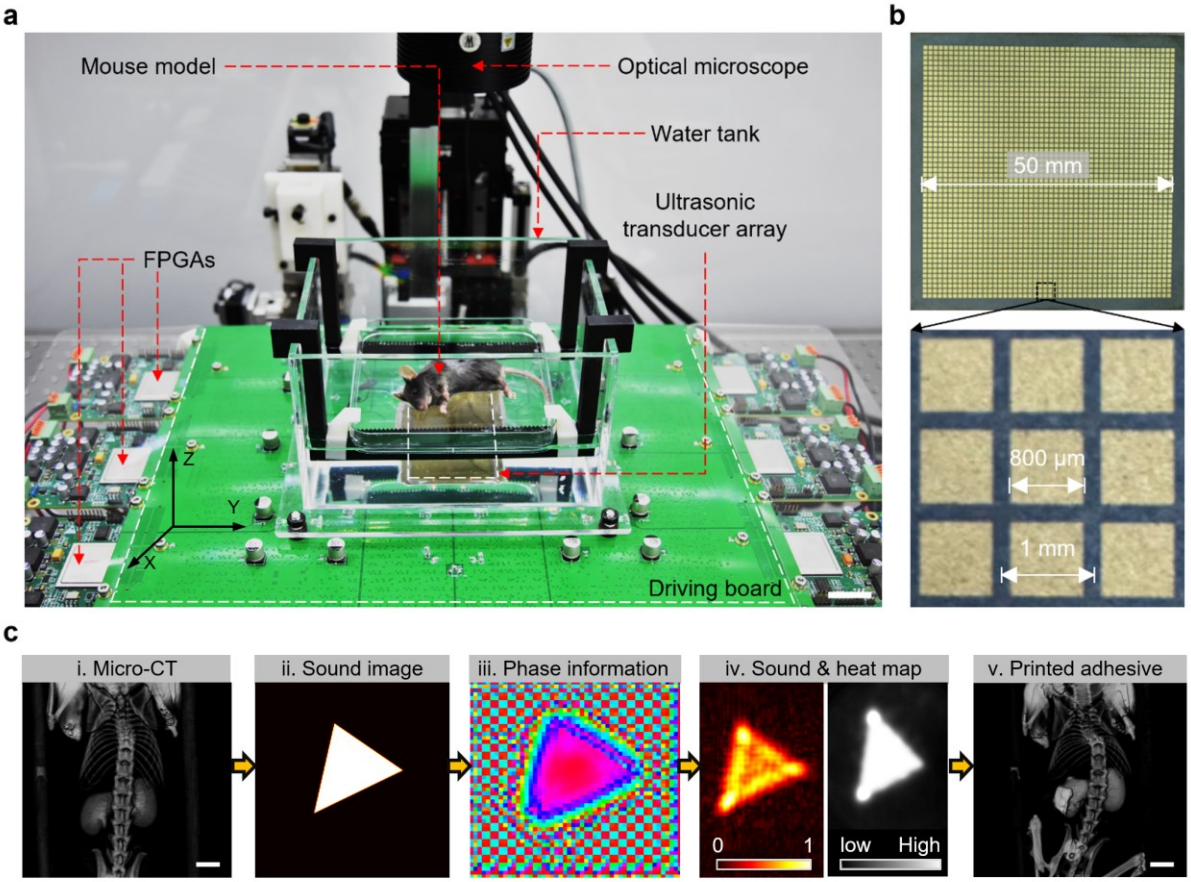

Extended Data Fig. 1 | The prototyped sound printing system for proof-of-concept study of minimally invasive delivery of bioadhesive in deep tissue. a, Overview of the sound printing system. The system features an ultrasonic transducer array emitting modulated sound waves. A specially designed driving board controlled by FPGAs to generate 2.32 MHz electrical square waves. Scale bar, 25 mm. **b**, Backside of the ultrasonic transducer array fabricated from PZT ceramic. The ultrasonic transducer array has a thickness of 1 mm, enclosing 50 × 50 array of square electrodes, essentially creating 2500 densely packed vibration sources under the actuation of the driving board. **c**, Working pipeline using the stablished system for minimally invasive sound printing of bioadhesive in deep tissue inside a mouse model. i. we use micro-CT to inspect the mouse model to determine the position and geometry of the required bioadhesive to be delivered; ii. then, we obtain an expected sound image adequately covering the clinical need; iii. using the ultrasound beamform algorithm (see methods), we get the phase information, based on which the driving board modulates the 2.32 MHz electrical square waves; iv. the ultrasonic transducer array will generate a sound image upon the target tissue surface, where will be heated up by sonothermal effect; v. the bioadhesive solution will be cured once the temperature gets higher than 37 °C, forming firm chemical bond to tissue surface. Scale bar, 3 mm.

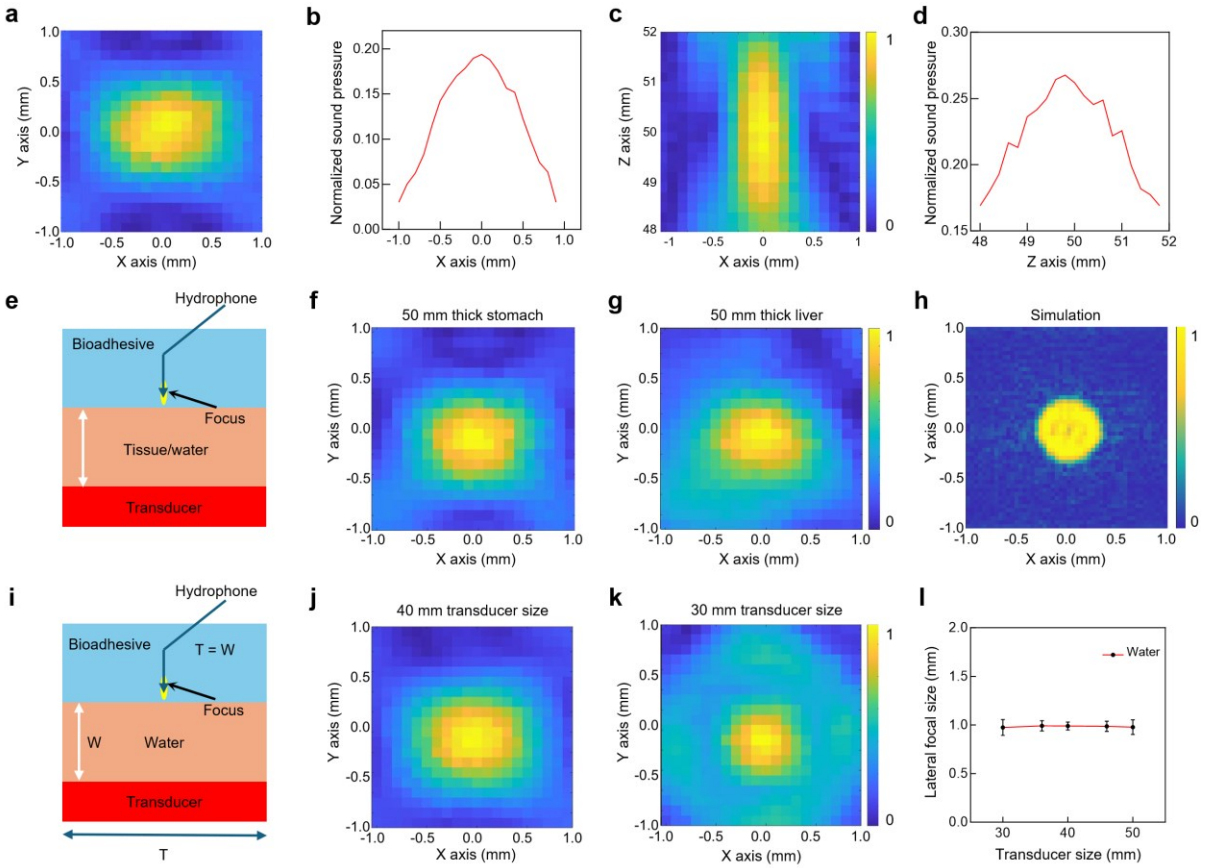

Extended Data Fig. 2 | Characterization of the sound patterning resolution of S^{3}P system and the impacts of tissue penetration and transducer size on sound patterning resolution. **a**, Single focal pressure profile at the XOY plane scanned by a hydrophone in water medium at the working distance of 50 mm away from the transducer plane (i.e., Z = 50 mm). **b**, Single focal pressure along X-axis. **c,** The single focal pressure profile at the XOZ plane. **d,** Single focal pressure along Z-axis. **e,** Schematic illustration of the characterization experiment over the impact of deep tissue penetration on sound patterning resolution. The transducer generates a single focal point at the plane of Z = 50 mm, and the transducer size is fixed 50 mm. A needle hydrophone is used to scan the sound pressure step by step (step size is 100 μm). Tissues of different types (e.g., porcine liver, stomach, and brain tissues) with different thicknesses (from 10 mm to 50 mm) are placed between the transducer plane and focal plane. **f-g,** The scanned focal profiles at the XOY plane after penetrating 50 mm thick stomach (**f**) and liver tissue (**g**). **h,** Simulated focal profile at the XOY plane generated by S^{3}P system. **i,** Schematic illustration of the characterization experiment over the impacts of transducer size on sound patterning resolution. Transducer size from 30 mm to 50 mm is evaluated. The working distance is set to be the transducer size. Working medium is water. **j-k,** The scanned focal profiles at the XOY plane with transducer size of 40 mm (**j**) and 30 mm (**k**). **l,** The measured lateral focal size (-6 dB attenuation) as a function of transducer size. The sound pressure is normalized.

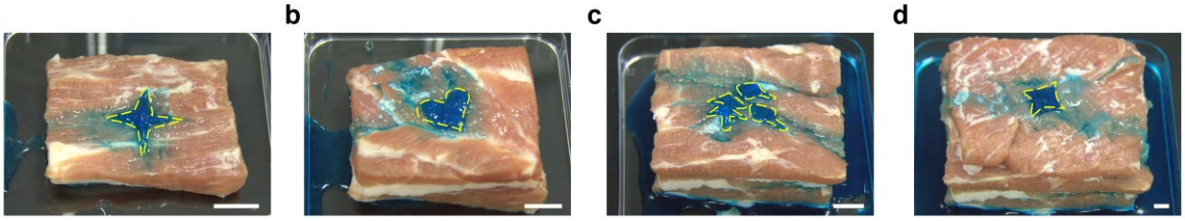

Extended Data Fig. 3 | Demonstration of deep-penetration capability of S^3P. The bioadhesive was printed on **a**, 1 cm, **b**, 2 cm, **c**, 3 cm, and **d**, 5 cm thick porcine muscular tissue surface with different patterns at room temperature of 24 ℃. The bioadhesives were stained in blue color for visualization. Scale bar, 2 cm.

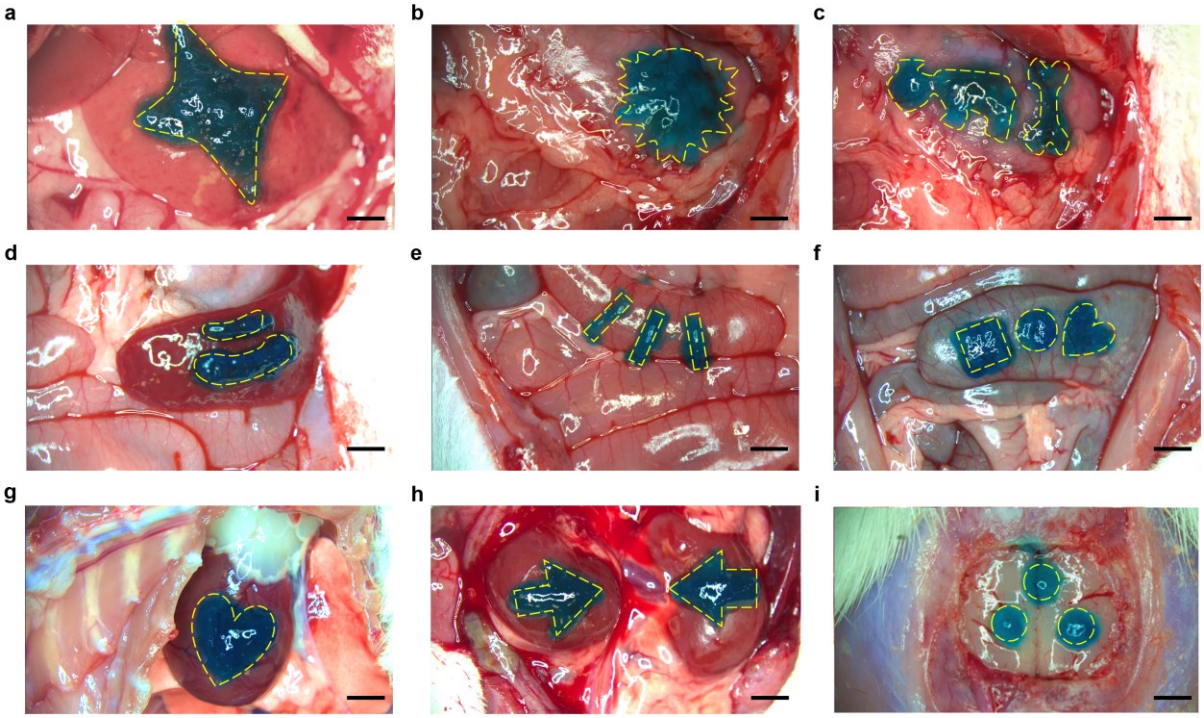

Extended Data Fig. 4 | Versatile applicability of S^{3}P on different tissue surfaces. The *in vivo* printed bioadhesive of different patterns on mouse **a**, liver, **b-c**, stomach, **d**, spleen, **e-f**, colon, **g**, heart, **h**, kidney, and **i**, brain tissue, exposed to room temperature. The yellow dashed lines indicate the designed patterns. The bioadhesives were stained in blue color for visualization. Scale bar, 3 mm.

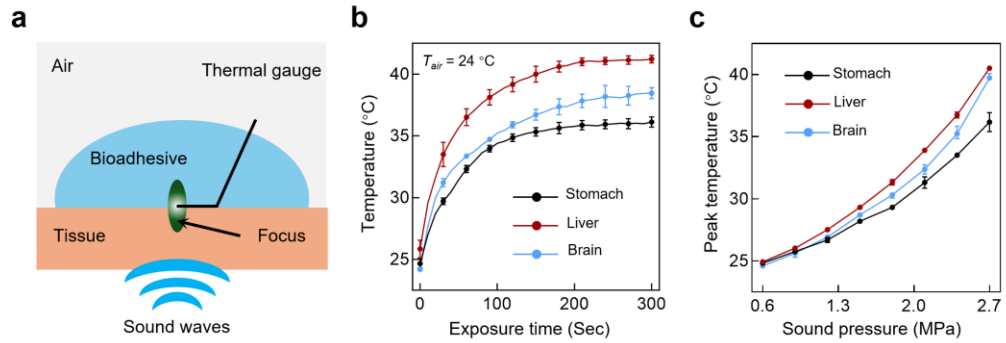

Extended Data Fig. 5 | Sonothermal effect characterization on tissue surface *in vitro*. a, Characterization scheme for sonothermal heating on various tissue surfaces covered by bioadhesive and exposed to focused ultrasound. **b**, Time-dependent temperature increase on mouse stomach, liver, and brain tissue surface at the sound focal zone under 2.75 MPa. **c**, Peak-temperature increase on mouse stomach, liver, and brain tissue surface at the sound focal zone exposed to varying sound pressures.

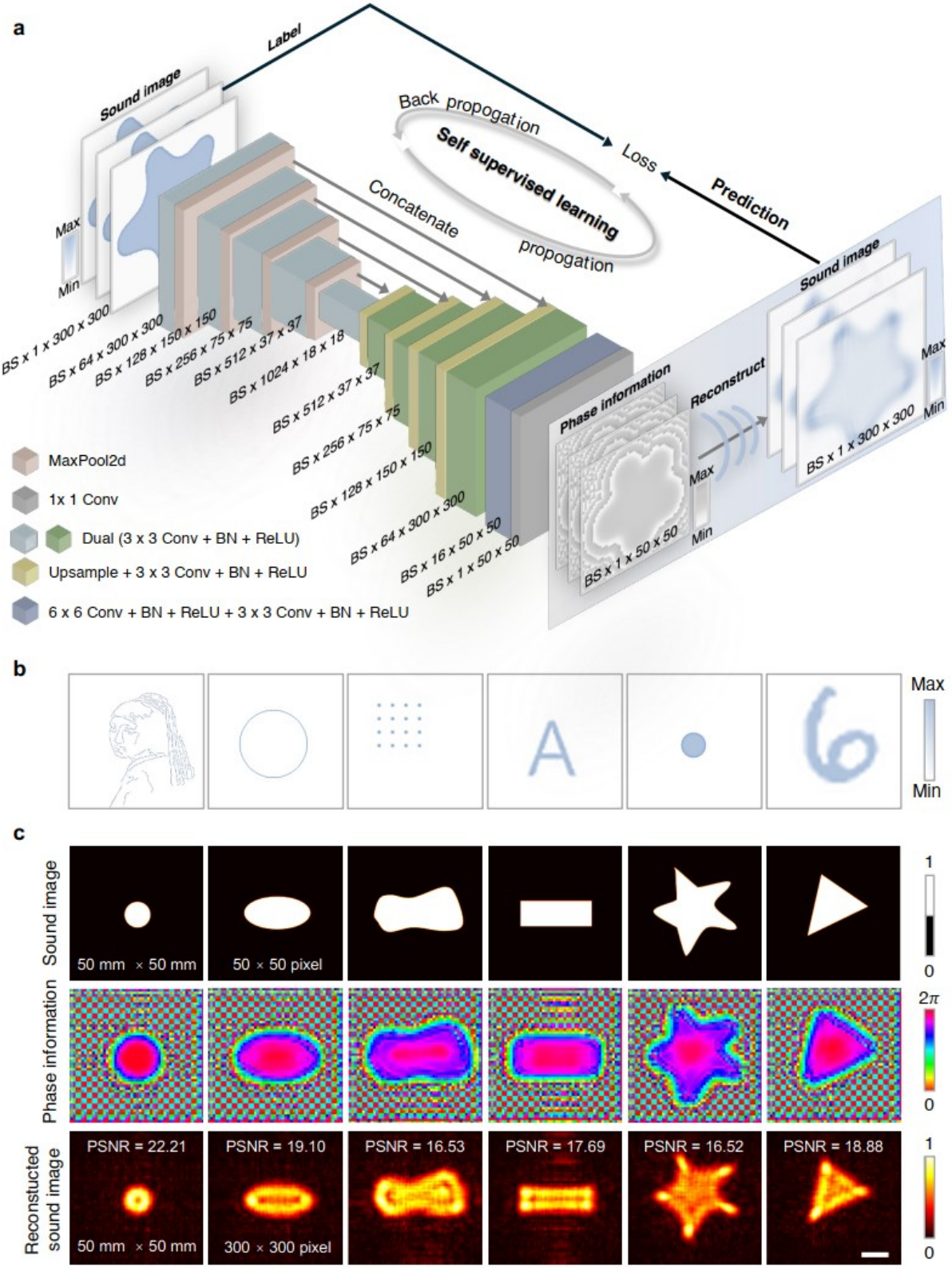

Extended Data Fig. 6 | Ultrasound beamforming algorithm. a, Schematic illustration of the developed deep-learning based ultrasound beamforming algorithm, where a deep neural network following the U-Net architecture trained by self-supervised learning is employed to compute the phase information given the desired sound images. **b,** Examples of the prepared sound image dataset meeting bioadhesive deployment requirements for network training. **c,**

Phase information produced by the well-trained network for given desired sound images, along with the corresponding reconstructed sound images (sound image reconstruction quality is evaluated by the peak signal to noise ratio (PSNR)). The sound wave propagation distance is 50 mm for the examples in (c). Scale bar, 10 mm.

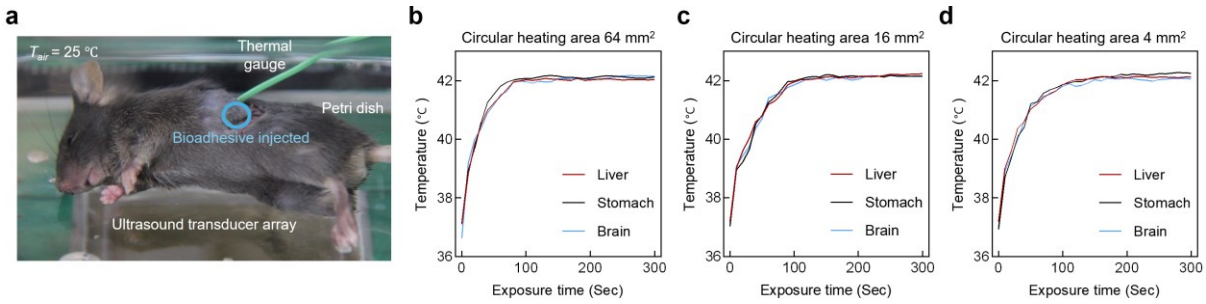

Extended Data Fig. 7 | Temperature control in S^{3}P. a, The setup for characterizing the temperature control in S^{3}P. A mouse (C57BL / 6, 6 weeks, GemPharmatech) was placed on the petri dish as in Extended Data Fig. 1a, while a thermal gauge (YET-620x, KAIPUSEN, China) was buried into the tissue with 0.5 mL of bioadhesive applied to fully cover the gauge tip. The mouse skin was then placed over the bioadhesive to mitigate the influence of the ambient temperature (room temperature T_{air} = 24 ℃). All experiments began once the bioadhesive temperature stabilized at the equilibrium temperature (~ 37 ℃). Scale bar, 3 mm. **b,** For a 64 mm^2 circular heating area (defined by the sound image), the required sound energy was 80%, 83%, and 88% of full power operation (9 Volts) for the liver, brain, and stomach respectively, to maintain the temperature at 42 ± 0.3 ℃. **c,** For a 16 mm^2 circular heating area, the required sound energy was 63%, 65%, and 70% of full power operation (9 Volts) for the liver, brain, and stomach respectively, to maintain the temperature at 42 ± 0.3 ℃. **d,** For a 4 mm^2 circular heating area, the required sound energy was 51%, 54%, and 59% of full power operation (9 Volts) for the liver, brain, and stomach respectively, to maintain the temperature at 42 ± 0.3 ℃. For all experiments in **b-d**, we conducted multiple experiments and all witnessed similar results.

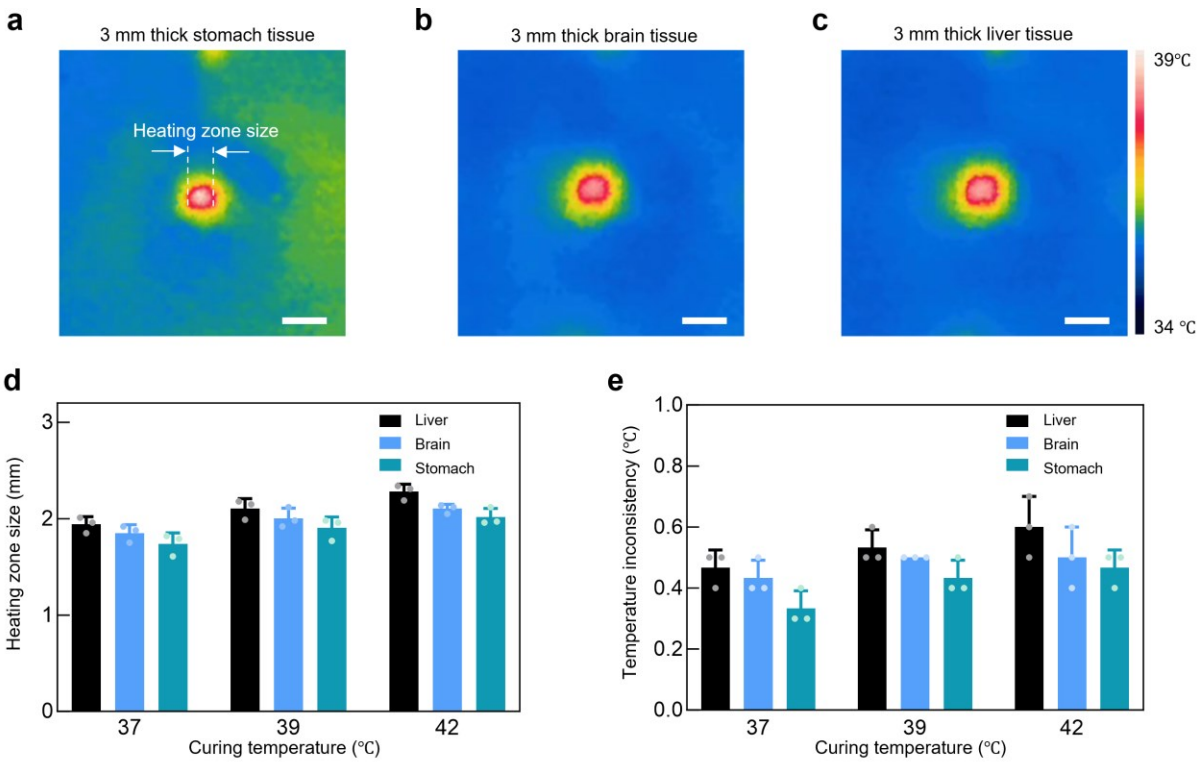

Extended Data Fig. 8 | Characterization of heat accumulation under single focal pressure on different tissue surfaces. a-c, Snapshots of stabilized infrared thermal images on the surface of porcine stomach (**a**), brain (**b**), and liver (**c**) tissues. The heating temperature in the three snapshots is 39 ℃. All tissues are 3 mm thick and covered by 1 mm thick bioadhesive solution. **d,** Heating zone size under different curing temperatures on different tissue surfaces. **e,** Temperature inconsistency within the heating zone under different curing temperatures on different tissue surfaces. The temperature inconsistency is measured by the difference the center temperature and the surrounding temperature of the heating zone. Data are represented as mean ±s.d. (n = 3). Scale bar, 5 mm.

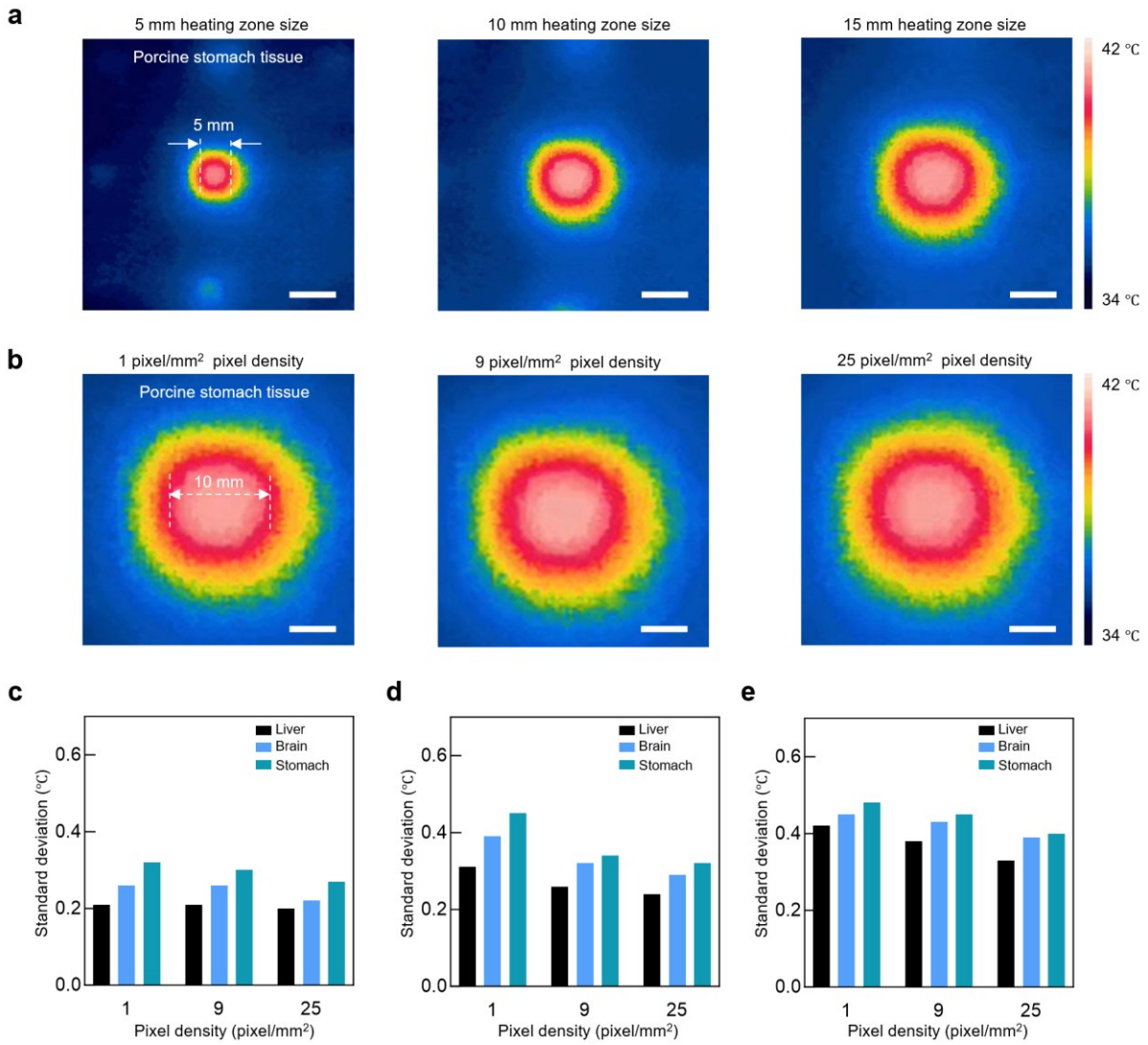

Extended Data Fig. 9 | Characterization of the heat accumulation under different sound pattern sizes and pixel densities on different tissue surfaces. a, Snapshots of the stabilized infrared thermal images of 5 mm, 10 mm, and 15 mm circular heating zone on 5 mm thick porcine liver tissue covered with 1 mm thick bioadhesive solution. The heating temperature is 42 ℃. Scale bar, 1 cm. **b,** Snapshots of the stabilized infrared thermal images of 10 mm heating zone on 5 mm porcine liver tissue covered with 1 mm thick bioadhesive solution with pixel density of 1, 9, and 25 pixel/mm². Scale bar, 5 mm. **c-e,** Standard deviation of the temperature within the heating zone heated on different tissues with different pixel densities over heating zone size of 5 mm (**c**), 10 mm (**d**), 15 mm (**e**).

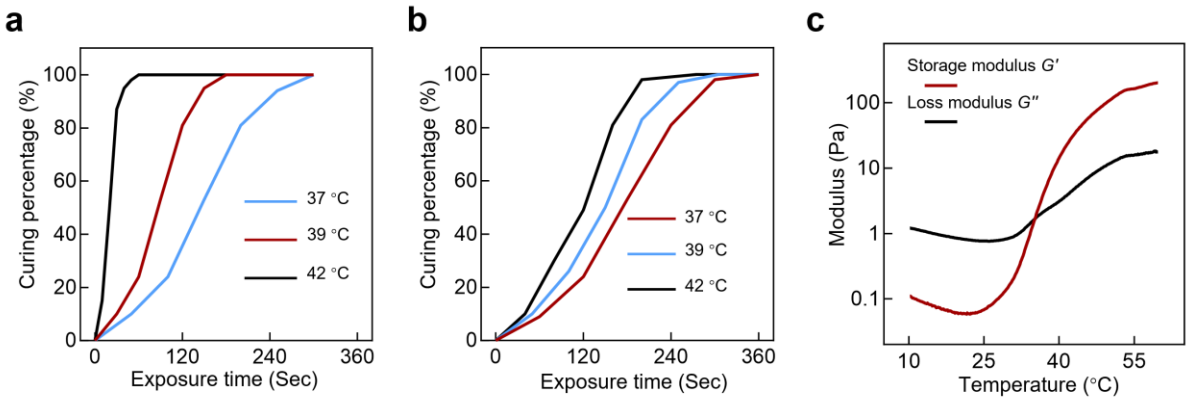

Extended Data Fig. 10 | Curing behavior of the thermosensitive bioadhesive used in S^{3}P. **a-b,** Curing ratio of bioadhesive measured by curing area as a function of time at 37 °C, 39 °C, and 42 °C under sonothermal heating (**a**) and hot plate heating (**b**). **c**, Oscillation temperature sweep depicting the storage modulus and loss modulus of the bioadhesive at the transition temperature.

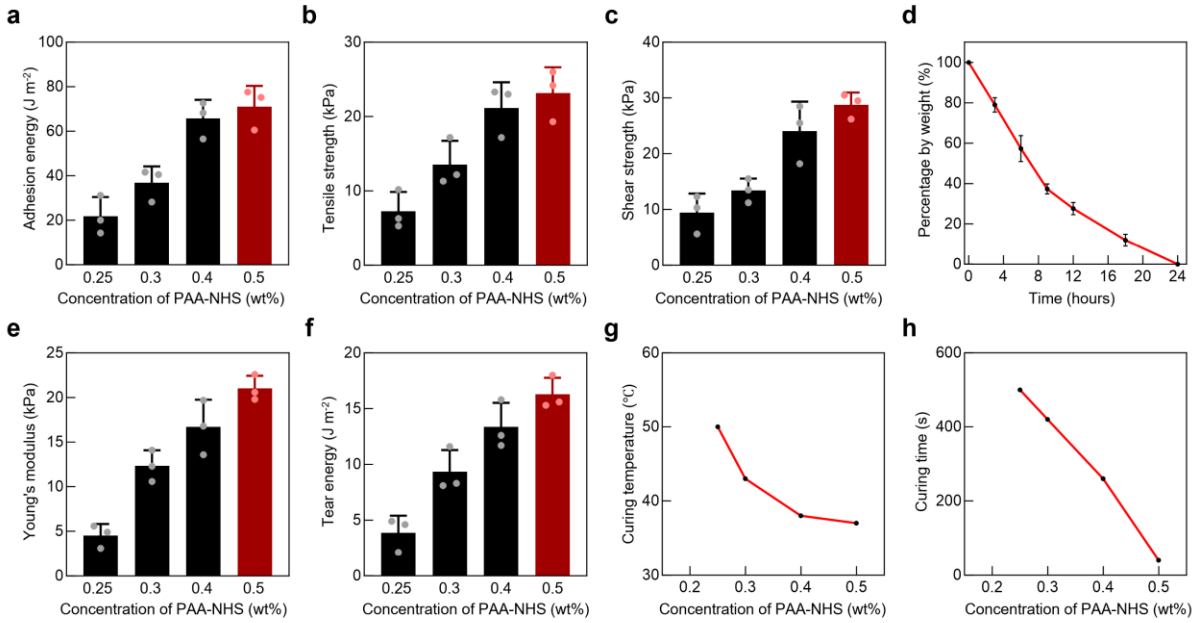

Extended Data Fig. 11 | Characterization of the adhesion performance, mechanical properties, curing behaviors, and biodegradability of PAA-NHS/HBCS formulation under different concentrations. a-c, Adhesion energy (**a**), tensile strength (**b**), and shear strength (**c**) of the bioadhesives cured by sonothermal heating on *ex vivo* rat colon with varying concentrations of PAA-NHS. The 0.5 wt% concentration (in red color) corresponds to the formulation used in S^3P. **d,** The degradation process of the sonothermally cured bioadhesive with the concentration of 0.25 wt% PAA-NHS and 4 wt% HBCS in PBS solution. **e-f,** The Young's modulus and tear energy of the bioadhesives cured by sonothermal heating on *ex vivo* rat colon with varying concentrations of PAA-NHS. The 0.5 wt% concentration (in red color) corresponds to the formulation used in S^3P. **g-h,** The curing temperature (**g**) and curing time (**h**) with varying concentrations of PAA-NHS under sonothermal heating. In (**g**), the curing temperature is 42 °C. In all figures, the data for the concentration of 0.25 wt% PAA-NHS refers to diluting the original bioadhesive solution to half its original concentration, while the other concentrations were obtained by individually adjusting the concentration of PAA-NHS. Data are represented as mean ± s.d. (n = 3).

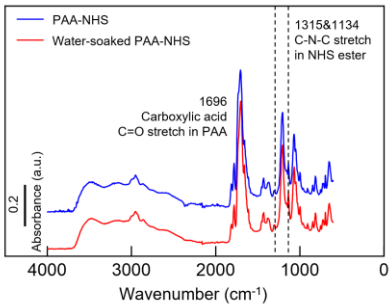

Extended Data Fig. 12 | FTIR analysis of the material synthesis and long-term stability of PAA-NHS. FTIR absorbance vs. wavenumber spectra for dry PAA-NHS powder and PAA-NHS after soaking in water for 24 hours. In FTIR spectra, peak at 1315 cm^{-1} and 1134 cm^{-1} correspond to C-N-C stretch in NHS ester groups; peaks at 1,696 cm^{-1} correspond to C=O stretch of carboxylic acid groups in PAA.

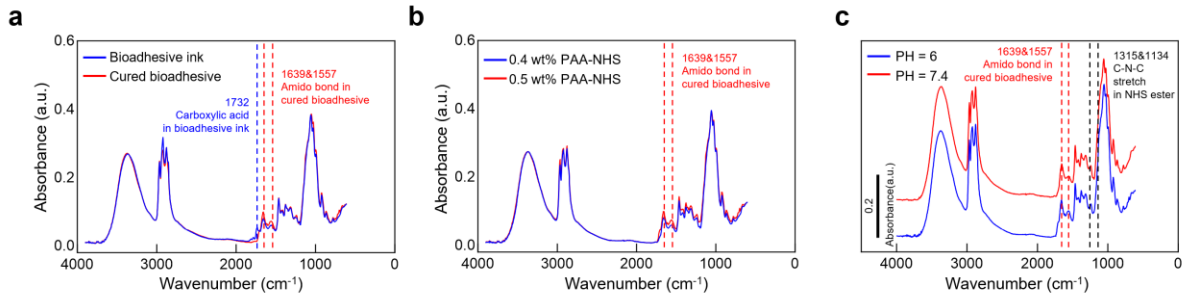

Extended Data Fig. 13 | FTIR analysis of the amidation reaction under different concentrations of PAA-NHS and different PH conditions. a, FTIR absorbance vs. wavenumber spectra of the bioadhesive solution before (blue) and after curing (red). **b**, FTIR absorbance vs. wavenumber spectra of cured bioadhesives with different concentrations of PAA-NHS. The 0.5 wt% (red) corresponds to the concentration used in S^3P. **c,** FTIR absorbance vs. wavenumber spectra of the bioadhesives cured under the PH level of 6 (blue) and 7.4 (red). All bioadhesives are cured at 42 ℃ under sonothermal heating. In FTIR spectra, peaks at 1557 cm^{-1} corresponds to N-H bending vibration and 1639 cm^{-1} correspond to C=O stretch of amide bond in cured bioadhesive; peak at 1732 cm^{-1} corresponds to C=O stretch of carboxylic acid of PAA in bioadhesive solution; peak at 1315 cm^{-1} and 1134 cm^{-1} correspond to C-N-C stretch in NHS ester groups.

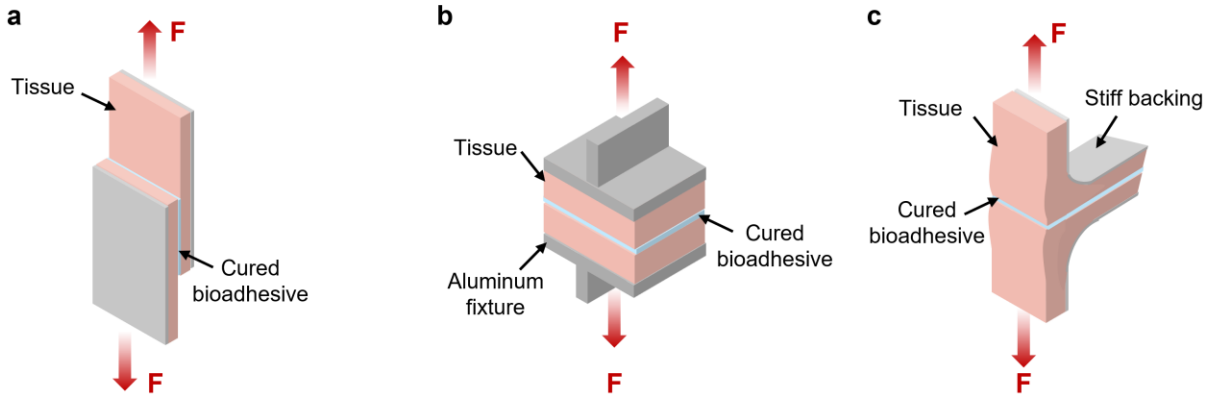

Extended Data Fig. 14 | Mechanical testing configurations for assessing adhesion performance. The testing setups for mechanical properties of the printed bioadhesive on tissue surfaces in terms of adhesion energy, tensile stress, and shear strength. **a**, Schematic of testing setup for shear strength based on the standard 180° peeling test. **b**, Schematic of testing setup for tensile stress based on the standard tensile test. **c**, Schematic of testing setup for adhesion energy based on the standard lap-shear test.

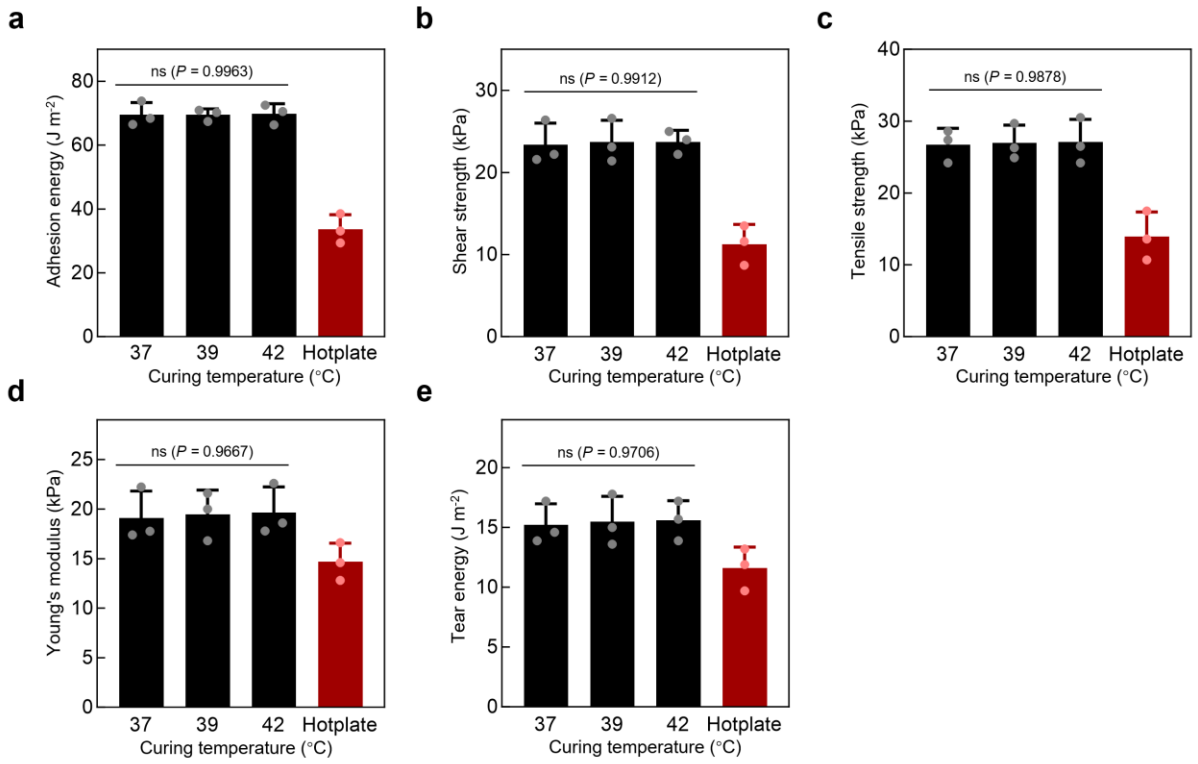

Extended Data Fig. 15 | Characterization of adhesion performance and mechanical properties of bioadhesives cured at different temperatures under sonothermal heating. a-c, Adhesion energy (**a**), tensile strength (**b**), and shear strength (**c**) of the bioadhesives cured by sonothermal heating (black) and hotplate heating (red) on *ex vivo* rat colon with varying curing temperatures. **d-e,** The Young's modulus (**d**) and tear energy (**e**) of the bioadhesives cured by sonothermal heating (black) and hotplate heating (red) on mice dorsal muscle *in vivo* with varying curing temperatures. In all figures, data from the hotplate curing group are obtained at 42 °C on a hotplate for 5 mins curing time. Data are represented as mean ± s.d. (n = 3). Statistical analysis was performed using a one-way ANOVA followed by Tukey's multiple comparison test; ns, not significant.

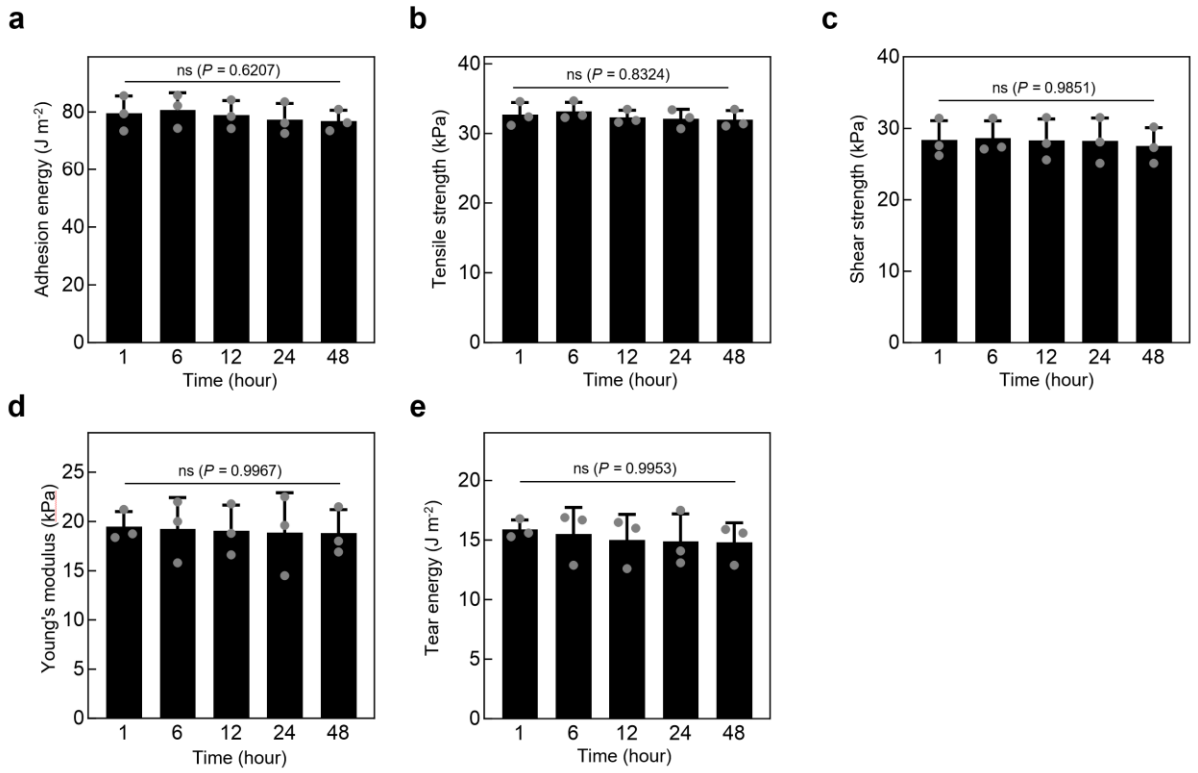

Extended Data Fig. 16 | Characterization of the long-term *in vivo* adhesion performance and mechanical properties of the delivered bioadhesives. a-c, Adhesion energy (**a**), tensile strength (**b**), and shear strength (**c**) of the delivered bioadhesion at different time after curing on mice dorsal muscle *in vivo*. **d-e,** The Young's modulus (**d**) and tear energy (**e**) of the delivered bioadhesives at different time after curing on mice dorsal muscle *in vivo*. All bioadhesives are cured by sonothermal heating at 42 ℃ for 40 seconds. Data are represented as mean ± s.d. (n = 3). Statistical analysis was performed using a one-way ANOVA followed by Tukey's multiple comparison test; ns, not significant.

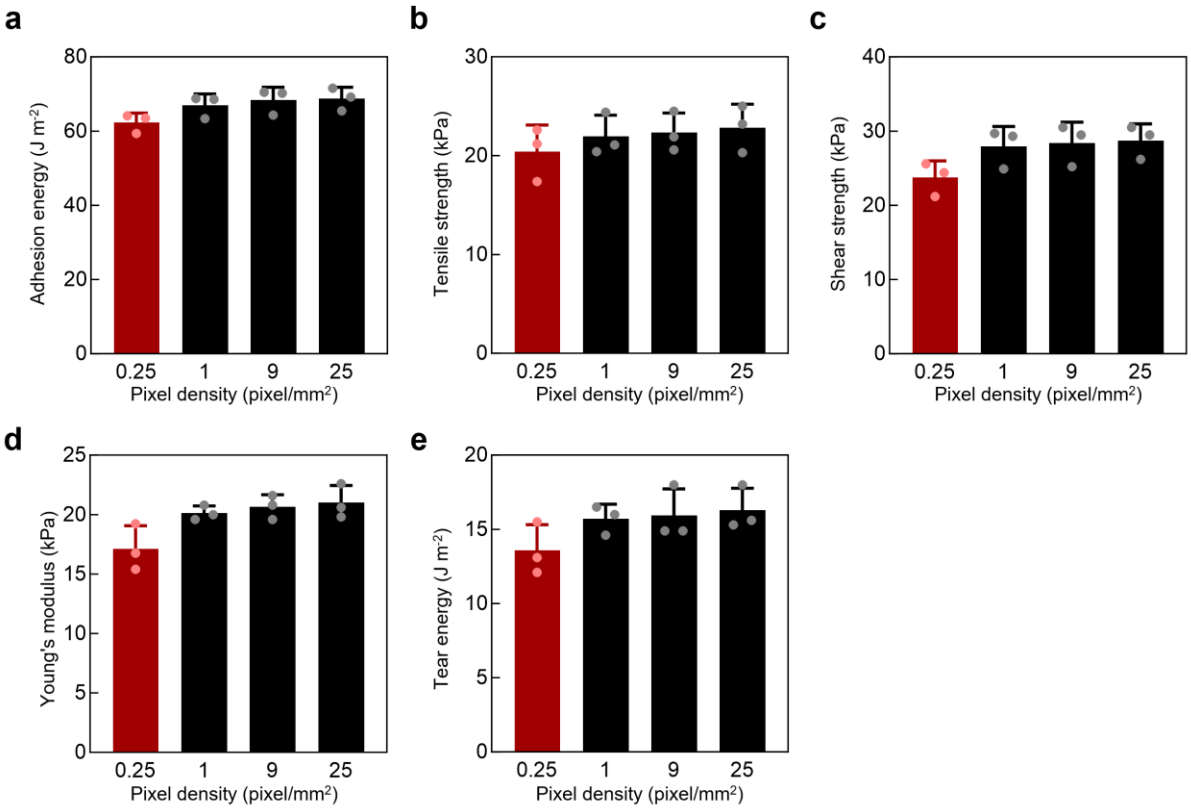

Extended Data Fig. 17 | Characterization of the adhesion performance and mechanical properties of bioadhesives cured at different pixel densities under sonothermal heating. **a-c,** Adhesion energy (**a**), tensile strength (**b**), and shear strength (**c**) of the bioadhesives cured by sonothermal heating on *ex vivo* rat colon with varying pixel densities. **d-e,** The Young's modulus (**d**) and tear energy (**e**) of the bioadhesives cured by sonothermal heating with varying pixel densities on mice dorsal muscle *in vivo*. All bioadhesives are cured by sonothermal heating at 42 °C for 40 seconds. From the spatial bandwidth product theory, our transducer array system physically supports the generation of sound images in the pixel density of 1 pixel/mm^2. The data obtained from the pixel density of 0.25 pixel/mm^2 (red) is for characterization purpose. Data are represented as mean ± s.d. (n = 3).

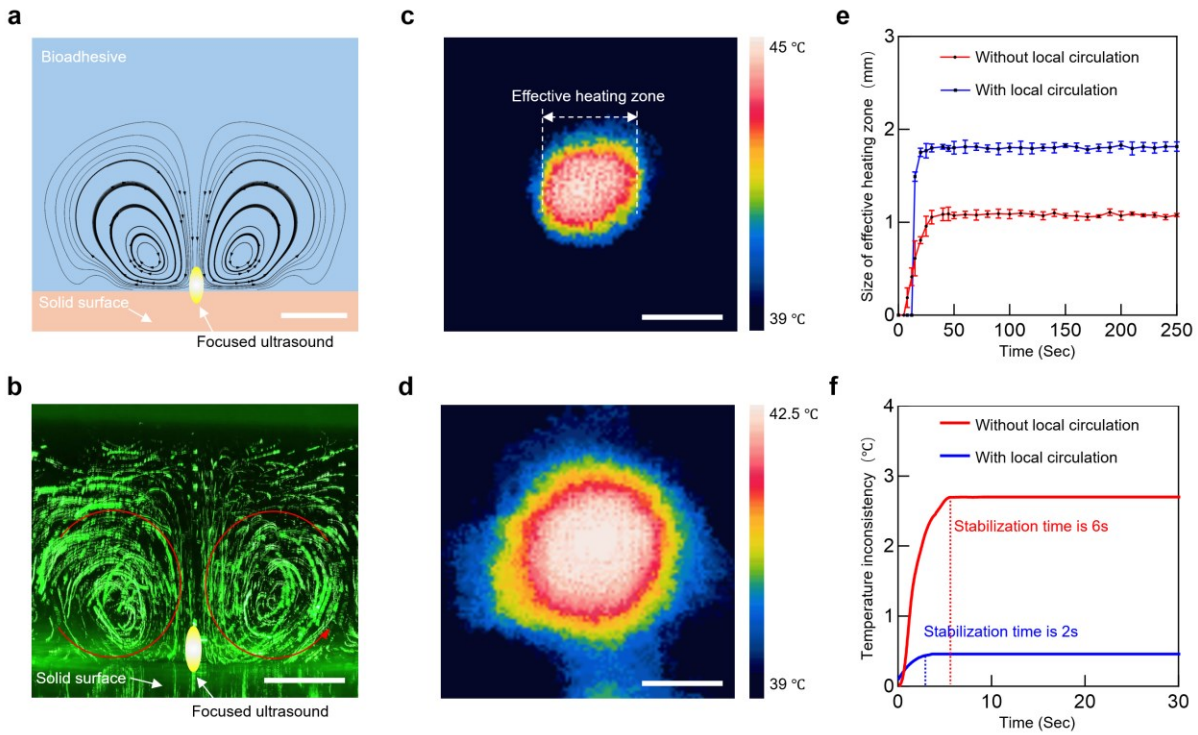

Extended Data Fig. 18 | Characterization of heat diffusion under single focal pressure with and without local circulation on porcine stomach tissue (Video S4). a, Simulation of the acoustic streaming induced local circulation under the boundary effect of tissue surfaces by COMSOL Multiphysics 6.1. **b,** Particle Imaging Velocimetry characterization of the local circulation formed on tissue surface. **c-d,** Snapshots of the stabilized infrared thermal image under singe focal heating on porcine stomach to 42 °C without (**c**) and with (**d**) local circulation. In (**c**), the tissue surface is naked to air, while in (d), the tissue is covered by 1 mm thick bioadhesive solution. **d,** Thermal field image of single-point heating on porcine stomach to 42 °C for 40 seconds with local circulation. **e,** Time dependent size of the effective heating zone (where the temperature reaching the curing temperature of 42 °C) with (blue) and without (red) local circulation. **f,** Time dependent temperature inconsistency (measured by the difference between the center temperature and the surrounding temperature) of the effective heating zone (where the temperature reaching the curing temperature of 42 °C) with (blue) and without (red) local circulation. Data are represented as mean ± s.d. (n = 3). Scale bar, 1 mm.

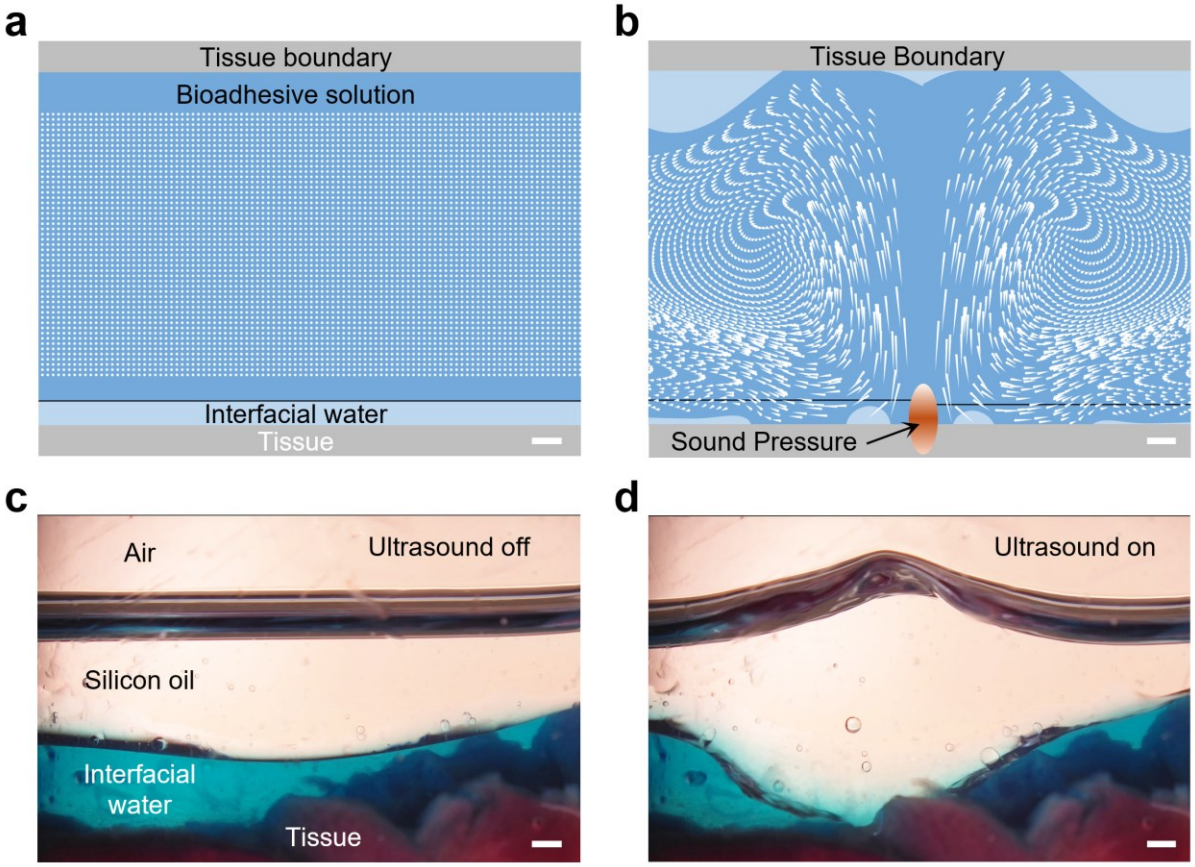

Extended Data Fig. 19 | Sound pressure induced fluidic streaming on tissue surface. The focusing of sound pressure upon tissue surface will induce fluidic streaming within the interfacial water layer between the tissue surface and the bioadhesive solution, which in turn facilitates the permeation of PAA-NHS into the interfacial water on wet tissue surfaces. **a**, Simulation setup for COMSOL Multiphysics 6.1. The interfacial water layer assumed to be 500 μm thick. The white particles are used to indicate the flow pattern, mimicking the motion of PAA-NHS inside the bioadhesive solution. **b**, Simulation results of local fluidic streaming illustrated by particle tracks under single focused ultrasound. The interfacial water layer is broken by the local fluidic streaming. Scale bar, 500 μm. **c-d**, Experimental visualization of the sound pressure induced fluidic streaming upon tissue surface. For better visualization, we covered about 1 mm thick water upon kidney tissue to mimic the interfacial water layer, and used silicon oil with similar viscosity upon water to mimic the hydrogel solution. The two immiscible liquids can better illustrate the permeation of bioadhesive solution into the interfacial water layer. Before exposure to ultrasound (**c**), the silicon oil is isolated from contacting with the tissue; once exposed to ultrasound (**d**), the sound pressure induced fluidic streaming facilitates the permeation of bioadhesive solution into the interfacial water layer (see Video S2 for more details). Scale bar, 500 μm. In both simulation and experiment, we used single focused ultrasound.

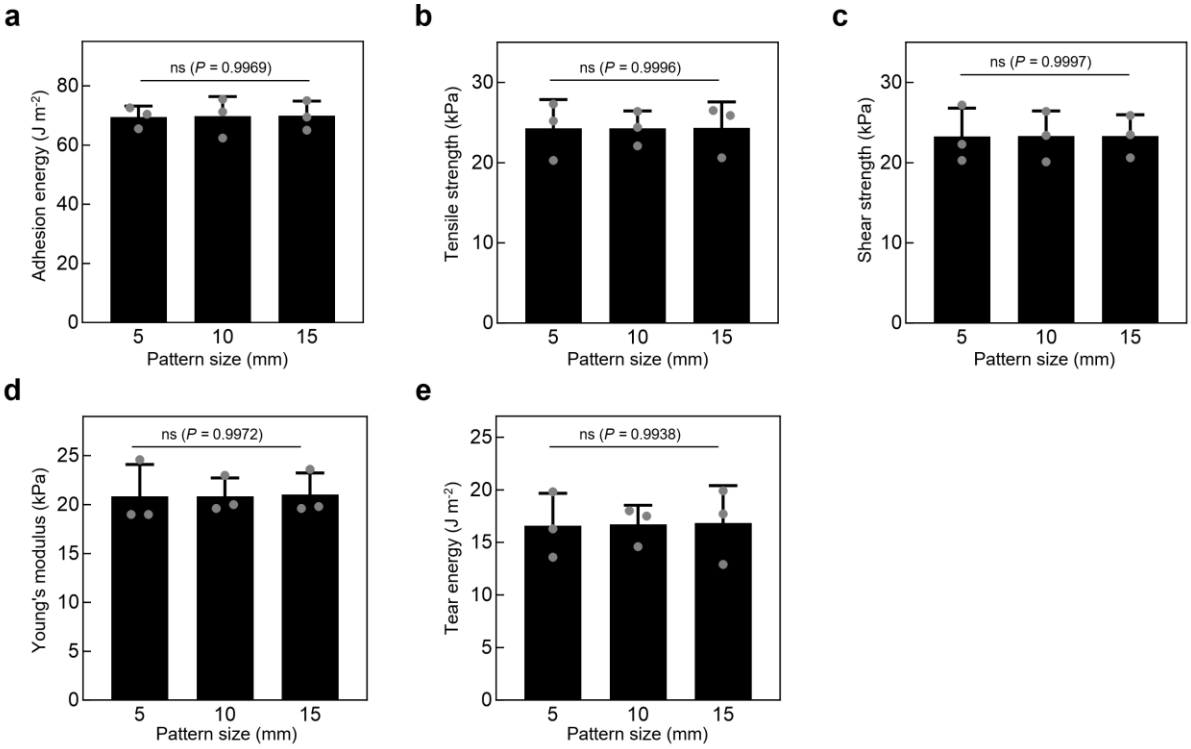

Extended Data Fig. 20 | Characterization of the adhesion performance and mechanical properties of bioadhesives cured at different pattern sizes under sonothermal heating. a-c, Adhesion energy (**a**), tensile strength (**b**), and shear strength (**c**) of the bioadhesives cured by sonothermal heating on *ex vivo* rat colon with varying pattern sizes. **d-e**, The Young's modulus (**d**) and tear energy (**e**) of the bioadhesives cured by sonothermal heating with varying pattern sizes on mice dorsal muscle *in vivo*. All bioadhesives are cured by sonothermal heating at 42 °C for 40 seconds. Data are represented as mean ± s.d. (n = 3). Statistical analysis was performed using a one-way ANOVA followed by Tukey's multiple comparison test; ns, not significant.

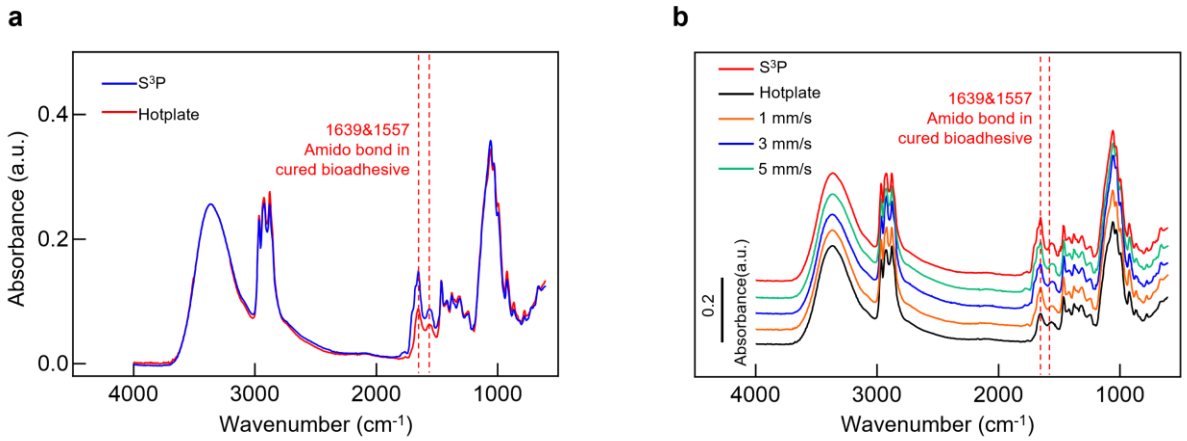

Extended Data Fig. 21 | FTIR analysis of the amidation reaction with sonothermal heating and hotplate heating. a, FTIR absorbance vs. wavenumber spectra of the bioadhesives cured by sonothermal heating (blue) and hotplate heating (red). The bioadhesives are cured at 42 ℃ for 40 seconds in sonothermal heating and 3 mins in hotplate heating. **b**, FTIR absorbance vs. wavenumber spectra of the bioadhesives cured by hotplate heating mixed by magnetic stirring. In FTIR spectra, peaks at 1557 cm^{-1} corresponds to N-H bending vibration and 1639 cm^{-1} correspond to C=O stretch of amide bond in cured bioadhesive; peak at 1732 cm^{-1} corresponds to C=O stretch of carboxylic acid of PAA in bioadhesive ink; peak at 1315 cm^{-1} and 1134 cm^{-1} correspond to C-N-C stretch in NHS ester groups.

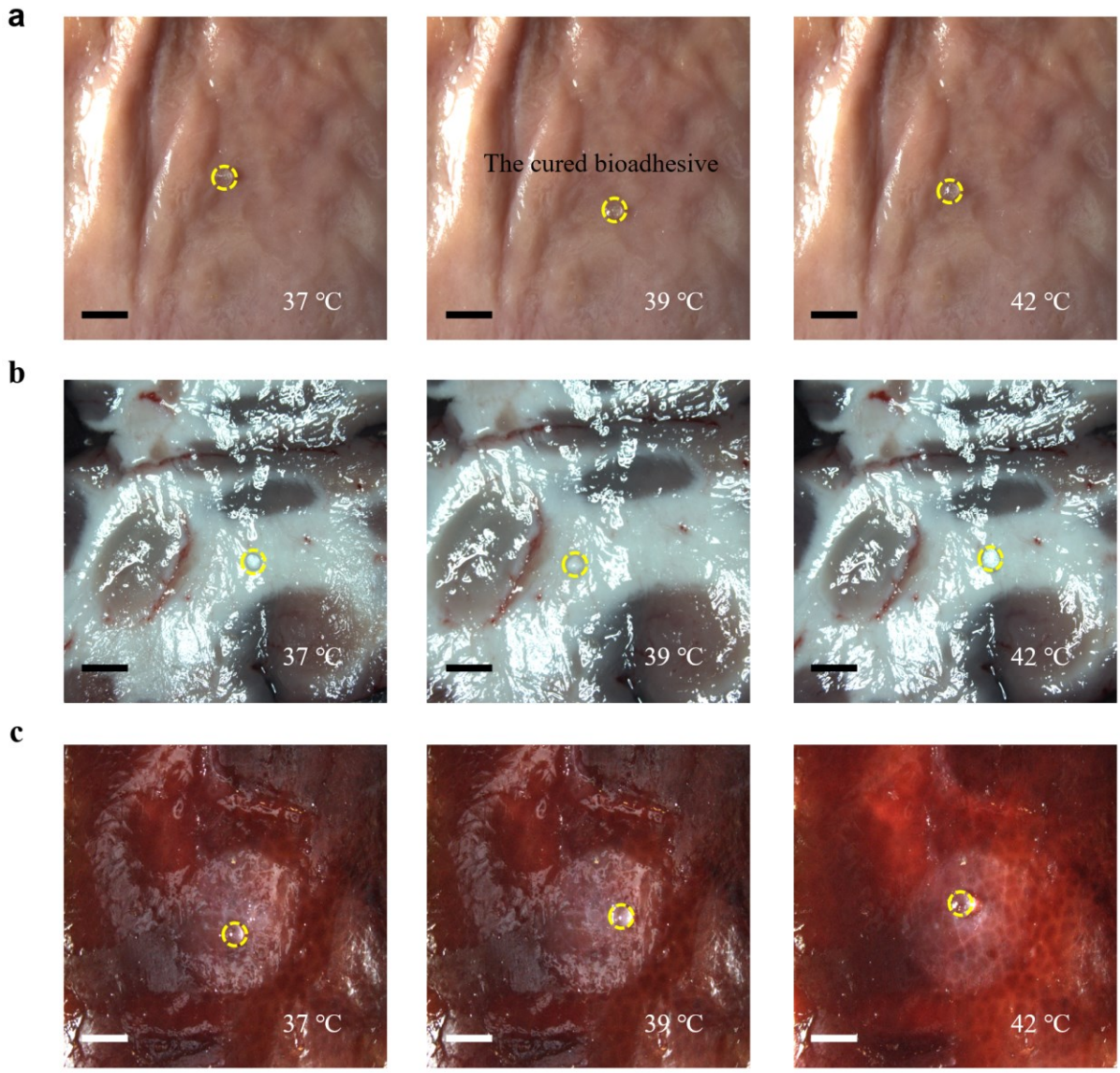

Extended Data Fig. 22 | Characterization of the printing resolution with varying curing temperatures on different tissue types. a-c, Snapshots of printed bioadhesives under single focal heating on porcine stomach (**a**), brain (**b**), and liver (**c**) tissue. Statistical data is given in Fig. 2e in main text. Scale bar, 5 mm.

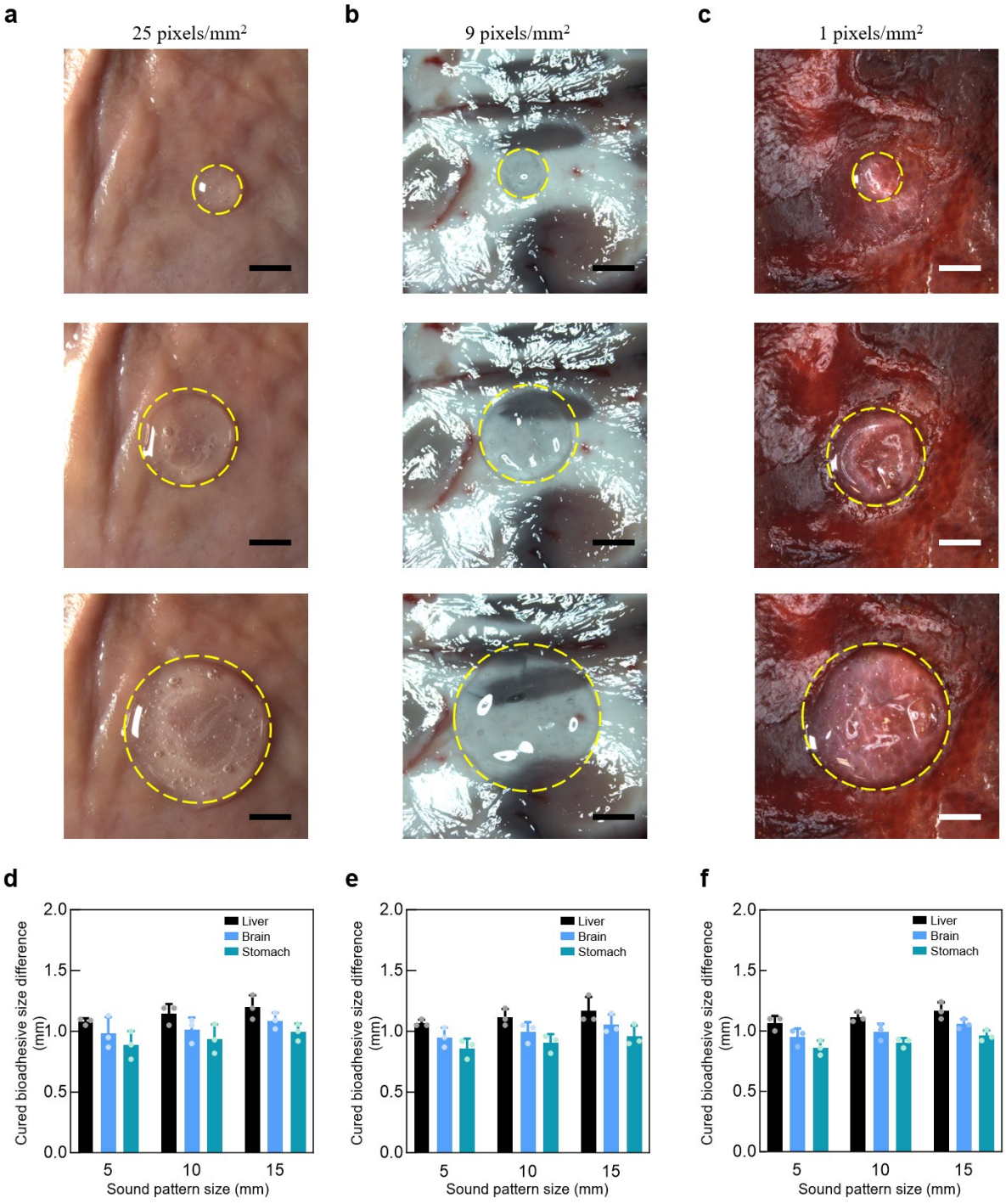

Extended Data Fig. 23 | Characterization of the printing accuracy with varying pixel densities and pattern sizes on different tissue surfaces. a-c, Snapshots of the printed bioadhesives in circular size of 5 mm, 10 mm, and 15 mm diameter heated with the pixel density of 25 pixel/mm^2 (**a**), 9 pixel/mm^2 (**b**), and 1 pixel/mm^2 (**c**) at porcine stomach (**a**), brain (**b**), and liver tissues (**c**). **d-f**, The size difference between printed bioadhesive pattern and the delivered sound pattern with varying pixel density of 25 pixel/mm^2 (**d**), 9 pixel/mm^2 (**e**), and 1 pixel/mm^2 (**f**). Scale bar, 5 mm.

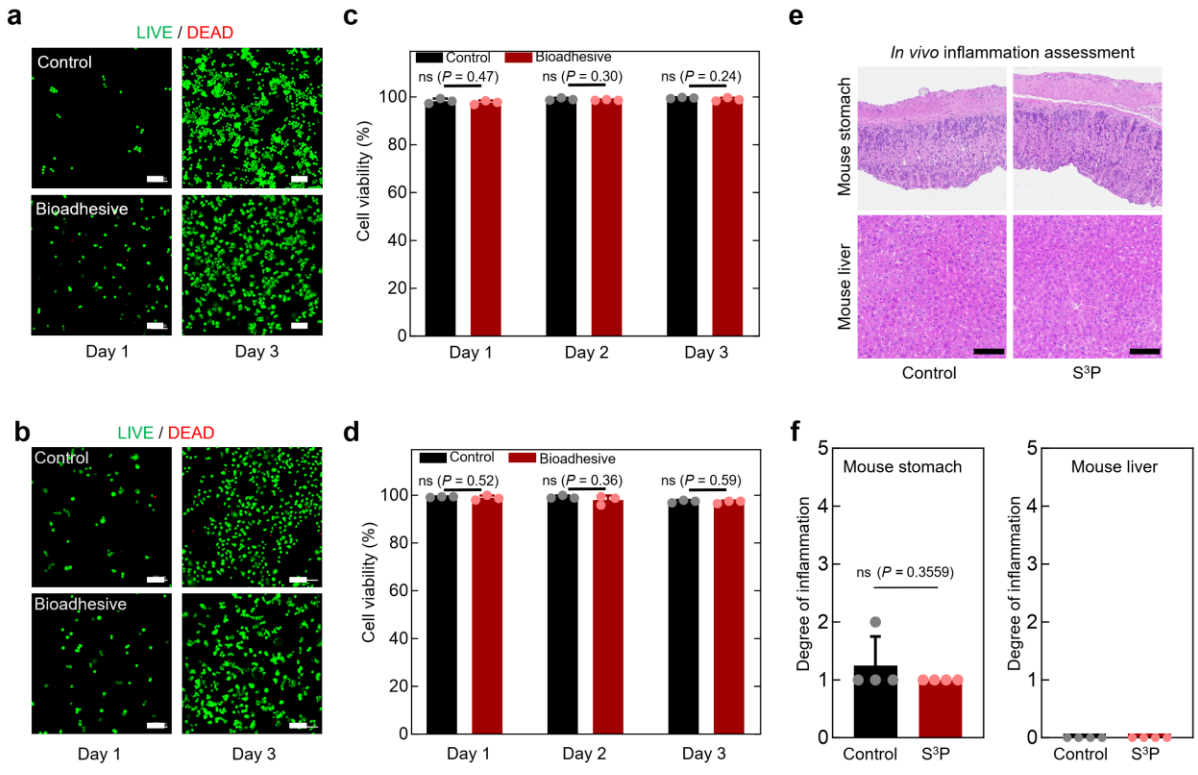

Extended Data Fig. 24 | Cytocompatibility evaluation of S^{3}P. a, Representative LIVE/DEAD assay images of SNU-1 cells treated with control (RPMI 1640) or bioadhesive on different culture days. Live cells (green, calcium-AM) and dead cells (red, PI) are shown. RPMI: Roswell Park Memorial Institute 1640 medium. Scale bar, 200 μm. **b**, Representative LIVE/DEAD assay images of AGS cells treated with control (F-12K) or bioadhesive solution on different culture days. Live cells (green, calcium-AM) and dead cells (red, PI) are shown. F-12K: Ham's F-12K (Kaighn's) medium. Scale bar: 200 μm. **c-d,** Comparison of cell viability after the different culture days application of control or bioadhesive in SNU-1 cells (**c**) and AGS cells (**d**). Values in (**c**) and (**d**) are represented as mean ± s.d. (n=3). Statistical analysis was performed using a two-sided Student's *t*-test; ns, not significant. **e-f**, Representative H&E staining of the mouse stomach three days after S^{3}P compared to untreated tissue (**e**). Four independent experiments were conducted with similar results (**f**). Degree of inflammation: 0 indicates no inflammation; 1, very mild inflammation; 2, mild inflammation; 3, moderate inflammation; 4, severe inflammation; and 5, very severe inflammation. Statistical analysis was performed using a two-sided Student's *t*-test; ns, not significant. Scale bar, 100 μm.

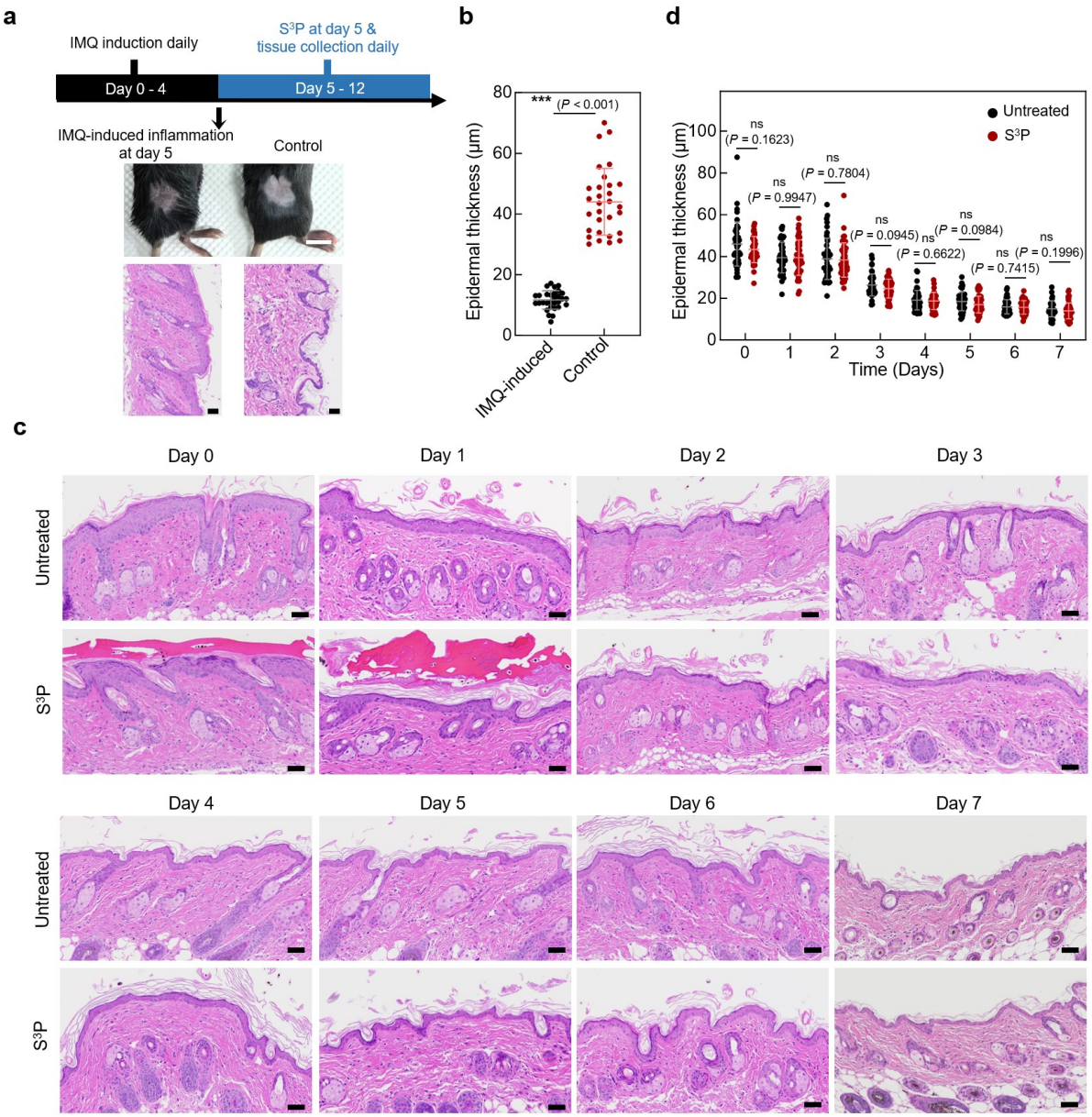

Extended Data Fig. 25 | *In vivo* bioeffects assessment of sonothermal heating during S³P on the IMQ-induced inflammation process in mouse model. a, Schematic illustration of the IMQ-induced inflammation mouse model. Middle row, a photograph of mice showing skin inflammation after IMQ treatment on dorsal skin, compared to blank control. Scale bar, 1 cm. Bottom row, representative H&E staining of dorsal skins from IMQ-treated and control (untreated) mice. Two independent experiments were conducted with similar results. Scale bar, 50 μm. IMQ, imiquimod. **b**, Quantification of epidermis thickness of dorsal skins of mice, n = 2 mice in each group. Data are represented as mean ± s.d. Statistical analysis was performed using a two-tailed Welch's t-test; ***P ≤ 0.001. **c**, Representative H&E staining of the inflamed dorsal skin sections from mice with or without S³P at days 0-7. Three independent experiments were conducted with similar results. Scale bar, 50 μm. **d**, quantification of epidermis thickness of inflamed dorsal skins of mice from c. n = 3 mice in each group. Data are represented as mean ± s.d. Statistical analyses were performed using a two-tailed Welch's t-test for day 0, a two-tailed Student's t-test for the other days; ns, not significant.

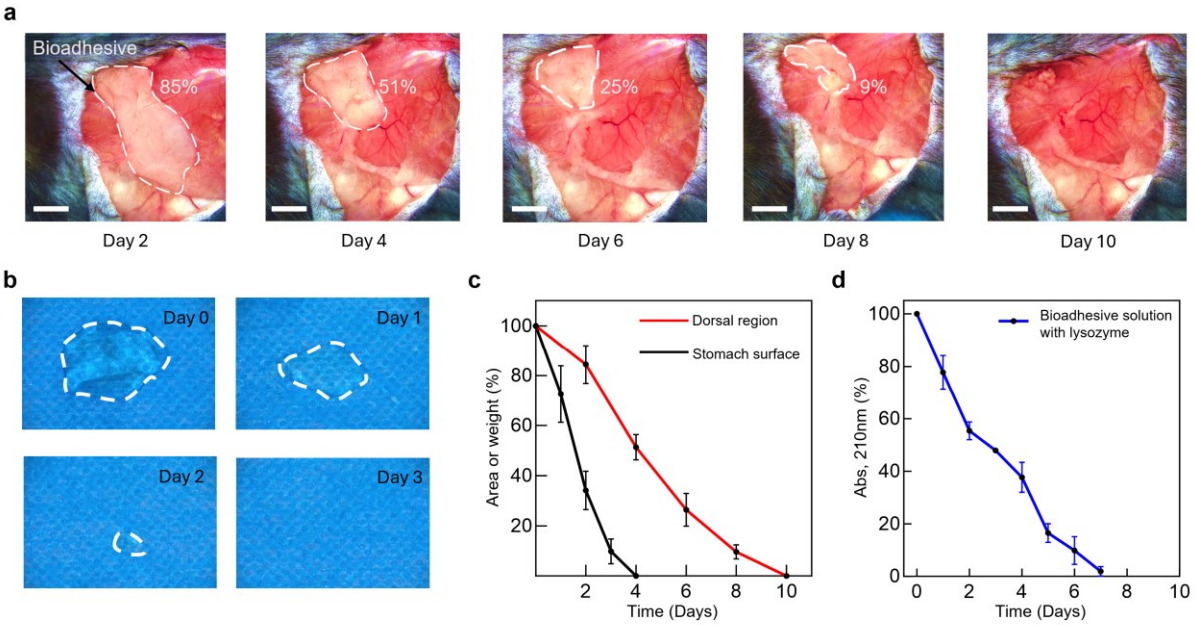

Extended Data Fig. 26 | The degradation process of cured bioadhesive *in vivo* and *in vitro*. **a**, Photos taken during the degradation process of the printed bioadhesive on mouse left dorsal muscle tissue *in vivo*. The bioadhesive was fully degraded four days after printing. Scale bar, 5 mm. **b,** Photos taken during the degradation process of thermal cured bioadhesive immersed in PBS solution at room temperature *in vitro*. The bioadhesive was fully degraded three days after curing. Scale bar, 3 mm. **c**, *In vivo* bioadhesive degradation measured by area (on mouse left dorsal region (red curve) and on stomach surface (black curve) as a function of time. **d**, *In vitro* bioadhesive solution degradation measured by ultraviolet spectrophotometer in PBS solution with lysozyme as a function of time.

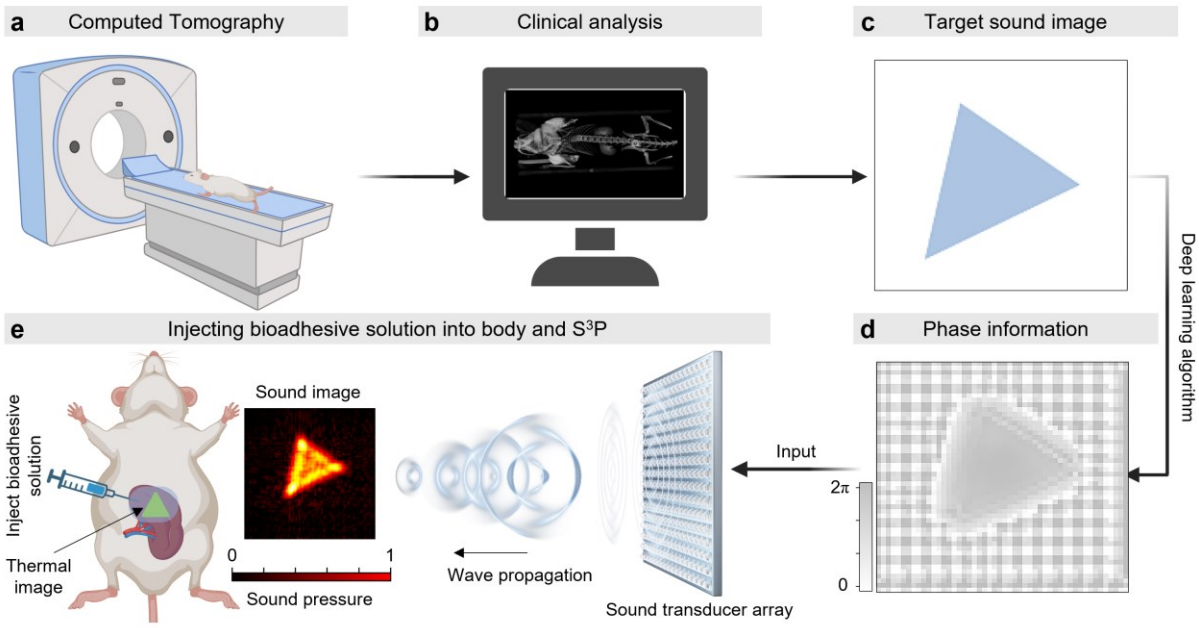

Extended Data Fig. 27 | Schematic illustration of applying S³P for minimally invasive bioadhesive delivery *in vivo*. a, Use micro-CT or ultrasonography to examine the deep tissue. **b**, Determine the geometry and deployment position for the bioadhesive delivery through clinical analysis. **c**, Design a corresponding sound image. **d**, Utilize ultrasound beamforming algorithm to estimate the necessary phase information to control the ultrasonic transducer array. **e**, Inject bioadhesive solution near the targeted area within the body. The ultrasonic transducer array then projects the designed sound image onto the tissue surface, where the sonothermal effect induces the on-site curing of the bioadhesive.

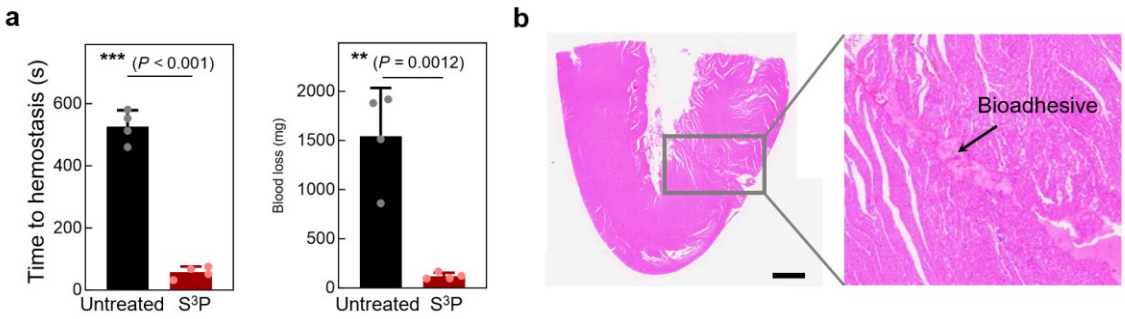

Extended Data Fig. 28 | S^{3}P delivers bioadhesive for rapid cardiac hemostasis to validate the applicability of S^{3}P in wet and dynamic environments even with high pressure. a, Time to hemostasis (left) and blood loss until hemostasis (right) for rat cardiac bleedings untreated and treated with S^{3}P. Data are represented as mean ± s.d. (n = 4). Statistical analysis was performed using a two-sided Student's *t*-test; **P ⩽ 0.01; ***P ⩽ 0.001. **b**, H&E staining of injured heart after hemostatic sealing after S^{3}P immediately. Scale bar, 1 mm.

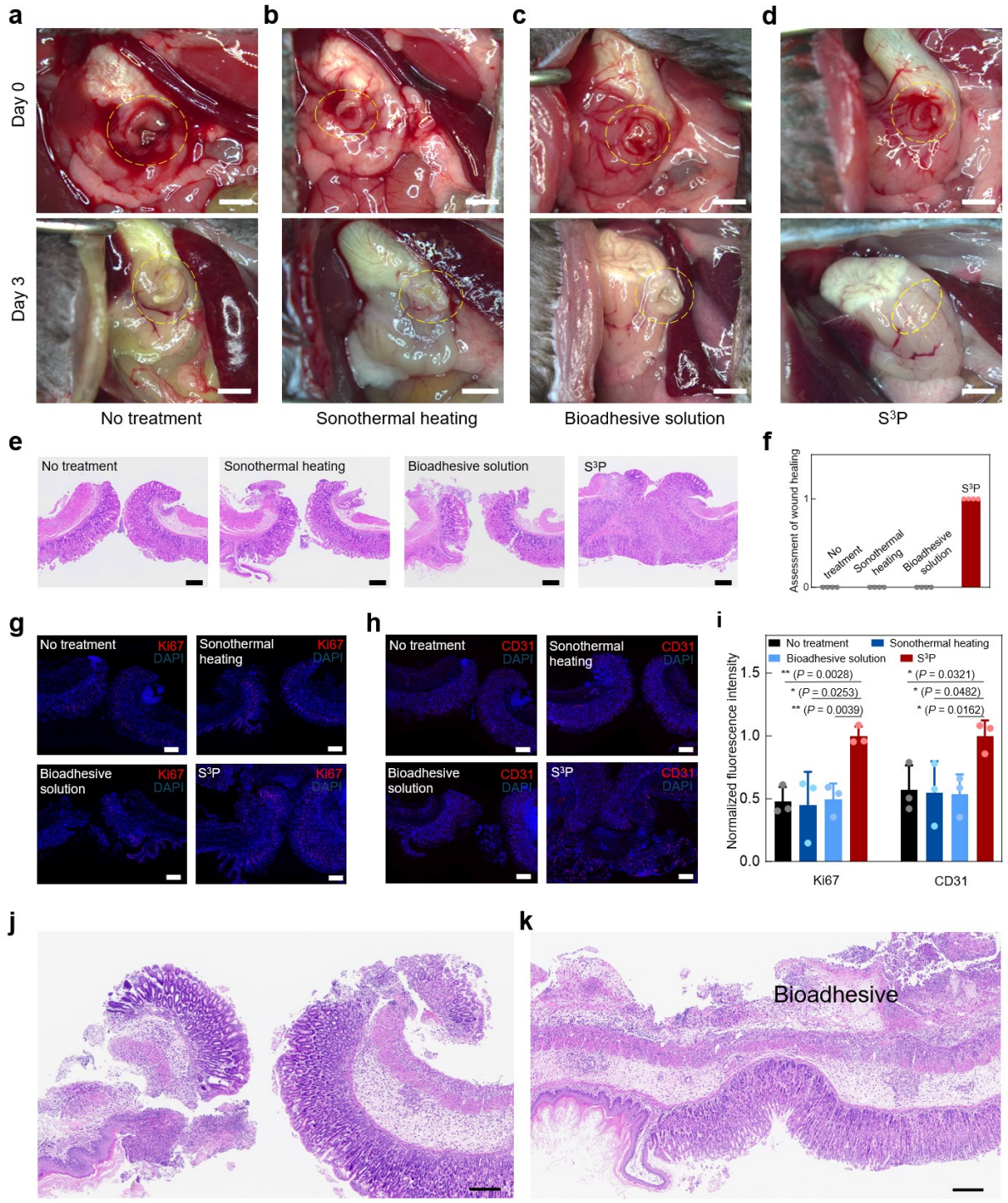

Extended Data Fig. 29 | Wound healing status 3 days after treatment to the mouse gastric perforation. a-i, System control experiments: **a-d,** Representative photographs of the created gastric perforations (top panel) and the stomachs in the four groups, a total of four independent biological replicates were performed for each group (**a**, no treatment, **b**, sonothermal heating alone, **c**, bioadhesive solution alone, **d**, S^3P) 3 days after treatment (bottom panel). Black and red dotted areas indicate the wound site on day 0 and day 3, respectively. Scale bar, 3 mm. **e**, Representative H&E staining of the wound site in the four groups (no treatment, sonothermal heating, bioadhesive solution, S^3P) 3 days after treatment. Scale bar, 200 μm. **f**, Assessment of

wound healing of different groups: 0 indicates not healed; 1 indicates healed. **g-h**, Representative immunofluorescence micrographs of the wound site in the four groups 3 days after treatment. Blue fluorescence corresponds to cell nuclei stained with DAPI; red fluorescence corresponds to the expression of Ki67 (**g**) and CD31 (**h**). Scale bar, 200 μm. **i**, Normalized fluorescence intensity from the immunofluorescence images for Ki67 and CD31 in the four groups 3 days after treatment. Data are represented as mean ± s.d. (n = 3). Statistical analysis was performed using a two-sided Student's *t*-test; *P < 0.05; **P ⩽ 0.01. **j-k**: Treatment control experiments. Representative H&E staining of the wound site in surgical suture treatment group (**j**) and S^3P treatment group (**k**). Scale bar, 200 μm.

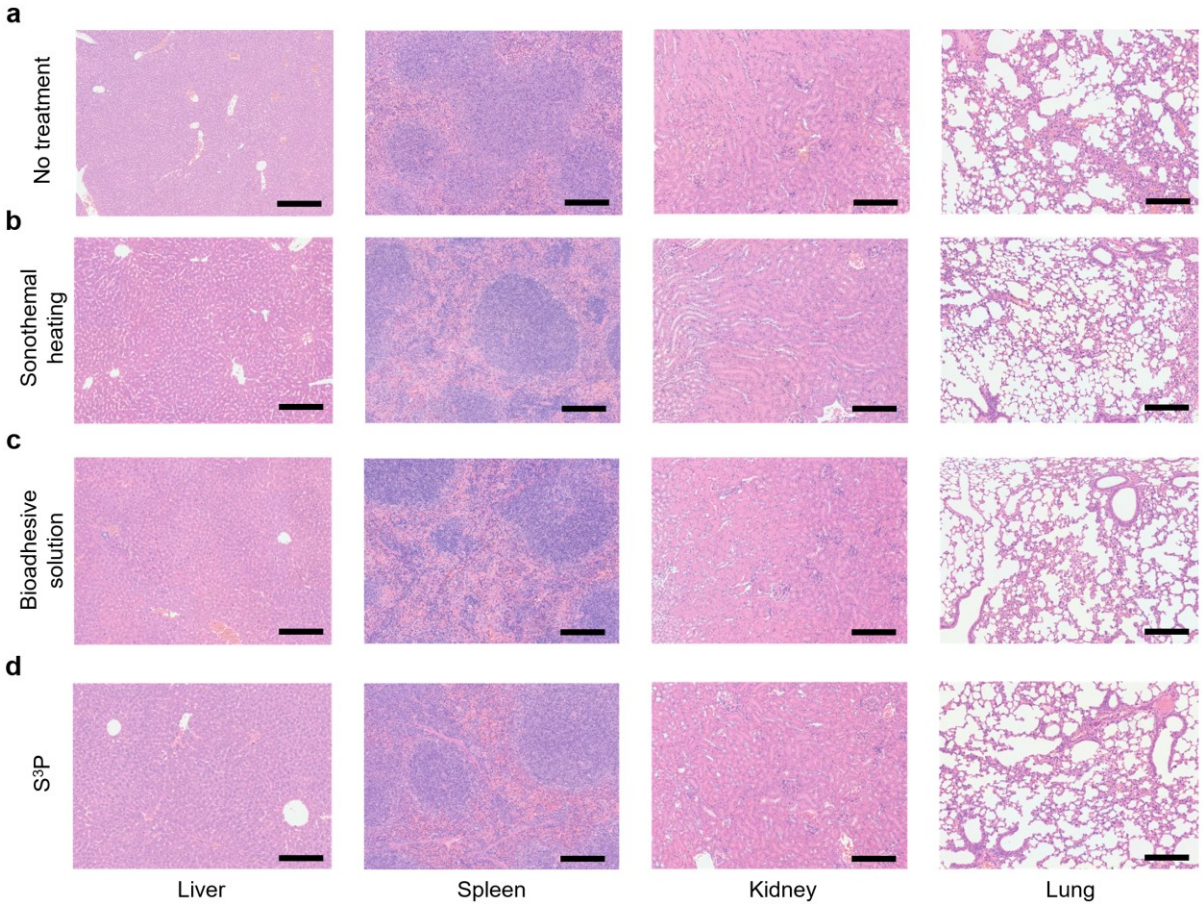

Extended Data Fig. 30 | Representative histological analysis of other organs in mouse gastric perforation repair by S^3P for side effect evaluation. Hematoxylin and eosin (H&E) staining of various visceral organs harvested from the mice in the four groups (**a**, no treatment, **b**, sonothermal heating alone, **c**, bioadhesive solution alone, **d**, S^3P) 3 days after treatment. Three independent experiments were conducted with similar results. Scale bar, 200 μm.

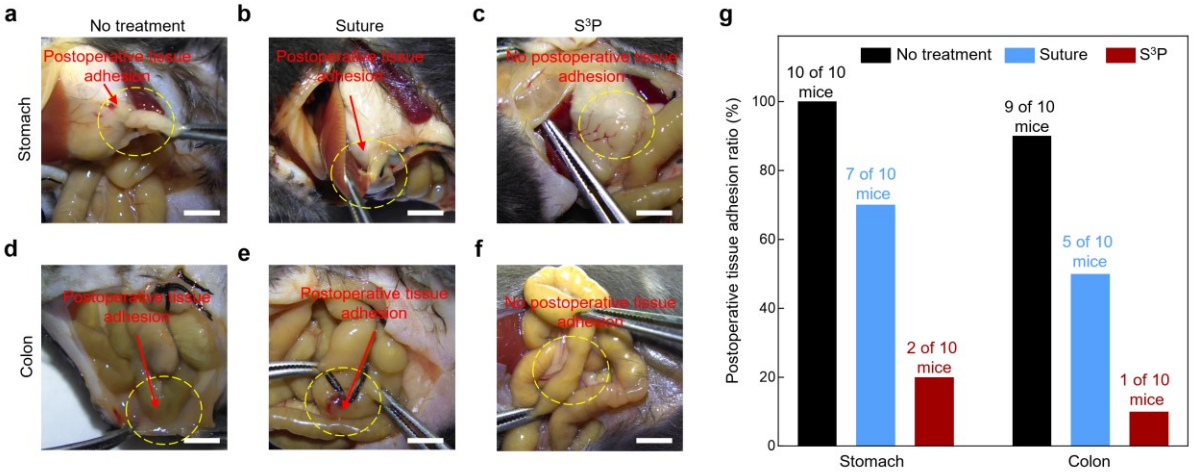

Extended Data Fig. 31 | Characterization of long-term tissue interaction of the delivered bioadhesives by S^{3}P. a-f, Snapshots of mouse stomach (top) and colon (bottom) defects repaired by no treatment (**a** and **d**), suture (**b** and **e**), and S^{3}P (**c** and **f**) after 72 hours. Yellow dotted areas indicate the wound site. Scale bar, 3 mm. **g,** Proportion of post-surgical tissue adhesion formation for mouse stomach and colon defects without treatment (control), treated by suture, and S^{3}P after 72 hours.

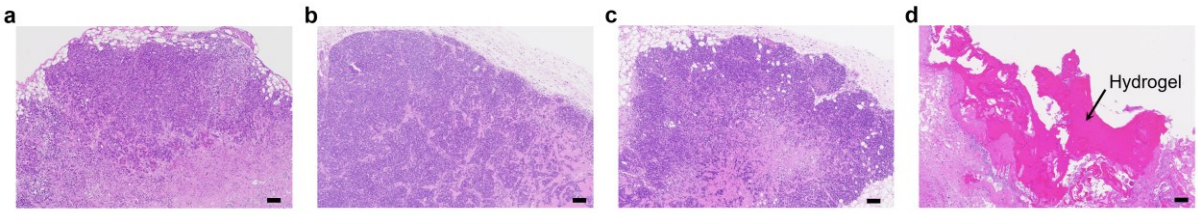

Extended Data Fig. 32 | Pathological analysis of using S^3P for drug delivery to tumor. a-d, Representative H&E staining of the untreated group (**a**), I.P. group (**b**), I.V. group **(c)** and S^3P group **(d)**. Scale bar, 100 μm. Seven independent experiments were conducted with similar results.

Extended Data Table I | Summary of different sound printable materials and their potential biological damage during curing process

Example	Sound pressure	Sound frequence	Curing agent	Induced temperature	Curing initiation method	Curing process	Curing time	Potential biological damage
Nat Commun 13, 1800, 2022	3 MPa	2.15 MHz	/	5000-6000 ℃	Ultrasound induces cavitation in liquid, generating high local temperature.	Radicals react with TMDSO, forming new radicals that initiate chain growth and extend polymer chains through cross-linking polymerization.	1.5 seconds	Thermal damage Radical damage
Nat Commun 15, 6691,2024	2 MPa	1.86 MHz 2.24 MHz 2.28 MHz	/	5000-6000 ℃	Ultrasound induces cavitation in liquid, generating high local temperature.	Radicals react with TMDSO, forming new radicals that initiate chain growth and extend polymer chains through cross-linking polymerization.	~10 seconds	Thermal damage Radical damage
Science 382,1148-1155, 2023	35-55 MPa	2.05 MHz 3.41 MHz 6.68 MHz	APS	60-80 ℃	Ultrasound generates high temperatures at focal point, causing APS to produce free radicals.	Radicals cause the monomers in the solution to polymerize, thereby achieving curing.	2 seconds	Thermal damage Material toxicity Radical damage
S^3P	2.7 MPa	2.32 MHz	PAA-NHS	37-42 ℃	Ultrasound induces temperature and streaming, boosting PAA-NHS and HBCS collisions.	The intensified collisions between PAA-NHS and HBCS lead to the formation of amide bonds, thereby achieving cross-linking.	40 seconds under sonothermal heating at 42 ℃	NONE observed

References

1 Lee, M. H., Lew, H. M., Youn, S., Kim, T. & Hwang, J. Y. Deep Learning-Based Framework for Fast and Accurate Acoustic Hologram Generation. *IEEE Trans Ultrason Ferroelectr Freq Control* **69**, 3353-3366 (2022).

2 Ronneberger, O., Fischer, P. & Brox, T. in *Medical image computing and computer-assisted intervention–MICCAI 2015: 18th international conference, Munich, Germany, October 5-9, 2015, proceedings, part III 18.* 234-241 (Springer).

3 Marzo, A. & Drinkwater, B. W. Holographic acoustic tweezers. *Proc Natl Acad Sci U S A* **116**, 84-89 (2019).

4 Liu, S. & Li, Y.-F. Precision 3-D motion tracking for binocular microscopic vision system. *IEEE transactions on industrial electronics* **66**, 9339-9349 (2019).

5 Ma, Z. *et al.* Bioinspired Printable Tough Adhesives with In Situ Benignly Triggered Mechanical Enhancements. *Advanced Functional Materials* **34**, 2403290 (2024).

6 Wu, S. J. *et al.* A 3D printable tissue adhesive. *Nat Commun* **15**, 1215 (2024).

7 Mohapatra, H., Kleiman, M. & Esser-Kahn, A. P. Mechanically controlled radical polymerization initiated by ultrasound. *Nature Chemistry* **9**, 135-139 (2017).

8 Narayanan, B. *et al.* Cavitation and radicals drive the sonochemical synthesis of functional polymer spheres. *Applied Physics Letters* **109** (2016).

9 Orszulik, S. T. The use of ultrasound and a thermolabile radical initiator in the polymerization of acrylate monomers. *Polymer* **34**, 1320-1321 (1993).

10 Rokita, B., Rosiak, J. M. & Ulanski, P. Ultrasound-induced cross-linking and formation of macroscopic covalent hydrogels in aqueous polymer and monomer solutions. *Macromolecules* **42**, 3269-3274 (2009).

11 Gao, Z. *et al.* Sono-Polymerization of Poly(ethylene glycol)-Based Nanoparticles for Targeted Drug Delivery. *ACS Macro Lett* **8**, 1285-1290 (2019).

12 Sadhal, S. S. Acoustofluidics 13: Analysis of acoustic streaming by perturbation methods. *Lab Chip* **12**, 2292-2300 (2012).

13 Joergensen, J. H. & Bruus, H. Theory of pressure acoustics with thermoviscous boundary layers and streaming in elastic cavities. *J Acoust Soc Am* **149**, 3599 (2021).

14 Łukaszewicz, G. & Kalita, P. Navier – stokes equations. *Advances in Mechanics and Mathematics* **34** (2016).

15 Bach, J. S. & Bruus, H. Bulk-driven acoustic streaming at resonance in closed microcavities. *Phys Rev E* **100**, 023104 (2019).

16 Melde, K., Mark, A. G., Qiu, T. & Fischer, P. Holograms for acoustics. *Nature* **537**, 518-522 (2016).

17 Wu, J. *et al.* An off-the-shelf bioadhesive patch for sutureless repair of gastrointestinal defects. *Sci Transl Med* **14**, eabh2857 (2022).

Supplementary Text

Supplementary Note 1. Sonothermal effect on tissue surface.

S^3P leverages the sonothermal effect at the tissue-bioadhesive boundary to selectively cure the thermoresponsive bioadhesive solutions. As ultrasonic waves propagate through the tissue, their mechanical energy is absorbed by the tissue molecules, causing them to vibrate. This molecular vibration converts mechanical energy into thermal energy through friction, resulting in localized heating. Biological tissues, such as muscle, have significantly higher attenuation coefficients than water (e.g., muscle tissue has an attenuation coefficient of about 1.2 dB/cm/MHz compared to water's much lower coefficient of approximately 0.002 dB/cm/MHz). This higher attenuation means that tissues absorb more acoustic energy, leading to more substantial heat generation. The degree of heating is influenced by several factors, including the intensity and frequency of the ultrasound waves and the specific absorption characteristics of the tissue. As the absorbed ultrasonic energy is converted into heat, it increases the local temperature of the tissue through heat accumulation, which can be precisely controlled by adjusting sound parameters, ensuring effective and targeted curing of bioadhesive solution while avoiding the risk of heating other tissues.

Without considering the thermal transfer, the temperature of biological tissue exposure to ultrasound (plane waves) can be predicted by the differential equation of

$$\partial T / \partial t = 2\alpha I / \rho C_p \tag{2}$$

where T is temperature in unit of ℃, t is time in unit of second, α is absorption coefficient of tissue, I is the intensity of ultrasound, ρ is the of tissue, C_p is the specific heat of tissue (~4.2 J/g℃). Equation (2) reveals a linearly proportional relationship between temperature elevation to sound intensity under neglecting thermal transfer effect, which is confirmed by the early stage of thermal heating experiments in Extended Data Fig. 7.

In existing sound printing techniques, sound energy is directly focused to the printing materials. In contrast, S^3P selectively deposits patterned sound onto target deep-tissue surface to induce spontaneous sonothermal heating on site. The reasons for why we deposit sound energy onto target tissue surface instead of to bioadhesive solution are discussed as follows:

1. More efficient heat generation. Sonothermal effect means the temperature increase due to material acoustic attenuation. This phenomenon is inevitable in any acoustic exposure regardless of the printing materials (the temperature elevation is proportional to the medium attenuation coefficient). Given the fact that biological tissues, such as muscle, have significantly higher attenuation coefficients than water and hydrogel solution, depositing sound energy onto tissue surface is more efficient in heat generation. By this way, we can cure the bioadhesive at a given temperature in relative lower sound pressure input, thus minimizing the potential hazardous impacts of high sound exposure to tissue.

2. More stable curing temperature. Delivering bioadhesive into deep tissue is inherently challenging due to the wet and dynamic nature of tissue surfaces. If we direct sound energy to bioadhesive solution, the acoustic streaming effect and the tissue vibration will lead to unstable curing temperature. In contrast, leveraging the oval-shaped focal profile, depositing sound energy onto tissue surface makes the heat source be irrelevant to acoustic streaming, meanwhile enables S^3P to be able to tolerate moderate tissue surface vibration, resulting in more stable *in vivo* heat generation and curing temperature for bioadhesive curing (Supplementary Note 8).

3. More rapid heat diffusion. Acoustic streaming effect is inevitable in sound printing process. In classical through tissue sound printing, the acoustic streaming is an adverse effect to the sound printing process. By utilizing the boundary effect of tissue surface through depositing sound energy onto tissue surfaces, we can reshape the acoustic streaming to be local circulation (Supplementary Note 4), which facilitates rapid heat diffusion, promotes uniform temperature distribution, and accelerates the sound curing rate (Supplementary Note 5).

4. Better biosafety. On one hand, the high acoustic attenuation coefficient of tissue compared to bioadhesive solution enables the same temperature increase with lower acoustic pressure input; on the other hand, the thereby induced local circulation leads to the more evenly distributed temperature, avoiding the overheating to local tissue due to heat accumulation particularly when it comes to patterned bioadhesive delivery. Therefore, depositing sound energy onto tissue surface ensures better biosafety for printing patterned bioadhesives on tissue surfaces in a single step (Supplementary Note 7).

5. Break the interfacial water barrier on wet tissue surface. Delivering bioadhesives onto wet tissue surfaces is inherent challenge, since the interfacial water barrier on tissue surface stops the effective formation of bioadhesion to tissue surfaces. Traditionally solved from the bioadhesive design side, by depositing sound energy onto tissue surfaces, the acoustic streaming will induce a local circulation under the boundary effect of the tissue surface can effectively break the interfacial water barrier, thus enabling effective delivery of bioadhesion to tissue surfaces (Supplementary Note 3).

Note that, depositing sound energy onto tissue surface also results in new challenges to printing resolution, since the local circulation facilitates the heat diffusion both spatially and temporally. On one hand, the spatially facilitated heat diffusion leads to enlarged reactivity zone (beyond the focal zone) for curing; on the other hand, the temporally facilitated heat diffusion requires rather fast curing rate of material to realize finer printing resolution (Supplementary Note 6).

Supplementary Note 2. Sound printable bioadhesive materials.

1. The concept of sound printable bioadhesive materials to bioadhesive chemistry. Successful implementation of S^3P necessitates the sound printable bioadhesive materials, which are conceptually differentiable from the bioadhesive materials, printable bioadhesive materials[5-6], sound printable materials, and the sound-driven polymerization materials[7-11]. Sound printable bioadhesive materials should fulfill the following essential requirements on

- **Sound printability**, i.e., the curing temperature is higher than that of the body;
- **Sound-driven adhesion formation**, i.e., the effective adhesion formation to tissues is actively triggered by the exposure to sound;
- **Clinical functionality**, e.g., adequate adhesion performance, mechanical strength, biocompatibility, and biodegradability for clinical tasks, such as tissue healing; and
- **Printing biosafety**, i.e., the curing and adhesion formation temperature should be slightly higher than that of the body,

so that the materials can be applied for the minimally invasive *in vivo* and *in situ* delivery of bioadhesives onto deep tissue surfaces through volumetric sound printing.

The concept of sound printable bioadhesive materials is not reported from literature yet. Existing bioadhesive materials, printable bioadhesive materials, commercially available thermosensitive hydrogels, or the materials reported from the latest sound printing techniques, or the impressive sono-ink reported by *Kuang et al.* cannot comprehensively fulfill the above-mentioned requirements as functional sound-printable bioadhesive materials to achieve a well controllable and biosafe on-tissue sound printing approach for the minimally invasive *in vivo* and *in situ* delivery of bioadhesives on deep tissue surfaces.

2. The printing characteristics of the PAA-NHS/HBCS formulation. The formulation of PAA-NHS and HBCS as a bioadhesive material (Extended Data Fig. 12), particularly as a sound printable bioadhesive material, has not been reported or explored yet. To our best knowledge, this is the first functional sound printable bioadhesive formulation satisfying all the requirements we mentioned in last paragraph so far. Of particular significance, our investigation on S^3P provides essential insights to understand the printing characteristics of the PAA-NHS/HBCS formulation as the first sound printable bioadhesive material, which lays out a benchmark for future endeavors in this regard.

- **The concentration matters.** The concentration of PAA-NHS and HBCS in bioadhesive solution determines the adhesion strength, the mechanical properties, the biodegradability, the curing temperature, and the curing time (Extended Data Fig. 11). The adhesion strength, the mechanical properties, and the biodegradability determine the functionality, while the curing temperature and curing time determines the biosafety and printability.

- **The tradeoff between stronger adhesion/mechanical strength and printability**. If we want to improve mechanical properties and adhesion strength, we need to increase the concentration of PAA-NHS and HBCS. However, increasing the concentration of PAA-NHS and HBCS will in turn lower the curing temperature. Once the curing temperature getting lower (or much lower) than that of the body, the material will lose printability (because body temperature can already cure the bioadhesive solution).

- **The tradeoff between faster curing rate/printing resolution and printability**. We prefer faster curing rate for a printing technique for the sake of efficiency and finer printing resolution (Supplementary Note 6). By increasing the concentration of PAA-NHS and HBCS, we can fasten the curing rate. However, the cost is the decrease of the curing temperature, with determines the printability of the bioadhesive material.

Facing the above-mentioned tradeoffs, with the commonly used materials of PAA-NHS and HBCS in bioadhesive's chemistry, we have meticulously formulated the PAA-NHS/HBCS system (leveraging the printing behaviors of on-tissue sound printing Supplementary Note 3) to first fulfill the printability, adhesion controllability, functionality, and biosafety requirements, making the formulation a functional sound printable bioadhesive material for minimally invasive *in vivo* and *in situ* delivery of applicable bioadhesives onto deep tissue surfaces. Through our experiments, our sound printable bioadhesive material features 3 mins curing time at 42 °C with hotplate heating (S^3P facilitates the curing time from 3 mins to 40 seconds), adequate adhesion strength for tissue healing (e.g., gastric perforation repair, S^3P enhances the adhesion strength from ~33 J/m^2 to ~70 J/m^2), and applicable mechanical strength in hash environments with high pressure and blood bleeding (e.g., cardiac hemostasis, S^3P enhances the mechanical strength from ~14.5 kPa to ~19.5 kPa, Extended Data 15d).

We have to mention that the resulting curing time of our bioadhesive material design under sonothermal heating (40 seconds at 42 °C) leads to the fact that the printing resolution of S^3P is spatially determined by the reactivity zone, since the heat diffusion process facilitated by local circulation reaches thermal balance rapidly (Supplementary Note 6).

These insights help our fundamental understanding to the PAA-NHS/HBCS formulation as a functional sound printable bioadhesive material. For clinical tasks requiring stronger adhesion/mechanical strength, faster curing time, enhanced biocompatibility, and low-temperature curability, other types of sound-printable bioadhesive material should be developed, but they should first satisfy the necessary requirements in order to by deplorable by S^3P. Our fundamental understanding obtained from S^3P to the on-tissue sound printing behavior and the sound printable adhesive materials provide valuable insights for future efforts to develop other types of sound printing bioadhesive materials from bioadhesive's chemistry.

Supplementary Note 3. Adhesion and mechanical strength.

Bioadhesives with varying adhesion performance and mechanical properties are essential for different clinical applications due to the diverse requirements of each medical scenario. An ideal bioadhesive requires strong tissue adhesion and proper mechanical strength, which should be designed to match or exceed the strength of the target tissue they are intended to repair. Mismatching between the mechanical strength of a bioadhesive and that of the tissue may raise up severe issues, such as the inflammation, tissue damage, stress concentration and even failure. The adhesion and the bioadhesives delivered by S^3P features an adhesion strength of ~70 J/m^2 (on rat colon, Fig. 3d), a Young's modulus of ~19.5 kPa (Extended Data Fig. 15), adequate long-term stability (Extended Data Fig. 16) and biodegradability (Extended Data Fig. 26), which has been validated to be applicable to soft tissue repair clinical tasks, such as would closure, hemostasis, and tissue sealants (e.g., gastric perforation repair).

From the material design side, as discussed in Supplementary Note 2, the adhesion and mechanical strength of the bioadhesive can be modulate by the concentration of PAA-NHS and HBCS of the bioadhesive solution (Extended Data Fig. 11). As the concentration of PAA-NHS and HBCS increases, more amido bonds can be formed (Extended Data Fig. 13b), which enhances both the adhesion and mechanical strength. However, increasing the concentration would decrease the curing temperature, probably leading to the losing of printability (once curing temperature is lower than that of the body). Therefore, there is an upper bond to increase the adhesion and mechanical strength by increasing the concentration of bioadhesive solution. We set the curing temperature to be 37 °C (the body temperature), which is the lowest feasible temperature to ensure printability, while the corresponding concentration of PAA-NHS and HBCS in the bioadhesive solution is the highest we can get without compromising printability. Under hotplate curing (42 °C for 3 mins), the adhesion strength of cured bioadhesive is ~33 J/m^2 (on rat colon, Fig. 3d) and the mechanical strength is ~14.5 kPa (Extended Data Fig. 15d).

In S^3P, the delivered adhesion and mechanical strength is substantially enhanced by leveraging the on-tissue sound printing behaviors. By depositing patterned sound onto target tissue surface, the acoustic streaming effect will induce a local circulation inside the bioadhesive solution on the tissue surface, which would facilitate more efficient heat transfer from the heated tissue surface to the bioadhesive solution and the heat diffusion within the bioadhesive solution. Meanwhile, it will also enhance the mixing of PAA-NHS and HBCS, which, in turn, increases the frequency of reactive species collisions. More significantly and more substantially, the local circulation breaks the interfacial water barrier on wet tissue surfaces (Extended Data Fig. 19) which stops the effective formation of adhesion (takes the form of amido bonds in S^3P). These reasons promote the formation of more amido bonds to target tissue surface (we have visualized and characterized the local circulation, the facilitated heat diffusion, and the mixing effect. See more in Supplementary Note 5). As a result, the adhesion strength delivered by S^3P reaches as high as ~70 J/m^2 (on rat colon, in contrast to ~33 J/m^2 under hotplate curing, Fig. 3d).

In regard to the mechanical strength of delivered bioadhesives, we see similar results due to the same reasons as discussed above, where the sound induced local circulation in bioadhesive solution will also promote stronger mechanical strength. Through analyzing the cured bioadhesives by hotplate cuing (42 °C for 3 mins) and sonothermal curing (42 °C for 40 seconds) respectively in molecular level, we see more amido bonds can be formed in S^3P (Extended Data Fig. 21a), improving the mechanical strength from ~14.5 kPa to ~19.5 kPa in terms of Young's modulus, validating that S^3P also helps to improve the mechanical strength (Note that the curing percentage of the bioadhesive solution is determined by rheological mechanics analysis instead of the number of the amido bonds).

For bioadhesives cured at different temperatures, the adhesion and mechanical strength show no marked difference (Extended Data Fig. 15), which can be attributed to the fact that the local circulation dominantly ensures the complete curing of the bioadhesive solution already.

S^3P utilizes a transducer array and a deep learning-based algorithm to selectively deposit patterned sound onto target tissue surface in order to realize the delivery of bioadhesion and bioadhesive in a single step. The sound image quality in terms of sound patterning resolution (i.e., the pixel density or the number of pixels in a given pattern) would substantially impact the effectiveness of the delivered bioadhesives. On one hand, there is a physical limit for a transducer array to generate a single focal point[16] (our transducer array can generate a single focal point with lateral focal size of ~1 mm under -6 dB attenuation criteria, Fig. 2d, Extended Data Fig. 2); on the other hand, the heat diffusion due to the sound induced local circulation covers enlarged heating zone (hotspot) under single focal point (Extended Data Fig. 18e). Therefore, sound patterning resolution is an important factor of S^3P. The adhesion strength of ~70 J/m^2 (on rat colon) and the mechanical strength of ~19.5 kPa are achieved under sound pattern resolution of 50 × 50 pixels covering an area of 50 × 50 mm^2.

The size of the effective heating zone under a single focal point varies depending on the input sound pressure and the heat dissipation coefficient of target tissue (Extended Data Fig. 5), ranging from ~1.7 mm to 2.2 mm (Extended Data Fig. 8d). If the sound patterning resolution is low (e.g., 25 × 25 pixels covering an area of 50 × 50 mm^2) so that the effective heating zone by each pixel in the sound pattern cannot overlap each other (e.g., left column Fig. 2a), part of the bioadhesives upon the target tissue will not be fully cured (for 40 seconds under 42 °C), and bioadhesion cannot be effectively formed (Extended Data Fig. 17). If the sound patterning resolution is high enough (e.g., 50 × 50 pixels covering an area of 50 × 50 mm^2) so that the effective heating zone overlaps each other and covers the entire pattern, given the analysis in last paragraph, further increasing the pixel number in a given pattern (e.g., 150 × 150 pixels covering an area of 50 × 50 mm^2) can also slightly enhance the adhesion and adhesive strength to some extent (Extended Data Fig. 17), because more pixels in a given pattern will induce more dense acoustic streaming, thus leading to stronger heat diffusion and mixing effect.

Supplementary Note 4. Local circulation on tissue surface.

Acoustic streaming is the phenomenon that takes place when a steady flow field is generated by the absorption of an oscillatory field[12]. To describe the absorption of the sound field, thermoviscous acoustics can be applied. Following the conventions from literature[13,14], the governing equations of the thermoviscous acoustics is based on mass conservation, momentum conservation, and energy conservation, given as

$$i\omega\rho_t + \nabla\cdot(\rho_0\mathbf{u}_t) = 0 \tag{3a}$$

$$i\omega\rho_0\mathbf{u}_t = \nabla\cdot\boldsymbol{\sigma} \tag{3b}$$

$$\rho_0 C_p(i\omega T_t + \mathbf{u}_t\cdot\nabla T_0) - \alpha_p T_0(i\omega p_t + \mathbf{u}_t\cdot\nabla p_0) = \nabla\cdot(k\nabla T_t) + Q \tag{3c}$$

where i is the imaginary unit, ω the angular frequency of sound, ρ_t is the first order fluid density that varies with sound propagation, ρ_0 is the static density of the fluid, $\mathbf{u}_t$ is the particle velocity of the fluid, $\boldsymbol{\sigma}$ is a stress tensor applied on the fluid, C_p is the specific heat of the fluid at constant pressure, T_t is the first order temperature that varies with sound propagation, T_0 is static density of the temperature, α_p is thermal expansivity, p_t is first order sound pressure that varies with sound propagation, k is thermal conductivity of the fluid, and Q is an external heat source.

Since the sound field is time-harmonic, complex variable is introduced to simplify the equations. Equation (3a) represents the mass conservation, which means transportation of mass cause change of density. Equation (3b) represents the momentum conservation, which means change of momentum is equal to impulse of the total stress. Equation (3c) represents the energy conservation, which describe the change of temperature due to heat conduction and heat convection. To solve the equations above, we need further two additional constitutive equations

$$\boldsymbol{\sigma} = -p_t\mathbf{I} + \mu(\nabla\mathbf{u}_t + (\nabla\mathbf{u}_t)^T) - (\frac{2}{3}\mu - \mu_B)(\nabla\cdot\mathbf{u}_t)\mathbf{I} \tag{4a}$$

$$\rho_t = \rho_0(\beta_T p_t - \alpha_p T_t) \tag{4b}$$

where $\mathbf{I}$ is an identical matrix in size of 3×3, μ is the dynamic viscosity of the fluid, μ_B is the bulk viscosity of the fluid, and β_T is the compressibility of the fluid at specific temperature.

Equation (4a) describes the stress tensor in the fluid. Equation (4b) describes the density of the fluid is not only related to pressure, but also related to temperature, which is different from linear acoustics. After the sound field is obtained, then the Navier-Stokes equation is required to obtain acoustic streaming:

$$\rho_0(\mathbf{u}_2 \cdot \nabla)\mathbf{u}_2 = \nabla \cdot [-p_2\mathbf{I} + \mathbf{K}] + \mathbf{F} \tag{5}$$

where $\mathbf{u}_2$ is the velocity of the flow, p_2 is the hydraulic pressure due to the flow, $\mathbf{K}$ is the stress tensor due to the viscosity of the fluid, and $\mathbf{F}$ is the external volume force.

In essence, equation (5) is equal to equation (3b), both equations represent momentum conservation, and both the right term of the equations are stress tensors in the fluid. To distinguish from the alternating variable (p_t and $\mathbf{u}_t$), we use p_2 and $\mathbf{u}_2$ to describe the direct variables, which are not time-harmonic, but rather steady.

Similarly, equation (5) can be solved by combining one constitutive equation and a constraint equation:

$$\rho_0 \nabla \cdot \mathbf{u}_2 = 0 \tag{6a}$$

$$\mathbf{K} = \mu(\nabla \mathbf{u}_2 + (\nabla \mathbf{u}_2)^T) \tag{6b}$$

Equation (6a) is the mass conservation with assumption that fluid is incompressible. Equation (6b) is one term in the equation (4a), which the stress tensor due to viscosity of the fluid.

When consider the coupling of the sound field to the flow field, equation (5) and (6a) will be corrected by adding extra terms:

$$\rho_0(\mathbf{u}_2\cdot\nabla)\mathbf{u}_2=\nabla\cdot[-p_2\mathbf{I}+\mathbf{K}]+\mathbf{F}+\nabla\cdot\tau_{\text{aco}} \tag{7a}$$

$$-\rho_0\nabla\cdot\mathbf{u}_2-\nabla\cdot\mathbf{M}_{\text{aco}}=0 \tag{7b}$$

$$\mathbf{M}_{\text{aco}}=\left\langle\rho_t\mathbf{u}_t\right\rangle \tag{7c}$$

$$\tau_{\text{aco}}=-\rho_0\left\langle\mathbf{u}_t,\mathbf{u}_t\right\rangle-L_{\text{aco}}\mathbf{I} \tag{7d}$$

$$L_{\text{aco}}=\frac{1}{4}\beta_T|p_t|^2-\frac{1}{4}\rho_0\|\mathbf{u}_t\|_2^2 \tag{7e}$$

where $\boldsymbol{\tau}_{\text{aco}}$ is the stress tensor due to sound absorption, $\mathbf{M}_{\text{aco}}$ is the time-average mass flux due to the acoustic streaming L_{aco} is a scalar that describe the stress contributed by the sound pressure. Equation (7a) is added an additional stress tensor term due to the sound absorption. Equation (7b) is added an additional mass transfer term due to the nonlinearity of the sound.

However, the result of the flow field not only depends on the Navier-Stokes equation itself or the stress tensor due to the sound field, but also depends on the boundary conditions. The most common boundary condition is “No slip” condition, mathematic form of the boundary condition are simple:

$$\mathbf{u}_2=\mathbf{0} \tag{8}$$

which means the fluid in contact with the solid boundary is totally dragged by the solid. Although the boundary condition form is simple, the location of the boundary condition will still greatly affect the final outcome.

In addition to the boundary condition, there are some other factors that can substantially affect the outcome of the Navier-Stokes equation. For example, sound pressure may affect the results. When the sound pressure is low, the stress due to sound absorption is also small, so the flow speed is small, which means the flow is dominated by viscosity force. In this case, the Navier-Stokes equation degenerate to a linear equation. But when the sound pressure is high, the flow

speed rise, inertial term in the equation will gradually dominate, and the Navier-Stokes equation become a nonlinear equation. This transformation would lead to different results. For example, rotation direction of the flow pattern may reverse, which is observed during the experimentation.

We mathematically solved the streaming equations by finite element method (FEM, in COMSOL Multiphysics 6.1) to calculate the flow patterns upon tissue surface under the exposure of a single focal pressure, as illustrated in Extended Data Fig. 18a, where a local circulation is formed, which agrees well with our experimental characterization (Extended Data Fig. 18b).

The local circulation on tissue surfaces essentially distinguishes S^3P from existing sound printing techniques in terms of printing behaviors. In the following, we summarize the effects of the local circulation in S^3P, as follows:

1. Break the interfacial water barrier on wet tissue surface to form strong adhesion to tissue (Discussed in Supplementary Note 3);

2. Mix the bioadhesive solution to enhance the mechanical strength of the cured bioadhesive (Discussed in Supplementary Note 3);

3. Facilitate heat diffusion and mix the bioadhesive solution to accelerate the curing time (Discussed in Supplementary Note 5);

4. Facilitate heat diffusion to avoid local overheating to tissue in patterned bioadhesive printing (Discussed in Supplementary Note 7);

5. Enlarges the reactivity zone beyond focal zone, leading to challenges to printing resolution (Discussed in Supplementary Note 6).

Supplementary Note 5. Accelerated curing under sonothermal heating.

The printing behavior of S^3P is substantially determined by the heat diffusion process. Since S^3P deposits sound energy onto target tissue surface, the heat transfers from the heated tissue surface into bioadhesive solution. Due to the low-temperature curing and adhesion formation requirements imposed by biosafety concerns, the elevated temperature on tissue surface is only a few degrees higher than that of the bioadhesive solution. The very low temperature gradient inherently determines the low heat diffusion rate from the heated tissue surface into the bioadhesive solution, leading to long curing time. Meanwhile, our sound printable bioadhesive materials faces the tradeoff between curing time and printability (Supplementary Note 2). Increasing the concentration of PAA-NHS/HBCS in bioadhesive solution will decrease the curing time (Extended Data Fig. 11g). However, this also would decrease the curing temperature, probably leading to losing printability (once curing temperature is lower than that of the body). Therefore, there is an upper bond to decrease the curing time through increasing the concentration of bioadhesive solution. Finally, a long curing time makes the bioadhesive vulnerable to body fluid dilution, which would decrease the concentration of the bioadhesive solution, leading to the increase of curing temperature. The diluted bioadhesive solution will decrease the adhesion performance, while the passively elongated curing time may lead to incomplete curing of the bioadhesive materials, leading to deteriorated adhesive strength.

Given these conditions, one of the future efforts in minimally invasive bioadhesive printing could be to develop other types of sound printable of bioadhesive materials featuring rather fast curing rate, while meeting all the necessary requirements listed in Supplementary Note 2. Our sound printable bioadhesive material features 3 mins curing time at 42 °C under hotplate curing. In S_3P, we fully leverage the printing behavior of the on-tissue sound printing to significantly accelerate the curing rate of our bioadhesive material.

Just like the sonothermal effect, the acoustic streaming effect is also inevitable in sound printing techniques. In existing through tissue sound printing techniques, the acoustic streaming is an adverse effect to the sound printing process, since the very high sound pressure induced intense acoustic streaming will dilute the radical concentration and lead to the rapid heat dissipation in the focal zone (reactivity zone), thus deteriorating the material polymerization process. Therefore, the self-enhancing sono-ink design by *Kuang et al*, deployed a novel material design, which can spatially narrow the small oval-shaped focal zone by its nonlinear acoustic propagation effect at high acoustic pressure so that the printing material can be transiently polymerized only at the center of the heating zone where the temperature increased above the curing threshold.

In S^3P, the printing process will also experience acoustic streaming, though the input sound pressure is in a low level. The acoustic streaming is a nonlinear phenomenon which is highly sensitive to the boundary conditions[15]. The delivery process of bioadhesive to tissue surfaces naturally provides a boundary to the acoustic streaming, where the tissue surfaces can be utilized to reshape the acoustic streaming pattern. Under the boundary effect of the tissue surfaces, acoustic streaming will form a local circulation flow pattern near the tissue surface (Supplementary Note 4), once we deposit sound energy onto tissue surfaces. This local circulation will facilitate more efficient heat transfer from the tissue surface to the bioadhesive solution and the heat diffusion within the bioadhesive solution. Meanwhile, it will also enhance the mixing of PAA-NHS and HBCS, which, in turn, increases the frequency of reactive species collisions, thereby accelerating the amidation reaction rate during bioadhesive curing process. As a result, compared to hotplate curing at 42 °C, sonothermal heating significantly accelerates the curing time from 3 mins to 40 seconds, making S^3P applicable to emergency situations and harsh printing environments, e.g., cardiac hemostasis.

In light of the substantially impacts of the local circulation on the printing behaviors, we visualized and characterized this local circulation within bioadhesive solution induced by acoustic streaming under the tissue boundary effect through both simulation (Extended Data Fig. 18a) and particle imaging velocimetry (PIV, Methods, Extended Data Fig. 18b). As can be seen, the pattern size of the local circulation is larger than the focal zone (lateral size), and the measured velocity reaches the level of several millimeter per second. The heat diffusion facilitated by the local circulation is also experimentally validated by comparing the area size of tissue surface with elevated temperature. As illustrated by Extended Data Fig. 18e, under the same sound pressure exposure, the tissue with bioadhesive solution covered upon shows larger heated zone and more rapid heat diffusion compared to tissues naked to air (Note that, the air would effectively block the heat transfer from tissue to outside, leading to higher elevated temperature gradient and larger heat dissipation rate into the tissue. The experimental results actually enhanced our conclusion), proving the effectiveness of local circulation in facilitating heat diffusion both spatially and temporally.

We further validated the mixing effect to bioadhesive solution by this local circulation will also accelerate the curing rate from the molecular level. We put the bioadhesive solution on hotplate and mixed the solution by magnetic stirrer. Under 42 °C curing temperature for 40 seconds curing time, as the stirring speed getting higher, we see more amido bonds were formed (Extended Data Fig. 21b), fundamentally proving the mixing effect of local circulation would increase the curing rate of the amidation reaction rate.

Both the facilitated heat diffusion and the mixing effect by the local circulation promote the amidation reaction rate. By analyzing the cured bioadhesives by hotplate cuing (42 °C for 3 mins) and sonothermal curing (42 °C for 40 seconds) respectively, we see more amido bonds were formed (Extended Data Fig. 21a), further validating our theoretical analysis and the effectiveness of leveraging the local circulating to accelerate curing rate.

Supplementary Note 6. Printing resolution and printing accuracy.

The printing resolution and printing accuracy are two factors to evaluate a printing system. In S^3P, the printing resolution and the printing accuracy are collectively determined by the sound patterning resolution/accuracy, the on-tissue sound printing behaviors (i.e., the heat diffusion process), and the sound printable bioadhesive material (i.e., the temperature sensitivity).

1. Sound patterning resolution and accuracy. S^3P utilizes a transducer array and a deep learning-based algorithm to selectively deposit patterned ultrasound onto target tissue surface. The transducer array features a size of 50 mm × 50 mm (with a pitch size of 1 mm, Extended Data Fig. 1b), which, by the hologram theory[13], can effectively generate an on-axis sound image in size of 50 mm × 50 mm on the target tissue surface (meaning that the bioadhesive pattern should be less than 50 mm × 50 mm in geometry so that it can be delivered or printable in a single step). Due to the spatial bandwidth product (SBP)[16] limit, we digitalize the sound image by a digital resolution of 50 × 50 pixels, where each pixel covers a physical area of 1 mm × 1 mm, meaning that the sound patterning resolution (inverse to the pixel density) is 1 mm^2/pixel. We characterized our ultrasound transducer array by hydrophone scanning in its ability to generate a single focal point, where the effective focal size is ~950 μm in water medium (-6 dB attenuation criteria, Extended Data Fig. 2a, b, Methods), proving that our phased array system physically supports a sound patterning resolution of 1 mm^2/pixel.

We also characterized the focal size under different tissue thicknesses (of different tissue types) to evaluate the impact of energy dissipation due to tissue involvement (Fig. 2d, Extended Data Fig. 2e-g). For example, after penetrating through 50 mm thick liver tissue, a single focal point was successfully generated, and the focal size was measured to be ~1100 μm, while the focal pressure was attenuated by 34% compared to that in water medium. The focal pressure attenuation due to tissue penetration/absorption can be compensated by increasing the driving

voltage to the transducer array. In regard to the focal size, although it gets slightly higher compared to the value in water (Extended Data Fig. 2a, b), it still well matches our digital sound image resolution, validating that our sound printing system supports a sound patterning resolution of 1 mm^2/pixel in deep tissue.

Given the fixed sound image size (50 × 50 pixels covering a tissue area of 50 mm × 50 mm), and given an expected bioadhesive pattern (e.g., a circular pattern in size of 10 mm diameter), the bioadhesive pattern needs first to be digitalized into a sound image by 1 mm^2/pixel, which essentially generates a binary image (in which 1 represents where bioadhesive is needed and 0 represents no bioadhesive is needed. A 10 mm diameter circular bioadhesive pattern will take 78 pixels out of the 2500 pixels in the sound image). Then, based on the sound image, the deep learning algorithm can predict the phase information to actuate the transducer array. Afterwards, square-wave voltages in the same amplitude but modulated phases are generated to actuate the transducer array, which can emit sound waves, penetrate into the tissue, reach the target tissue surface, and finally interfere each other to form the expected sound image. Note that the thereby constructed sound image on tissue surface is in size of 50 × 50 pixels covering a tissue area of 50 mm × 50 mm. Ideally, in the constructed sound image, sound pressure will be uniformly high where bioadhesive is needed, and there will be no sound pressure in the left space of the sound image. By this way, we can make sure all sound energy will be deposited on the selected target tissue surface, which not only improves the sound energy delivery effieciency, but also make sure no other places on the tissue will be exposed to sound energy (thus improving the biosafety during the sound printing process compared to unpattern sound). Therefore, the sound patterning accuracy is validated by how the constructed sound image 'looks like' the expected sound image measured by the peak signal-to-noise ratio (PSNR). Our experiment results show that the constructed sound image features an average PSNR of 18.25, illustrating the capability of our sound printing system in generating high quality sound images (Extended Data Fig. 6c).

2. Enlarged reactivity zone. S^{3}P uses the sonothermal effect on tissue surface to selectively heat the bioadhesive solution to realize the minimally invasive delivery of bioadhesive onto target tissue surface. The heat generated on target tissue surface will thereafter diffuse from the heating zone to surrounding tissue and bioadhesive solution. If the tissue-bioadhesive system is motionless, we will see unevenly distributed temperature over the target tissue and the bioadhesive solution. This temperature inconsistency is even witnessed when the tissue surface is exposed to a single focal point (the tissue surface is not covered by bioadhesive solution), where the focal center shows the highest temperature than the surrounding tissue surface (Extended Data Fig. 18f). Under the context of single step sound printing, increasing the number of pixels in a given pattern would also lead to greater heat accumulation, particularly in the central zone of the pattern, resulting in inconsistency of the adhesion and mechanical strength of delivered bioadhesive over tissue (Supplementary Note 3).

Thanks to the acoustic streaming induced local circulation under the boundary effect of the tissue surface, the heat transfer from the heated tissue surface to the bioadhesive solution and the heat diffusion within the bioadhesive solution are effectively facilitated, resulting in more rapid and more evenly distributed temperature increase around the heating zone (Extended Data Fig. 8). For example (Extended Data Fig. 18e, f), using a single focal pressure to heat the stomach tissue surface (naked to air) until the temperature gets stabilized, we get a ~1.0 mm diameter circular region above 42 ℃, the center temperature is ~2.7 ℃ higher than the edge temperature of the heating zone. In contrast, under the same sound pressure, and covering the tissue surface with bioadhesive solution, we get a ~1.7 mm diameter circular region above 42 ℃, where the center temperature is only ~0.4 ℃ higher than the surrounding temperature. We further characterized the temperature inconsistency over the heating zone under different sound pattern sizes (Extended Data Fig. 9). The standard deviation of temperature over a 15 mm circular heating zone observed is ~0.48 ℃, while the temperature at the center is 0.9 ℃

higher. Due to this high temperature consistency facilitated by local circulation, the adhesion and mechanical strength of the delivered bioadhesives by S^3P are irrelevant to the sizes of the sound patterns, which is experimentally validated (Extended Data Fig. 20).

As discussed above, however, a direct consequence of the enhanced heat diffusion by the local circulation is that the effective heating zone gets wider than the sound focal zone (e.g., ~1.7 mm against 1 mm on stomach tissue), leading to the enlarged reactivity zone for bioadhesive curing, affecting both the printing resolution and printing accuracy. Note that, although the heat diffusion process is dominated by the local circulation, the heat conductivity of different tissues also slightly impacts the size of the effective heating zone (Extended Data Fig. 8), thereby leading to different printing resolutions (measured by the curing size under single focal pressure) on different tissue surfaces (Fig. 2e, Extended Data Fig. 22).

3. The temperature sensitivity of the sound printable bioadhesive material.

The printing resolution and printing accuracy are dependent on how the printing materials respond to external stimuli. For sound printing techniques based on sonothermal effect, the heat diffusion makes it difficult to confine the curing of the printing materials only within the focal zone. To improve the printing resolution of a sound printing technique, a good strategy is to confine the heat diffusion either spatially or temporally. For example, the sono-ink design by *Kuang et al.* spatially narrows the small oval-shaped focal zone by its nonlinear acoustic propagation effect at high acoustic pressure so that the printing material can be fast polymerized only at the center of the heating zone where the temperature increased above the curing threshold. Therefore, from the sound printing side, the sound printing materials are expected to possess a transient cuing mechanism (in the time scale of heat diffusion) at high temperature, meaning that high temperature sensitivity is preferred in order to realize high printing resolution.

In S^3P, the acoustic streaming induced local circulation facilitates the heat diffusion both spatially and temporally, leading to the rapid formation of enlarged effective heating zone beyond the focal zone (Extended Data Fig. 18e, f); meanwhile, the used bioadhesive solution features the curing time of 40 seconds under sonothermal heating at 42 ℃. These facts lead to the dependence of the printing resolution and printing accuracy on the spatial heat diffusion under sonothermal effect.

We characterized printing resolution (Fig. 2e, Extended Data Fig. 22) and printing accuracy (Fig. 2f, Extended Data Fig. 23) of S^3P on different tissues (e.g., liver, brain, stomach) at different temperatures (e.g., 37 ℃, 39 ℃, 42 ℃). The printing resolution is evaluated by measuring the lateral size of cured bioadhesives under single focal pressure, while the printing accuracy is evaluated from the size mismatch of the printed bioadhesives and sound patterns. Generally, S^3P realizes a printing resolution of ~1.7 mm − 2.2 mm (Fig. 2e), agreeing to the results in Extended Data Fig. 8d. In specific, a low printing temperature or a low thermal conductivity of the target tissue supports finer printing resolution (e.g., ~1.7 mm cured at 37 ℃ on stomach tissue); while, a higher printing temperature on tissues with higher thermal conductivity leads to coarser printing resolution (e.g., ~2.2 mm cured at 42 ℃ on liver tissue).

In regard to the printing accuracy, given a curing temperature and a tissue type, experiment results demonstrate the consistency of the printed circular bioadhesives in geometrical size. The delivered bioadhesives are on average ~1 mm larger than the sound pattern in diameter, regardless of pattern sizes, and the relatively larger bioadhesive size is explainable from the printing resolution of S^3P. For practical applications, the relatively larger pattern size of the delivered bioadhesive ensures the delivered bioadhesives meet clinical needs, such as soft tissue repair; meanwhile, leveraging this high printing consistency, we can realize accurate bioadhesive delivery if the high precision geometry is necessary for certain clinical applications.

Supplementary Note 7. Bioeffects of sonothermal heating to tissues.

Ultrasound exposure, while generally safe and widely used in medical diagnostics and therapies, can have adverse bioeffects if not carefully controlled. Excessive heating is a primary concern, as ultrasound waves absorbed by tissues can lead to temperature increases that surpass physiological thresholds, resulting in thermal damage. This risk is particularly significant in sensitive tissues, where thermal effects can cause protein denaturation, cellular damage, or even cell death. Additionally, the mechanical forces exerted by ultrasound waves can induce cavitation, wherein the formation and collapse of bubbles generate high pressures and temperatures, potentially causing tissue disruption and injury. Inertial cavitation, in particular, poses a significant risk due to the extreme conditions it generates. Prolonged or intense ultrasound exposure may also disrupt cellular functions and trigger apoptosis, further emphasizing the importance of careful monitoring and control of ultrasound parameters. While ultrasound offers numerous benefits in medical applications, including imaging and therapy, understanding and mitigating these adverse bioeffects are crucial for ensuring patient safety.

The Food and Drug Administration (FDA) of the United States plays a vital role in safeguarding the use of ultrasound technology in medical practice through its oversight of the Mechanical Index (MI) and Thermal Index (TI). While specific numerical thresholds for MI and TI are not universally mandated, the FDA provides comprehensive guidelines informed by scientific research and medical consensus. The MI serves to evaluate the potential for mechanical bioeffects, such as cavitation, which can occur during ultrasound exposure. On the other hand, the TI estimates the level of tissue heating that may result from ultrasound procedures. These indices are critical tools for healthcare professionals, enabling them to assess and manage the risks associated with ultrasound applications. Real-time monitoring of MI and TI values allows for prompt adjustments during procedures to ensure patient safety.

The FDA establishes maximum allowable values for MI and TI, considering factors such as ultrasound frequency, duration of exposure, and the intended clinical application to minimize the risk of adverse bioeffects. The FDA mandates that the mechanical index (MI) be kept below 1.9. In S^3P, the maximum sound pressure applied is 2.75 MPa, leading to the mechanical index maintained below 1.81. For $2.0 < TI \leqslant 2.5$, the safe exposure time should be less than 15 mins; for $2.5 < TI \leqslant 3.0$, the safe exposure time should be less than 4 mins; for $3.0 < TI \leqslant 4.0$, the safe exposure time should be less than 1 mins; for $4.0 < TI \leqslant 5.0$, the safe exposure time should be less than 15 seconds; for $5.0 < TI \leqslant 6.0$, the safe exposure time should be less than 5 seconds. In S^3P, the bioadhesive solution can be cured at 39 ℃ under sonothermal heating in about 2.5 mins, which meets the safety requirements to TI to be applied in the human body (for experiment with rats, the curing temperature was 42 ℃, resulting in curing time of 40 seconds under sonothermal heating, which also meets the safety requirement to TI).

S^3P uses patterned sound to realize the delivery of bioadhesive onto tissues in a single step. The sound patterning resolution (i.e., pixel density, or the number of pixels in a given pattern) substantially determines the heat accumulation on the target tissue surface. Theoretically, increasing the number of pixels in a given pattern leads to greater heat accumulation, particularly in the central zone of the pattern, which not only will result in unevenly distributed temperature on tissue surface, but also affects the printing resolution and adhesive performance. Since S^3P deposits sound onto target tissue surface, the thereby induced local circulation by acoustic streaming will facilitate heat diffusion over the heating zone, leading to more uniform temperature distribution and the avoidance of the local overheating within the patterned zone (thereby avoiding the biosafety concerns due to the heat accumulation). This phenomenon is also experimentally validated (Extended Data Fig. 18f), where the temperature inconsistency of the heating zone (maximum value - minimum value) covered by bioadhesive solution is much lower than that of the tissue naked to air (0.4 ℃ against 2.7 ℃).

To further demonstrate that the impacts of the sonothermal heating during S^3P on both normal and inflamed tissues are negligible, we performed S^3P treatment (42 ℃ for 40 seconds) on normal and inflamed tissues and assessed the effects of sonothermal heating in different tissue environments.

Sonothermal heating on normal tissues. Using the murine gastric and liver tissues as models, we observed that there were no significant differences in tissue integrity or cellular morphology between the S^3P-treated and untreated control groups (Extended Data Fig. 24e). Additionally, the degree of inflammation between the two groups was comparable (Extended Data Fig. 24f).

Sonothermal heating on inflamed tissues. Furthermore, we utilized imiquimod (IMQ)-induced psoriatic-like mice as an *in vivo* model of inflammation to investigate the effects of sonothermal heating with S^3P on pathological changes associated with skin inflammation (Extended Data Fig. 25). After four days of continuous IMQ treatment, the mice developed prominent psoriatic-like symptoms, with histopathological analysis showing significantly increased epidermal thickness compared to normal mice (Extended Data Fig. 25b). When IMQ treatment was discontinued, the untreated group, which did not undergo S^3P treatment, showed significant recovery of epidermal thickness by the third day, with the inflamed skin returning to near-normal levels. Interestingly, even when S^3P was applied to the inflamed skin after IMQ treatment was stopped, there was no adverse effect on the recovery of epidermal thickness. On day 3 post-treatment, the epidermal thickness in the S^3P-treated group was comparable to that of the untreated group, with both groups showing similar levels of recovery to normal tissue thickness (Extended Data Fig. 25c, d).

These experiments collectively demonstrate that the sonothermal heating effect generated by S^3P does not significantly impact the state of either normal or inflamed tissues, further supporting the safety and minimal impact of S^3P on tissue health.

Supplementary Note 8. *In vivo* applicability to wet and dynamic tissue surface under varying physiological conditions.

It is significant to ensure the applicability of S^3P in deep tissues under different physiological conditions, particularly given the wet and dynamic nature of deep tissues. Our strategy to ensure stable curing and adhesion formation in deep tissues is comprehensive, which is discussed as follows.

1. Leveraging the acoustic streaming effect to break the interfacial water barrier on wet tissue surfaces to realize efficient adhesion formation. Notably, in bioadhesive's chemistry, it is well acknowledged that bioadhesive delivery in deep tissue is inherently challenging due to the wet and dynamic nature of tissue surfaces, which stops the effective formation of adhesion to tissue surface. Conventionally solved from the bioadhesive material design side[17], our S^3P, decouples this challenge from the bioadhesive material design. Since S^3P selectively deposits sound energy onto target tissue surface to heat the bioadhesive solution by sonothermal effect, the instantaneously induced acoustic streaming will break the interfacial water on tissue surface, thereby facilitating stronger and efficient adhesion formation to tissue surfaces. This is evidenced by the experiment results in Fig. 3d, which compared the adhesion strength between hotplate curing and sonothermal curing (the adhesion strength was improved from ~33 J/m^2 to ~70 J/m^2 on rat colon).

2. Utilizing the local circulation to promote heat diffusion under low temperature gradient to accelerate the curing time. The printing behavior of sound printing is substantially determined by the heat diffusion process. Since S^3P selectively deposits sound energy onto target tissue surface, the heat transfers from the heated tissue surface into the bioadhesive solution. Due to the low-temperature curing and adhesion formation requirements imposed by biosafety concerns, the elevated temperature on tissue surface is only a few degrees

higher than that of the bioadhesive solution. The very low temperature gradient inherently determines the low heat diffusion rate from the heated tissue surface into the bioadhesive solution, thus leading to long curing time. Meanwhile, the wet and dynamic nature of tissue surfaces results in more challenges to control the heat diffusion process to keep stable curing temperature in long term (the curing time). For this problem, we deposit the sound energy onto target tissue surface instead of the bioadhesive solution, which would induce a local circulation inside the bioadhesive solution near the tissue surface upon ultrasound exposure due to the tissue surface boundary effect. This local circulation facilitates more efficient heat diffusion within the bioadhesive solution (Extended Data Fig. 18) and enhances the mixing of PAA-NHS and HBCS. This, in turn, increases the frequency of reactive species collisions, thereby accelerating the amidation reaction rate. As a result, compared to hotplate curing at 42 °C, sonothermal heating accelerates the curing time from 3 mins to 40 seconds, making S^3P applicable to the harsh environments of cardiac hemostasis (Fig. 3f, g).

3. Meticulous bioadhesive material design to achieve effective bioadhesive and adhesion delivery against body fluid dilution on wet tissue surfaces. By delving into the printing characteristics of the PAA-NHS/HBCS formulation, the concentration of the PAA-NHS/HBCS determines the adhesion strength, the mechanical properties, the curing temperature, and the curing time (Extended Data Fig. 11). Compared to polymerization-based through-tissue sound printing techniques relying on high sound pressure and high temperature (whose curing time is in seconds), our thermosensitive hydrogel bioadhesive cure and form adhesion to tissues near the body temperature for biosafety, where the tradeoff is the elongated curing time. This is inevitable due to the limited acoustic power input given a curing temperature marginally higher than that of the body, otherwise the bioadhesive material will not show printability. A direct consequence of long curing time is that it leads to challenges to the printing controllability due to the dilution of body fluid. The body fluid dilution may change the concentration of the PAA-

NHS/HBCS, and the PH level of the bioadhesive solution, which may lead to inadequate delivery of bioadhesive to fulfill its functionality, e.g., for tissue sealing, particularly given the bioadhesive is used for minimally invasive *in vivo* printing. As confirmed from Extended Data Fig. 11, as the concentration of the PAA-NHS decreases, the adhesion strength drastically decreases.

We set the curing temperature to be 37 °C (the body temperature) for our bioadhesive material after thorough and meticulous consideration. On one hand, 37 °C is the lowest feasible temperature to ensure printability, while the corresponding concentration of PAA-NHS and HBCS is the highest we can get. Once the concentration gets higher, the curing temperature will be lower than 37 °C, resulting in the losing of printability. On the other hand, the curing temperature of 37 °C allows us to get the highest adhesion/mechanical strength and the shortest curing time for the PAA-NHS/HBCS formulation without compromising printability, meanwhile makes the bioadhesive solution robust to body fluid dilution. This material design enables us to deliver effective bioadhesive and adhesion onto deep tissue surfaces against body fluid dilution (we have validated that our bioadhesive can be effectively cured under the PH level of 6 and 7.4 and upon inflamed tissue surfaces, see Extended Data Fig. 13c and Extended Data Fig. 25). Our experiments validate that, the recipe of our sound-printable bioadhesive materials meets all the necessary requirements and shows applicability in clinics, e.g., for soft tissue repair.

4. Leveraging focal depth to get adaptation to tissue vibration. The wet and dynamic nature of deep tissues makes it challenging to precisely deposit sound energy onto target tissue surface, thus may lead to temperature fluctuation during printing process. By studying the single focal profile of our system, we found that the focal depth in the propagation direction is 4 times larger than the focal size in the lateral direction (~4 mm against ~1 mm, -6 dB attenuation

criteria, Extended Data Fig. 2b, d). Therefore, by placing the target tissue surface to be roughly perpendicular to the wave propagation direction, we get adaption to tissue vibration by leveraging the large focal depth. Our experiments validated that this strategy makes S^3P applicable in rats for cardiac hemostasis, capable of effectively delivering bioadhesive and adhesion under the tissue vibration of rat heart.

5. Leveraging the dynamic wave modulation capability of our system to keep stable curing temperature on dynamic tissue surfaces inside human body.

Our phased transducer array and deep learning algorithm is capable to dynamically adjust the emitted sound parameters (our system at current stage can update the sound pattern and the pattern position in 10 Hz). Given the low vibration frequency of deep tissues (e.g., the natural frequency of the abdominal viscera is 4 ~ 6 Hz), we can use our system to precisely and dynamically modulate the sound patterns to precisely deposit sound energy onto target tissue surfaces to keep stable curing temperature. The successful implementation of this strategy depends on the real-time imaging of deep tissue surface to the printing system as feedback. We can use real-time ultrasound imaging or a minimally invasive laparoscope to realize this objective. This strategy is particularly useful if we apply S^3P to larger animals or even humans in clinics, since the vibration amplitude of large animals or humans can reach centimeter level, leading to the incompetence of the strategy of leveraging focal depth to overcome vibration mentioned in last paragraph.

Supplementary Discussion

The minimally invasive and controllable bioadhesive delivery problem. Bioadhesives and bioadhesion techniques are considerably applied in wearable electronics, biomedical implants, wound closure, regenerative medicine, and drug delivery. Despite the extensive range of available options designed specifically to address certain clinical and healthcare requirements, a pervasive challenge remains: the application of almost all existing bioadhesives onto tissues inside the body hinges exclusively on invasive surgical procedures. A direct and intuitive solution to this problem is to first inject liquid bioadhesive into the body, followed by the on-demand curing of the bioadhesive under external stimuli (like light or sound waves). Meanwhile, sound waves offer remarkable deep penetrability and biocompatibility. These facts inspire us to find a feasible solution to this problem through sound printing techniques.

Given one specific type of sound printing technique, it inherently supports the fabrication of certain material deep inside the body. Since the report of direct sound printing, the sound printing techniques have been advancing rapidly. However, existing/conventional sound printing techniques cannot be adequately utilized to fabricate bioadhesive deep inside the body. It is not only a material problem, but also there are other challenges to overcome for one sound printing technique to be applicable.

1. From through-tissue sound printing to on-tissue sound printing, the biosafety puts limit to the input acoustic power.

2. From sound printable material to sound printable bioadhesive material, the controllability necessitates the sound responsive adhesion formation in sound printable material design.

3. From fabricating 3D constructs to delivering bioadhesives to tissue surfaces, the effective formation of adhesion requires to overcome the interfacial water barrier on tissue surfaces.

Having tried our best efforts, we are unable find a feasible solution from the realms of sound printing, material science, and bioadhesive's chemistry, or a simple combination of existing techniques, to solve the above-mentioned challenges. These challenges not only highlight the uniqueness of the underlying research problem, but also underscore the significance of our sound printing technique.

The distinctions between our S^{3}P and existing sound printing techniques. The distinctions between the current research and existing sound printing techniques are discussed as follows:

1. Difference in concept. Our S^{3}P represents a controlled and biosafe sound printing method for the minimally invasive, *in vivo*, and *in situ* delivery of bioadhesives onto the deep tissue surfaces. In this regard, S^{3}P can be conceptualized as an 'on-tissue sound printing' technique, given that the printing unfolds directly on the tissue surfaces. By extension, we refer to existing sound printing techniques (e.g., *Nat Commun* **13**, 1800, 2022, *Science* **382**, 1148-1155, 2023) as 'through-tissue sound printing', where the sound waves propagate through the tissues and the printing occurs within the body, without the tissue being a concern in the material curing zone or a condition in the fulfillment of the printing functionality (e.g., the delivery of bioadhesives to tissue surfaces). Under these definitions, both our 'on-tissue sound printing' technique and existing 'through-tissue sound printing' techniques can be categorized as minimally invasive sound printing techniques, capable of printing deep inside body.

2. Difference in functionality. Our 'on-tissue sound printing' is developed for the minimally invasive, *in vivo*, and *in situ* delivery of bioadhesives (and bioadhesion) onto the deep tissue surfaces, while existing 'through-tissue sound printing' techniques (*Nat Commun* **15**, 6691, 2024, *Science* **382**, 1148-1155, 2023), like other 3D printing techniques using focused light, are developed for the fabrication of geometrically complex 3D constructs, with the deep-penetration printing capability into opaque media (such as tissues).

3. Difference in minimally invasive *in vivo* applicability. The direct impact of tissue involvement in the on-tissue printing process is the printing materials and sound waves must engage intimately with tissue. For instance, for the minimally invasive bioadhesive delivery on deep tissue surfaces investigated in this work, sound energy must be localized on the target tissue surface to induce a temperature rise on tissue surface, in order to facilitate both the curing of the bioadhesive and the formation of adhesion between the tissue surface and the cured bioadhesive. In contrast, 'through-tissue sound printing' techniques direct sound energy towards the printing materials to catalyze polymerization reactions. As such, the integration of the tissue surface in the printing process (material reactivity zone) introduces heightened challenges in the design of printing materials and the curing mechanism by imposing stricter biosafety constraints to meet the *in vivo* applicability requirements.

4. Difference in curing mechanisms and printing materials. To achieve our 'on-tissue sound printing', ensuring the biosafety of the printing process is crucial. In this context, a curing mechanism that operates at low temperatures (slightly above body temperature) is highly preferable. However, such a minimal temperature increase (<5 °C) is insufficient for polymerizing existing materials. This constraint renders polymerization-based sound printing techniques and polymerization-dependent ultrasound curable materials unsuitable for the minimally invasive delivery of bioadhesives to deep tissues. On the other hand, given that the curing mechanisms of ultrasound-driven polymerization, as utilized in existing sound printing techniques, rely on high sound pressures, elevated temperatures (>70° C), or radicals, these methods are ill-suited to meet the biosafety demands of 'on-tissue sound printing'. It follows that the successful implementation of our 'on-tissue sound printing' necessitates the using of new materials and different sound curing mechanism, thereby distinguishing our 'on-tissue sound printing' from existing 'through-tissue sound printing' as a novel category of sound printing technique.

The unique on-tissue sound printing behaviors. Apart from the aforementioned distinctions with existing sound printing techniques, S^3P also features its own printing behaviors. As pointed out by *Kuang et al.* in their sono-ink work, sound printing face the challenges of sound-induced streaming. However, acoustic streaming manifests different characteristics for on-tissue sound printing from existing through-tissue sound printing. Our research on S^3P provides basic understanding of the acoustic streaming and its effects to the on-tissue printing process.

- **Boundary effect leads to local circulation in bioadhesive solution.** Due to the boundary effect imposed by the tissue surface, the acoustic streaming will form a local circulation around the sound beam inside the bioadhesive solution near the tissue surface upon ultrasound exposure, which manifests a different streaming pattern as in through-tissue sound printing (Extended Data Fig. 18a, b).

- **Local circulation helps to break the interfacial water barrier on tissue surface, fostering stronger adhesion.** A common knowledge from the bioadhesive field tell that the interfacial water is barrier preventing the effective formation of adhesion to tissue surfaces. In bioadhesive's chemistry, one bioadhesive material should be designed to overcome the interfacial water barrier. In on-tissue sound printing, the sound induced local circulation helps to overcome the interfacial water, decouples this challenge from material design, meanwhile fosters a strong adhesion to the tissue compared to hotplate curing.

- **Local circulation helps the spatiotemporal heat diffusion, promotes uniform temperature distribution in patterning zone, accelerates the sound curing rate.** The local circulation facilitates more efficient heat diffusion within the bioadhesive solution and enhances the mixing of PAA-NHS and HBCS. This, in turn, increases the frequency of reactive species collisions, thereby accelerating the amidation reaction rate. As a result, compared to hotplate curing at 42 °C, sonothermal heating accelerates the curing time

from 3 mins to 40 seconds, making S^3P applicable to the harsh environments of cardiac hemostasis, where the wet and dynamic environments with blood bleeding have been rather challenging even for bioadhesive research field.

- **Local circulation expands bioadhesive curing zone.** The local circulation promotes spatiotemporal heat diffusion through heat convection. Due to this reason, compared with existing polymerization-based sound printing techniques where the focal zone determines the reactivity zone, in our on-tissue sound printing, the local circulation would expand the reactivity zone to be larger than the focal zone. For this reason, on-tissue sound printing technique faces different challenges to improve the printing resolution compared to through-tissue sound printing.

In summary, the capability of minimally invasive delivery of functional bioadhesives onto deep tissue surfaces inherently contribute to clinics, opening up new chances to wearable electronics, biomedical implants, wound closure, regenerative medicine, and drug delivery. As the first endeavor in this regard, S^3P notably fulfills its functionality and minimally invasive *in vivo* applicability. It is for sure that the utilized bioadhesive material is critical for the success of S^3P, and we fully recognize that bioadhesives with different properties are required for different clinical tasks. For clinical tasks requiring stronger adhesion and mechanical strength, or faster curing ratio and higher resolution, other types of sound-printable bioadhesive material should be developed, but they should first satisfy the necessary requirements in order to by deplorable by S^3P. Our fundamental understanding obtained from S^3P to the sound printing process and the sound-printable adhesive materials provide valuable insights for future efforts to develop other types of sound printing adhesive materials in bioadhesive's chemistry.

Supplementary Video S1. Overview of single-step sound printing of bioadhesive in deep tissue.

Supplementary Video S2. Sound pressure induced fluidic streaming facilitates the permeation of bioadhesive into interfacial water on tissue surface. In this video, we visualized the sound pressure induced streaming through simulation and experimental setups.

Supplementary Video S3. Selective sonothermal heating to porcine skin.

Supplementary Video S4. The acoustic streaming induced local circulation facilitates the spatiotemporal heat diffusion.

Supplementary Video S5. Minimally invasive printing of triangular bioadhesive on mouse kidney.

Supplementary Video S6. Cardiac hemostasis with single-step sound printing on rat *in vivo*. This video is to demonstrate the capability of S^3P to effectively deliver bioadhesive in the wet and dynamic tissue surfaces inside the body.

Supplementary Video S7. Minimally invasive gastric perforation repair with single-step sound printing on mouse.